Lasing and Modified Spontaneous Emission in Photonic Crystal Structures and Microcavities

Thesis by

Reginald K. Lee

In Partial Fulfillment of the Requirements
for the Degree of
Doctor of Philosophy

California Institute of Technology
Pasadena, California

2000
(Defended May 22, 2000)

Acknowledgements

I would like to thank some of the people who have supported me during the past years. First and foremost, I am greatly indebted to my advisor, Professor Amnon Yariv, for providing me with the opportunity and privilege of being a member of his research group. I also owe a great deal of thanks to Professor Axel Scherer, who was like a second advisor to me. His constant encouragement and advice have been greatly appreciated. Having the opportunity to work so closely with both of these professors has been a unique and rewarding experience.

I have enjoyed and benefited from working closely with various members of both research groups. In particular, I would to thank our former group member Dr. John O'Brien, who provided guidance and taught me a great deal. I also enjoyed working with Drs. Gilad Almogy and Yujian Xu. My research on photonic crystals has not been in isolation. I would like to thank Dr. Chuan-Cheng Cheng, Yong Xu, Oskar Painter, Dr. Thomas Krauss, and Dr. Ali Adibi, with whom I have had the opportunity to work. I have also enjoyed many fruitful discussions with Dr. Bruno Crosignani and would like to thank him for encouragement and advice. I would also like to thank Dr. Jack Jewell from Picolight Incorporated, who taught me the basics for doing optical measurements on semiconductor devices.

Thanks to the students with whom I shared an office Dr. Matt McAdams and more recently: John Choi and William Green. Also thanks to Dr. Bill Marshall for the many interesting discussions and talks in our office over the years that I have spent in that room. The many long days (and nights) in the lab would not have been the same without the friendships of Dan Provenzano and Roger Koumans. I would also like to thank former group members Atsushi Sugitatsu, Benjamin Kitzke, and Drs. Doruk Engin, Boaz Salik, Xiao Lin Tong, Randy Salvatore, and Danny Eliyahu.

My everlasting gratitude to Ali Ghaffari and Dr. Ali Shakouri for teaching me MBE crystal growth, semiconductor fabrication, and for generally instilling in me the

discipline, caution, and care needed to work with semiconductor fabrication. I would also like to thank former and current staff members in our group: Jana Mercado, Connie Rodriguez and Kevin Cooper.

I would also like to thank various members of Dr. Scherer's group: Dr. Theodore Doll, for his energy and encouragement; Reynold Johnson, for his constant jokes and his help; and David Barsic, who has had the unenviable job of trying to fix the things other people broke. In my close collaboration with Prof. Axel Scherer, I must thank his assistants over the years: Michelle Vine, Marlene Moncado, and Kate Finigan.

My thanks to Drs. Tino Alavie, Myo Ohn, and Robert Maaskant from E-Tek Corporation, which was formerly Electrophotonics Corporation, with whom I collaborated at the University of Toronto Institute for Aerospace Studies. I enjoyed working with them and their friendships and advice originally encouraged me to come to Caltech.

I would also like to thank Tony Vanelli for all his advice and friendship. He always brought a refreshingly Texan perspective to our discussions, which were always interesting, refreshing, and stimulating.

I would like to thank Drs. Se Oh, Jeff Ungar, and T.R. Chen from Ortel Corporation for their advice and for some of the epitaxial crystal growth used for this thesis. Also thanks for our brief collaboration to Professor Eli Yablonovitch and his former student Dr. Misha Boroditsky from the department of electrical engineering at UCLA.

Finally I'd like to express my deepest gratitude to Joyce Wong for her friendship, support, encouragement, and help here and there in the lab. And to my parents and my brother for their love and support.

Abstract

Semiconductor light-emitting devices in the near-infrared (1.55 μm) based on microfabricated photonic crystal structures are demonstrated. The photonic structures consist of two-dimensional arrays of air holes patterned into an optically thin, air-suspended InGaAsP slab by high-resolution electron beam lithography and various dry etching techniques.

Two types of microcavities are examined. The first are larger hexagonally shaped cavities in the range of 10 to 20 μm in size and bounded by the photonic crystal structure. Cavity mode spontaneous emission at room temperature under optical pumping is used to demonstrate mode confinement due to the in-plane bandgap. No cavity mode peaks in the emission spectrum are seen if the in-plane bandgap is not spectrally aligned with the material emission. Pulsed lasing is also demonstrated with the lasing threshold at 66 mW peak incident optical pump power at a duty cycle of less than 1% in order to minimize membrane heating. Changes in the pump geometry is shown to result in controllable lasing mode switching. This behaviour is explained in terms of mode Q, lasing threshold and enhanced spontaneous emission into the mode.

The second type of microcavity consists of a single point defect into photonic lattice with a modal volume of 2.5 $(\lambda/2n)^3 \approx 0.03\mu\text{m}^3$. Cavity quality factors up to 250 are demonstrated and suppressed spontaneous emission due to the bandgap except at the mode frequency is shown. Pulsed lasing at 143 K under optical pumping is demonstrated.

The fundamental modification of the spontaneous emission rate due to the in-plane bandgap in a photonic crystal slab structure with no microcavity is experimentally and numerically examined. Incomplete bandgaps are theoretically shown to be able to strongly inhibit spontaneous emission. High density of states points in the bandstructure are seen to greatly enhance the spontaneous emission rate. Measurements using phase sensitive spectroscopy of the spontaneous emission rate from quantum wells in the photonic crystal slab show a greater than 10 times inhibition of the emission rate in the in-plane bandgap. Experimental evidence for saturation of the surface recombination at relatively low pumping levels is found.

Contents

List of Figures

List of Tables

Chapter 1 Introduction

1.1 Background and a brief history of photonic crystals

Periodic structures in photonics have long been used to modify the behaviour of photons, if the periodicity is comparable to the wavelength. In particular, one-dimensional periodic structures have found broad applications [1]. These one-dimensional periodic structures have, until recent years, not been typically discussed in terms of bandstructure and photon bandgaps and include such commonly used structures as Bragg mirrors, gratings, the distributed feedback (DFB) laser [2, 3], the vertical cavity surface emitting laser (VCSEL) [4], and the less common anti-resonant reflecting optical waveguide (ARROW) [5] and the Bragg waveguide [6]. A simple extension of these one-dimensionally periodic devices are structures with periodicity in multiple directions. This was suggested in 1987 independently by E. Yablonovitch [7] and S. John [8]. In these works, three-dimensionally periodic dielectric structures were suggested that would exhibit a complete three-dimensional bandgap for photons. The similarity between the vector wave equation and electromagnetic waves with semiconductor crystals and Schrödinger waves naturally led towards drawing analogies between electromagnetism and solid state physics. However, whereas the crystal structures and atomic potentials in solid state physics are determined by nature, photonic crystals are man-made and provide a means on a microscopic scale, to engineer the material response to electromagnetic radiation.

Integration of photonic bandgap structures into light emitting semiconductor material has been predicted to provide a means to control radiation processes in the semiconductors [9] and to form high-Q microcavities as defects of the periodic structure [10]. A schematic of this type of process is shown in Fig. 1.1. Radiative transi-

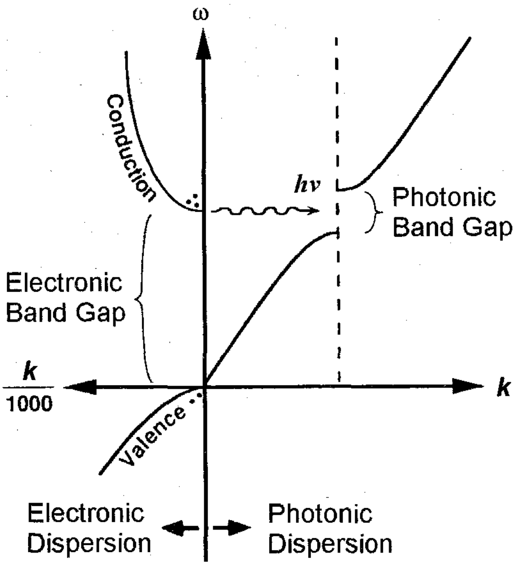

Figure 1.1: Dispersion relation of electrons in a semiconductor crystal and photons in a photonic bandgap crystal after Yablonovitch [9].

tions can occur between electrons and holes in the electronic band structure (shown on the left of Fig. 1.1), emitting a photon whose energy depends on the electronic energy bandgap. If the photon energy lies in the photonic bandgap frequency range, the electron-hole recombination process can be inhibited since there are no electromagnetic modes into which the an emitted photon could radiate. This means that the photonic bandgap crystal can be used either to inhibit internal radiation or to reflect radiation (essentially, inhibiting external radiation). This has primarily been the point of view pursued to date in the photonic bandgap crystal field (for a review, see [11] and [12]). However, interesting behaviour can occur even when the recombination energy is not aligned with the photonic bandgap, since the periodic structure modifies the dispersion relation at all frequencies including those away from the bandgap. Indeed, even structures with no photonic bandgap can exhibit diffractive effects due to the periodicity. Drawing on the analogy between solid state physics and photonic crystals, it seems clear that focusing on the bandgap overlooks the full richness of solid state physics in which the complexity of behaviour frequently lies not in the electronic bandgap itself, but rather in the band and sub-band structure.

1.1.1 From 1D to 3D and back

The development of the photonic bandgap (PBG) crystal field historically has progressed from one-dimensional structures used in a wide variety of photonic devices for many years, to the more recent extension of these ideas to 2- and 3-dimensional periodicities in pursuit of complete three-dimensional bandgaps. The underlying principle is that schematically shown in Fig. 1.1, that complete control of the radiation requires a complete bandgap. However, there has been a recent shift in interest back towards lower-dimensional periodicities in which ideas that manifested due to the treatment of photonics and optics in the language of solid state physics have been reduced to lower-dimensional cases exhibiting novel behaviour. Due to its complex geometry, there has been limited experimental success with three-dimensional photonic crystals. Two-dimensionally periodic structures, however, have flourished due in part to the easier fabrication for two-dimensional geometries and also to the easier manipulation of the photonic lattice to increase functionality (such as point and line defects as microcavities and waveguides, respectively). In fact, this trend has extended all the way "back" to one-dimensionally periodic structures, which have been found to be able to exhibit full photonic bandgaps and to completely control spontaneous emission [13].

1.1.2 The photonic crystal lattice

The analogy of electromagnetism with solid state physics is a transcendent theme in all discussions of PBG crystals. The periodicity in the dielectric constant in Maxwell's equations plays the same role as the periodic electron potential does in Schrödinger's equation. Following the trend towards lower-dimensional periodic structures, the work in this thesis has been primarily focused on two-dimensional photonic crystals. An example, of particular interest to this work is the triangular array of photonic "atoms" shown in Fig. 1.2 at circles of high dielectric material. In this case high dielectric constant "atoms" play the role of atomic electron potential wells. Since many of the bandstructure properties can be derived purely from symmetry considerations, we can also have inverse atoms where the circles in Fig. 1.2 may represent low dielectric constant regions in a high dielectric background. Whereas solid state physics is limited by gifts from nature determining the electron potential wells and the symmetries of the crystal, since PBG crystals are man-made, the possible structures and photonic "atoms" are limited by imagination as well as skill and technology to realize the structures. In following with the solid state physics analogy, the reciprocal lattice for this periodic structure is shown in Fig. 1.3.

1.2 Modified spontaneous emission

It has long been known that the spontaneous emission rate for an electronic transition can be enhanced [14] or inhibited [15] by the local electromagnetic environment. Controlled spontaneous emission in semiconductor and other solid state systems has been of great interest in recent years both for light emitting device applications as well as fundamental quantum electrodynamic studies. The vertical cavity surface emitting laser (VCSEL) structure has been the semiconductor microcavity of choice since modern epitaxial techniques provide means to make extremely high quality microcavities. Recent years have also seen the advent of the microdisk laser [16, 17, 18, 19]. This type of microcavity also shows promise for modified spontaneous emission due to the relatively small modal volumes possible, high mode quality factors, and strong mode coupling (β-factor) [20, 21]. To date, the highest magnitude Purcell effect enhancement on a solid state emitter has been demonstrated in 1999 by Gerard et al. [22, 23, 24]. In this work, Purcell enhancement factors of ×5 for narrow pillar VCSEL-like structures and ×15 for microdisks were demonstrated from quantum dots at low temperature 8K. Weaker enhancement of ×2.3 (although not yet optimized) has been shown in oxide apertured VCSEL structures also with quantum dot emitters at 10K [25, 26].

From their conception, photonics crystals have been suggested as a means towards modified spontaneous emission [7]. In theory, a three-dimensional photonic bandgap should be able to completely inhibit spontaneous emission. Also, the small modal

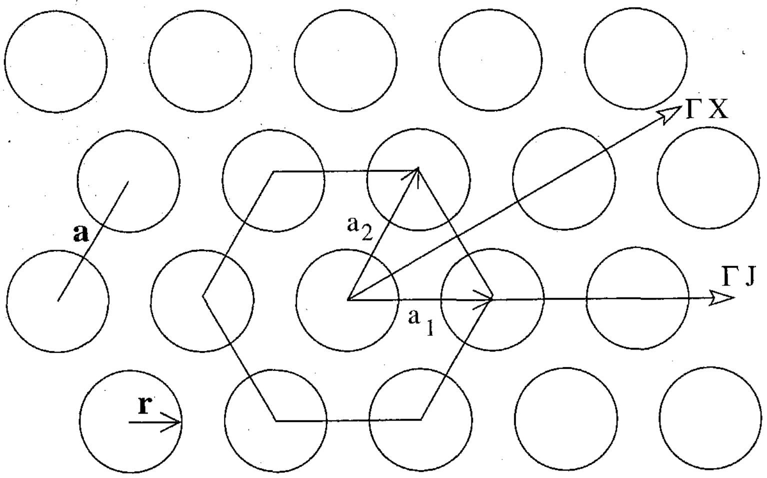

Figure 1.2: Schematic diagram of two-dimensional triangular photonic bandgap lattice. a_1 and a_2 are the primitive lattice vectors and ΓJ and ΓX indicate high symmetry directions of interest in the lattice.

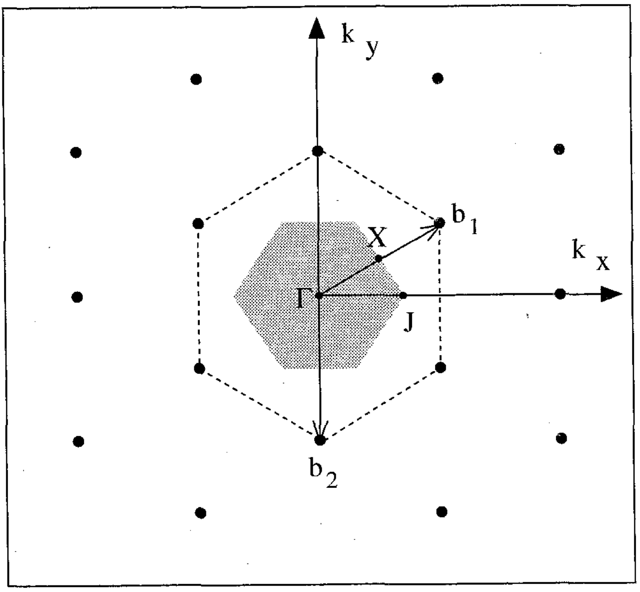

Figure 1.3: Schematic diagram of two-dimensional triangular photonic bandgap lattice Brillouin zone in reciprocal space. The shaded region indicates the first Brillouin zone with primitive lattice vectors b_1 and b_2. Γ, X, and J are high symmetry points in the reciprocal lattice

volumes possible by photonic crystal defect microcavities [27, 28, 29] make these types of structures promising for the enhancement of spontaneous emission. Inhibited spontaneous emission in photonic crystals has been previously demonstrated in the microwave regime of the electromagnetic spectrum. Yablonovitch and Gmitter [30] demonstrated photon bands in the microwave region of the spectrum in a period structure composed of low-loss dielectric material. A photonic band gap is achieved when the dielectric contrast between the scattering centers and the surrounding medium exceeds a critical value of $\epsilon_r > 10$ although the exact critical value depends on the precise geometry and symmetry used. Although the dielectric constant is weaker than this criteria ($\epsilon_r = 1.45$), Martorell and Lawandy [31] observed inhibited spontaneous emission in an ordered aqueous suspension of polystyrene spheres that self-assembled into a periodic array. More recently, Petrov et al. [32, 33] as well as Gaponenko et al. [34] have observed slightly inhibited spontaneous spectra and decay kinetics of dye molecules in an artificial opal photonic crystal. However, the small dielectric contrast in these structures limited the effect, since the structure did not support a complete bandgap. Romanov et al. have attempted to increase the dielectric contrast by depositing a high index material (MOCVD grown GaP) into the artificial opal structure [35, 36] however, the bandgap in this work was still incomplete. It has also been shown that a complete bandgap cover 4π steradians can be created using only a one-dimensional periodic structure [13]. Spontaneous emission inhibition and high spontaneous emission coupling ($\beta = 0.96$) have been predicted for this relatively simple structure.

1.3 Motivation

The beauty in the use of photonic crystals in optics and for photonic devices is in some sense also the most fulsome part. The complex geometries drawn from solid state physics provide a multitude of ways for the so-called band engineer to design a structure to satisfy a particular need or application. However, this brings with it the difficult problem of dealing with the same complex geometries in order to predict and optimize the behaviour. Two-dimensionally periodic structures lie in a potentially useful medial point between the simplicity of well known 1D periodic structures and devices and the complexity and richness of 3D crystals.

Experimental measurements on optical frequency photonic crystals are of interest in and of themselves because of the lack of experimental confirmation, until recent years, of the many numerical and theoretical predictions for photonic bandgap crystal structures. Two-dimensional PBG structures can be used in the typical "bandgap" view to form microcavity devices which confine photons due to the inability of the photons to propagate outside because of the bandgap. These types of micro- or nano-cavity laser devices are interesting because extremely small modal volume cavities are possible and the cavity confinement is geometrically determined instead of being material dependent (e.g., Fresnel reflection from the dielectric interface). However, light emitting diodes (LEDs) may be the application with the greatest impact in the near term. In fact, in 1998, the U.S. Academy of Sciences [37] cited LEDs as having a major impact on the economy for the next century.

The interest in light emitting diodes stems from the inherent inefficiency of these devices. Although modern crystal growth techniques have resulted in materials with internal quantum efficiencies of 90% or greater, typically only 3-20% of the light actually escapes with the remainder being reabsorbed and lost as heat. In addition to improvements to the external efficiency, photonic crystals, either through Purcell enhancement in microcavities, (the "bandgap" view) or directly through modified emission in the photonic crystal states themselves, may exhibit accelerated spontaneous emission rates. A fundamental limit to the modulation speed of a light emitting diode is the spontaneous emission rate, which means that this provides a means towards high efficiency, high modulation speed light emitting diodes. High efficiency LEDs have many potential lighting and illumination applications, which makes their development an economically important goal. High modulation speed LEDs may provide a cheap incoherent light source useful for telecommunication applications.

1.4 Summary of this thesis

This thesis discusses the theory and application of photonic crystal structures to active light emitting devices. This includes their uses in the design of small modal volume microcavity devices as well as the fundamental emission properties of the crystal themselves. Chapter 2 briefly outlines some of the theory and numerical techniques used to characterize the photonic crystal structures and microcavities. The two-dimensional plane wave expansion technique and the finite-difference time-domain (FDTD) algorithm are described. The use of the FDTD technique for classical electromagnetism to calculate the spontaneous emission rate, a fundamentally quantum mechanical process, will be briefly mentioned. This is not meant as a comprehensive examination but rather a brief overview of some points that may be a useful prelude to the remaining chapters.

Chapter 3 examines the quantum mechanical modification of spontaneous emission in greater detail. The general case of modified spontaneous emission in a microcavity including transition broadening and cavity mode linewidth is derived. The complex interplay between enhanced spontaneous emission into a mode, the lasing threshold, and stimulated emission are briefly discussed, showing possibly novel behaviour that may be possible with photonic crystal based microcavities. The modified spontaneous emission results for a microcavity mode will be compared with the traditional Purcell enhancement factor [14] and generalized to the case of bands of states.

Chapter 4 presents some of the first results from photonic crystal based microcavities in the near-infrared. The spontaneous emission behaviour showing bandgap confinement will be shown and lasing in the *hexagonal disk laser* is demonstrated. Mode switching and the relation between lasing modes and spontaneous emission are discussed in relation to the results of chapter 3.

Chapter 5 includes the results from the first demonstration of an isolated photonic crystal defect mode in the near-infrared. These cavities are similar to those described in chapter 4 but support only one or two modes which simplifies the interpretation of the results. Spontaneous emission measurements for these tiny "nanocavities" are presented showing lithographic tuning of the mode frequency. Low temperature pulsed lasing results are presented with lasing in a truly single mode cavity with modal volume of $2.5 \times (\lambda/2n)^3 \approx 0.03\mu\text{m}^3$.

Chapter 6 presents some numerical calculations on the spontaneous emission rate from a two-dimensionally patterns photonic crystal slab structure. Using the concept of localized density of states (LDOS), complete control of the transition dynamics is possible even in structures with incomplete bandgaps. The numerical results predict that both strong inhibition or enhancement of the spontaneous emission rate are possible.

Chapter 7 includes some of the first experimental evidence of strong inhibition of the spontaneous emission rate over the entire material transition bandwidth. Spontaneous emission in the bandgap are inhibited by nearly an order of magnitude $(6-10\times)$ as compared to the out-of-gap emission. Measurements from these structures also show the evidence of the enhanced extraction efficiency for emission into the photonic conduction band modes as predicted in chapter 6.

Chapter 2 Simulations of photonic crystals

2.1 Theoretical approach to photonic crystals

Photonic crystals in general have relatively complex geometry. Particularly for higher dimensionality, this results in some difficulty for theoretical treatments. For infinitely periodic structures, it is natural to look to frequency domain techniques to determine dispersion properties such as plane wave expansion. If the periodicity of the structure is essentially one [1] or two dimensional [38, 39] this problem is solved relatively easily. For the three-dimensional case, the problem becomes quickly becomes intractable due to the cubic relation of the required computation to the problem size. In addition, if the medium is not perfectly or infinitely periodic, such frequency domain techniques have difficulty converging because of high frequency terms introduced by the discontinuities. However, for one- or two-dimensional problems (or problems that can be effectively reduced to one or two dimensions), the speed and simplicity of the plane wave expansion method to determine frequency domain information such as the dispersion relation can be very useful if used judiciously.

2.1.1 Plane wave expansion

Following the method of Plihal and Maradudin [40], we begin from Maxwell's equations [41] in the simplest case where the medium of interest is linear and source-free.

$$\begin{aligned} \nabla \times \vec{H} &= \frac{\partial \vec{D}}{\partial t} \\ \nabla \cdot \vec{B} &= 0 \\ \nabla \times \vec{E} &= -\frac{\partial \vec{B}}{\partial t} \\ \nabla \cdot \vec{D} &= 0 \end{aligned} \tag{2.1}$$

with the constitutive relations

$$\vec{B} = \mu \vec{H} \qquad\qquad \vec{D} = \epsilon \vec{E} \tag{2.2}$$

Assume that the magnetic permeability, μ not a function of position. The six equations in Eq. (2.1) and Eq. (2.2) can be summarized in a set of two equations known as the vector wave equations for the magnetic and electric field.

$$\nabla \times \left(\frac{1}{\epsilon(\vec{r})} \nabla \times \vec{H} \right) = -\mu \frac{\partial^2}{\partial t^2} \vec{H} \tag{2.3}$$

$$\nabla \times \nabla \times \vec{E} = -\mu \epsilon(\vec{r}) \frac{\partial^2}{\partial t^2} \vec{E} \tag{2.4}$$

For the case of a photonic crystal, the spatial dependence of the dielectric constant, $\epsilon(\vec{r})$ as well as the magnetic and electric fields are periodic. We can therefore apply Bloch's theorem [42, 43] so that these functions can be written as

$$\epsilon(\vec{r}) = \sum_{\vec{G}} \epsilon_G \exp(i\vec{G} \cdot \vec{r}) \tag{2.5}$$

$$\vec{H}(\vec{r}, t) = \sum_{\vec{G}, \omega} \exp(i\omega t) \vec{H}_{G,\omega} \exp\left(i \left(\vec{k}(\omega) + \vec{G} \right) \cdot \vec{r} \right) \tag{2.6}$$

$$\vec{E}(\vec{r}, t) = \sum_{\vec{G}, \omega} \exp(i\omega t) \vec{E}_{G,\omega} \exp\left(i \left(\vec{k}(\omega) + \vec{G} \right) \cdot \vec{r} \right) \tag{2.7}$$

where the electric and magnetic fields have also been expanded as sums of plane waves. Substituting Eq. (2.5), Eq. (2.6) and Eq. (2.7) into the vector wave equations Eq. (2.3) and Eq. (2.4) we then have

$$\begin{aligned}
\left(\vec{k}+\vec{G}\right) \times \left[\sum_{\vec{G}'} \eta_{G'G} \left(\vec{k}+\vec{G}\right) \times \vec{H}_{G'}\right] + \omega^2 \vec{H}_G &= 0 && (2.8) \\
\left(\vec{k}+\vec{G}\right) \times \left[\left(\vec{k}+\vec{G}\right) \times \vec{E}_{G'}\right] + \omega^2 \sum_{\vec{G}'} \epsilon_{GG'} \vec{E}_{G'} &= 0 && (2.9)
\end{aligned}$$

For notational simplicity, we have defined the following parameters

$$\begin{aligned}
\frac{1}{\epsilon(\vec{r})} &= \sum_{\vec{G}} \eta_G \exp(i\vec{G}\cdot\vec{r}) && (2.10) \\
\epsilon_{GG'} &\equiv \epsilon_G - \epsilon_{G'} && (2.11) \\
\eta_{GG'} &\equiv \eta_G - \eta_{G'} && (2.12)
\end{aligned}$$

and ϵ_G is defined by Eq. (2.5). These equations form an eigenvalue problem that can be solved for the dispersion relation for any periodic structure. It should be noted that both vector wave equations Eq. (2.3) and Eq. (2.4) can be solved independently for the dispersion information since, in this form, the electric and magnetic fields have been separated. The magnetic field wave equation tends to be easier to solve because the operator in Eq. (2.3) is Hermitian [44, 45].

2.1.2 Bandstructures in 2 dimensions

We now consider the specific case of a purely two-dimensional structure. We must consider two polarizations that are possible. The transverse magnetic (TM) polarization has solutions to Maxwell's equations with the form

$$\begin{aligned}
\vec{H}(\vec{r},t) &= (0, 0, H_3(x_1, x_2, \omega)) \exp(i\omega t) && (2.13) \\
\vec{E}(\vec{r},t) &= (E_1(x_1, x_2, \omega), E_2(x_1, x_2, \omega), 0) \exp(i\omega t) && (2.14)
\end{aligned}$$

In this case, it is easiest to work with the vector wave equation Eq. (2.8) for the magnetic field, which reduces to

$$\sum_{\vec{G}_{\|}{}'} \left(\vec{k}_{\|} + \vec{G}_{\|}\right) \cdot \left(\vec{k}_{\|} + \vec{G}'_{\|}\right) \eta_{G'G} H_{G'_{\|}} + \omega^2 H_{G_{\|}} = 0 \tag{2.15}$$

In the case of the transverse electric (TE) polarization, the solutions will have the form

$$\vec{E}(\vec{r},t) = (0, 0, E_3(x_1, x_2, \omega)) \exp(i\omega t) \tag{2.16}$$

$$\vec{H}(\vec{r},t) = (H_1(x_1, x_2, \omega), H_2(x_1, x_2, \omega), 0) \exp(i\omega t) \tag{2.17}$$

and the wave equation Eq. (2.9) can be written as

$$\sum_{\vec{G}_{\|}{}'} \left(\vec{k}_{\|} + \vec{G}'_{\|}\right)^2 \eta_{G'G} E_{G'_{\|}} + \omega^2 E_{G_{\|}} = 0 \tag{2.18}$$

Dielectric function

The Fourier decomposition of the dielectric function represented by the parameters η_G is central to the solution of the eigenvalue problem. In the case of a structure composed of only two distinct dielectric regions, a, b, the parameters η_G can be determined by the following method. First, the inverse of the dielectric function in Eq. (2.10) is written as

$$\frac{1}{\epsilon(\vec{r}_{\|})} = \frac{1}{\epsilon_a} + \left[\frac{1}{\epsilon_a} - \frac{1}{\epsilon_b}\right] \sum_n S\left(\vec{r}_{\|} - \vec{r}_{\|}(n)\right) \tag{2.19}$$

where

$$S\left(\vec{r}_{\|}\right) = \begin{cases} 1 & \text{for } \vec{r}_{\|} \in R \\ 0 & \text{for } \vec{r}_{\|} \notin R \end{cases} \tag{2.20}$$

and R represents the region with dielectric constant ϵ_a. The Fourier components η_G are then given by the integral

$$\eta_{G_\parallel} = \frac{1}{\epsilon_b}\delta_{\vec{G}_\parallel,0} + \left[\frac{1}{\epsilon_a} - \frac{1}{\epsilon_b}\right]\frac{1}{a_{cell}}\int d\vec{r}_\parallel \exp(i\vec{G}_\parallel \cdot \vec{r}_\parallel)S(\vec{r}_\parallel) \qquad (2.21)$$

where the integration is over the entire $\vec{r}_\parallel$ plane. Given that the function $S(\vec{r}_\parallel)$ can only have the values 0 and 1, this simplifies to

$$\eta_{G_\parallel} = \begin{cases} \frac{f}{\epsilon_a} + \frac{1-f}{\epsilon_b} & , \quad \vec{G}_\parallel = 0 \\ \left[\frac{1}{\epsilon_a} - \frac{1}{\epsilon_b}\right]\frac{1}{a_{cell}}\int_R d\vec{r}_\parallel \exp(i\vec{G}_\parallel \cdot \vec{r}_\parallel)S(\vec{r}_\parallel) & , \quad \vec{G}_\parallel \neq 0 \end{cases} \qquad (2.22)$$

We have introduced the filling fraction for the structure f, which is defined as the fraction of the total area a occupied by dielectric material.

The triangular lattice of holes

This geometry is of particular interest since all subsequent sections and chapters will deal primarily with this lattice symmetry. This structure consists of a triangular lattice of air holes ($n_a = 1.0$) in a dielectric material (n_b) schematically shown in Fig. 1.2.

Taking the geometric function defined by the lattice of interest in Fig. 1.2, the integration in Eq. (2.22) can be solved to give

$$\eta_{G_\parallel} = \begin{cases} \frac{f}{\epsilon_a} + \frac{1-f}{\epsilon_b} & , \quad \vec{G}_\parallel = 0 \\ \left[\frac{1}{\epsilon_a} - \frac{1}{\epsilon_b}\right] f \frac{2J_1(G_\parallel R))}{G_\parallel R} & , \quad \vec{G}_\parallel \neq 0 \end{cases} \qquad (2.23)$$

where J_1 is the first order Bessel function.

2.1.3 Effective index approximation for PBG slabs

In microfabricated optical structures, the purely two-dimensional approximation is not accurate because of the difficulty in fabricating structures such as the two-dimensional triangular lattice of holes where the third dimension is large compared to the wavelength. In this case significant effects are expected due to the finite extent of the structure in the third dimension.

In this case where the structure is essentially two-dimensional but not infinite in the third dimension, some approximations can be made to reduce the problem to an effectively two-dimensional one that is then tractable using the plane wave expansion technique. One possible method is to solve the one-dimensional infinite dielectric slab problem to find the modal index for the slab modes [27]. In most cases we are particularly interested in the single mode case, so the modal index for the fundamental slab mode is used. This can then be used in the two-dimensional approximation in place of the actual material index (air is still modeled at $n_{air} = 1$). Other approximate techniques are possible to reduce the three-dimensional finite structure problem to a two-dimensional one (see for example [46, 47, 48]).

2.2 The finite difference time-domain technique

The finite difference time domain (FDTD) algorithm was first applied to numerically solve Maxwell's equations in 1966 by Yee [49]. The finite difference time domain technique (FDTD) has evolved into a very convenient method for solving electromagnetic field problems. Although not considered to be a computationally efficient numerical technique, the rapidly increasing speed of current computing technology has made this method of solution tractable in some cases. The advantage of this relatively simple technique derives from its ability to easily deal with any problem describable by the vectorial Maxwell equations limited only by computational resources. Fundamentally, as implied by the name, FDTD is a time domain technique; however, frequency domain problems can also be solved by using Fourier transformation methods while incurring only a small manageable computational penalty [50].

In the finite difference time domain method, a space-time mesh is applied to the problem and Maxwell's equations are replaced by a system of difference equations discretized on the mesh. Following Yee [49], a space grid is introduced to discretize

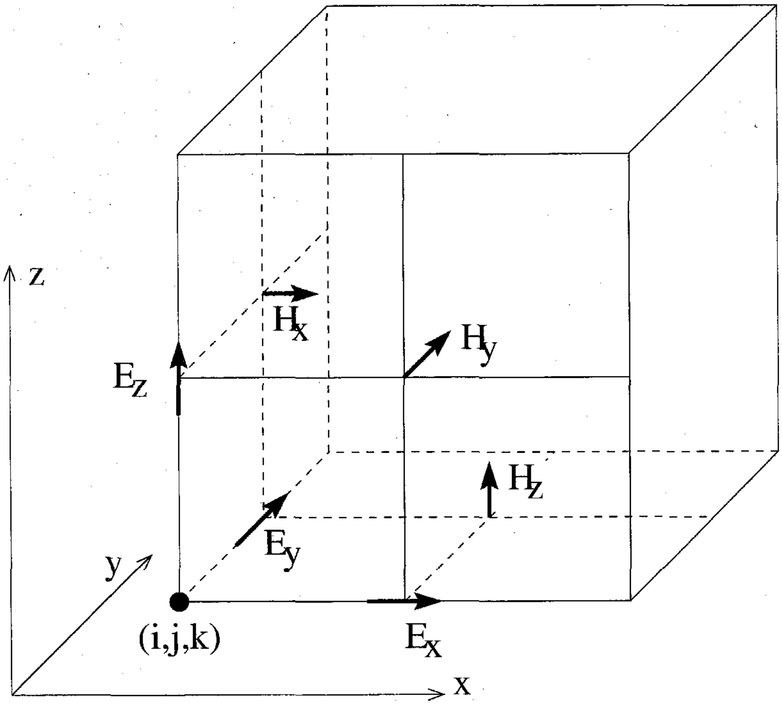

Figure 2.1: The position of field components in the FDTD lattice for grid point (i, j, k). The components of the dipole moment are placed in the same position as the electric field components and are not shown.

the differential equations with the grid points denoted as

$$(i, j, k) = (i\delta x, j\delta y, k\delta z) \tag{2.24}$$

and any function of space and time as

$$F^n(i, j, k) = F(i\delta x, j\delta y, k\delta z, n\delta t) \tag{2.25}$$

where δx, δy, and δz are the space increments in x, y, z directions, δt is the time increment, and the notation $F^n(i, j, k)$ denotes the (i, j, k, n) space-time mesh point.

The necessary difference equations can be derived using only two of the time dependent form of Maxwell's equations[1] following the method of Yee [49] and gener-

---

[1] Although only two of Maxwell's equations are used, the resulting solutions can be shown to satisfy all four of Maxwell's equations for the source-free Maxwell equations [49] or with non-zero electric polarization $\vec{P}$ [20]

alizing to include a non-zero electric polarization:

$$\mu_0 \frac{\partial \vec{H}}{\partial t} = -\nabla \times \vec{E} \tag{2.26}$$

$$\epsilon \frac{\partial \vec{E}}{\partial t} = \nabla \times \vec{H} - \frac{\partial \vec{P}}{\partial t} \tag{2.27}$$

The electromagnetic field and the dipole moment are discretized on the space grid as in Fig. 2.1. Applying the finite difference approximation to the equations results in a set of finite difference equations for the electromagnetic field. For the z-components of the electric field E_z and magnetic field H_z the difference equations take the form

$$\begin{aligned} E_z^{n+1}(i,j,k+\frac{1}{2}) &= E_z^n(i,j,k+\frac{1}{2}) \\ &+ \frac{\Delta t}{\epsilon(i,j,k+\frac{1}{2})}\left[\frac{H_y^{n+\frac{1}{2}}(i+\frac{1}{2},j,k+\frac{1}{2}) - H_y^{n+\frac{1}{2}}(i-\frac{1}{2},j,k+\frac{1}{2})}{\Delta x}\right. \\ &- \frac{H_x^{n+\frac{1}{2}}(i,j+\frac{1}{2},k+\frac{1}{2}) - H_x^{n+\frac{1}{2}}(i,j-\frac{1}{2},k+\frac{1}{2})}{\Delta y} \\ &\left. -(\dot{P}_z)^{n+\frac{1}{2}}(i,j,k+\frac{1}{2})\right] \end{aligned} \tag{2.28}$$

$$\begin{aligned} H_z^{n+\frac{1}{2}}(i+\frac{1}{2},j+\frac{1}{2},k) &= H_z^{n-\frac{1}{2}}(i+\frac{1}{2},j+\frac{1}{2},k) \\ &+ \frac{\Delta t}{\mu_0}\left[\frac{E_x^n(i+\frac{1}{2},j+1,k) - E_x^n(i+\frac{1}{2},j,k)}{\Delta y}\right. \\ &\left. - \frac{E_y^n(i+1,j+\frac{1}{2},k) - E_y^n(i,j+\frac{1}{2},k)}{\Delta x}\right] \end{aligned} \tag{2.29}$$

Note that the E_z and the H_z fields are evaluated on different time grids separated by a half-time step. Since the $\vec{E}$ and $\vec{H}$ fields are spatially displaced as seen in Fig. 2.1 (they are evaluated on different space meshes), they can also be evaluated on different time meshes resulting in a reduction of the required computational resources. The complete set of finite difference equations have been derived by Yee and given in reference [49]. These equations are then used to evolve the $\vec{E}$ and $\vec{H}$ field in the time domain at alternate half-time steps.

In section 2.3, a method for calculating the spontaneous emission rate from a dipole source represented by an electric polarization $\vec{P}$ will be derived where the polarization is assumed to have a δ-function spatial distribution. In the numerical calculation, however, such an idealization is difficult to realize due to the space discretization. δ-function spatial distributions will be approximated as being distributed uniformly in a unit cube. For example, for a z-polarized electric polarization located at grid point $(i, j, k + 1/2)$, only $P_z(i, j, k + 1/2)$ is non-zero, all P_x, P_y and other P_z are zero.

2.2.1 Boundary conditions

One difficulty with the FDTD algorithm is the need to terminate the computational mesh in space. From Eq. (2.28) and Eq. (2.29), it can be seen that our time stepping difference equations at any point in space (i, j, k) depend only on the nearest neighbour points of the other field mesh ($\vec{E} \rightarrow \vec{H}$ and vice versa). Borrowing a concept from finite difference techniques in computational fluid mechanics, this is shown schematically in Fig. 2.2 and is referred to as the computational molecule for the discretization. At any grid point (i, j, k) the total vector field ($\vec{H}$ or $\vec{E}$) will depend on the six nearest neighbour grid points. To solve the problem, the computational molecule must be applied at all grid points. Clearly, if the grid point lies on the boundary of the computational domain, all the nearest neighbours will not be available. Therefore, special boundary conditions are necessary to terminate the computational domain.

If the domain of interest is finite, the boundary conditions may be relatively simple. For example, a perfect metallic boundary will require the field to go to zero, which alleviates the need for the nearest neighbour points to determine the boundary points. For calculating infinitely periodic structures (such as an infinite photonic crystal lattice), Bloch boundary conditions can be used where the nearest neighbour points for one boundary are taken as the points on the opposing boundary with some phase factor. This is simply a numerical version of the Bloch theorem from solid state physics [42] applied to the electromagnetic equations. A much more difficult

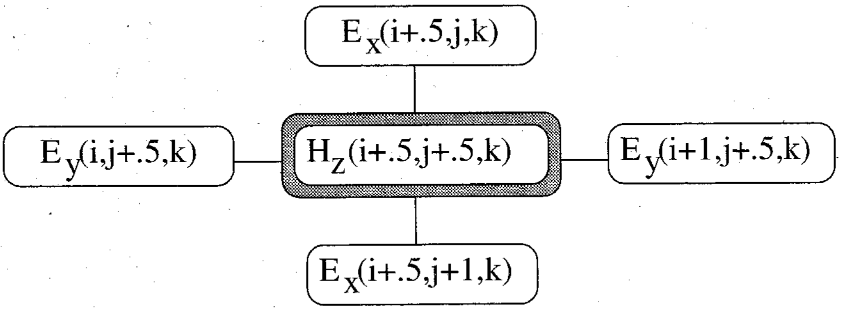

Figure 2.2: Computational molecule for the discrete time stepping of H_z. The updated (in time) H_z depends only on the previous time step for H_z and the nearest neighbours in E_x and E_y. The shaded box indicates the updated parameter.

problem occurs in trying to simulate unbounded domains, which will be discussed in the following section.

2.2.2 The perfectly matched boundary condition

One problem of performing calculations for microcavities or other finite structures, is the need to simulate an unbounded spatial domain. This is typically done by applying an absorbing boundary condition such that all incident radiation at the boundary is absorbed with negligible reflection (essentially a radiation condition). A commonly used and relatively simple boundary condition was proposed by Mur [51]. However, this boundary condition is known to show small reflection and high absorption only for incident radiation normal to the boundary. This requires that the boundary be placed at least several wavelengths away from any structure of interest thereby increasing the required computational resources.

An improved boundary condition is the perfectly matched layer [52] (PML), which is capable of absorbing an electromagnetic wave incident at any angle without reflection. Some properties of the PML medium will be discussed briefly. For a more detailed description consult the work of Berenger [52] and Gedney [53].

The perfectly matched layer can be viewed as a lossy uniaxial medium [53], characterized by parameters $(\sigma_x, \sigma_y, \sigma_z)$. Following Gedney [53], in the PML region

Maxwell's equations (Eq. (2.27)) can be written as

$$\nabla \times \vec{H} = \epsilon\tilde{\epsilon}\frac{\partial \vec{E}}{\partial t} \tag{2.30}$$

$$\nabla \times \vec{E} = \mu_0\tilde{\mu}\frac{\partial \vec{H}}{\partial t} \tag{2.31}$$

where we define

$$\tilde{\epsilon} = \tilde{\mu} = \begin{bmatrix} s_y s_z/s_x & 0 & 0 \\ 0 & s_x s_z/s_y & 0 \\ 0 & 0 & s_x s_y/s_z \end{bmatrix} \tag{2.32}$$

$$\begin{aligned} s_x &= 1 + \frac{\sigma_x}{i\omega\epsilon_0} \\ s_y &= 1 + \frac{\sigma_y}{i\omega\epsilon_0} \\ s_z &= 1 + \frac{\sigma_z}{i\omega\epsilon_0} \end{aligned} \tag{2.33}$$

Note that setting $(\sigma_x, \sigma_y, \sigma_z) = (0,0,0)$ in Eq. (2.32) and Eq. (2.33), then $\tilde{\epsilon}$ and $\tilde{\mu}$ are equal to the identity matrix and Eq. (2.30) is reduced to the regular Maxwell's equations (Eq. (2.27)). A dielectric medium can thus be regarded as a special case of a PML medium in which $(\sigma_x, \sigma_y, \sigma_z) = (0,0,0)$. The PML medium is then discretized in the same way as Eq. (2.28) and Eq. (2.29) according to Fig. 2.1. Note that this does not solve the problem of the boundary points since the discretization of Eq. (2.30) also involves the nearest neighbour dependence. The PML medium is therefore terminated using a perfect metal boundary condition following the method proposed by Berenger [54].

In the PML medium, if we restrict $\sigma_x(x,y,z) = \sigma_x(x)$ and similarly for σ_y and σ_z, the electromagnetic wave propagating in the PML medium will undergo absorption with no reflection [52]. In this case, any electromagnetic wave will not encounter any reflections at the interface of the PML medium except at the perfect metal outer boundary. However, the PML parameters ($\sigma_{(x,y,z)}$ and medium thickness) can be chosen such that the majority of the electromagnetic energy is absorbed on propagation through the PML medium and the field energy incident on the perfect metal is negligible. Even though in theory PML does not reflect any incident electromagnetic waves, it has been shown [52] that if σ_x, σ_y, and σ_z are constant within the PML region in the above computational domain, significant reflection may occur because of the discrete approximation at the interface between the computational domain of interest and the PML region. Therefore a spatial variation is required subject to the previous restriction. Following reference [53], σ can be varied along the normal axis of the PML interface to minimize the numerical reflection. For example, for the $\hat{z}$ normal interface region, the following form for σ_z is used

$$\sigma_z(z) = \frac{\sigma_{max}|z - z_0|^m}{d^m} \tag{2.34}$$

where z_0 is the position of the PML interface, d is the PML layer thickness and m is an arbitrary parameter. Similar spatial dependencies for $\sigma_x(x)$ and $\sigma_y(y)$ for the respective interface directions are used with the same σ_{max}. The parameters σ_{max}, d, and m are chosen to minimize reflection from the PML boundary for the particular problem.

2.3 Calculation of spontaneous emission

In principle, spontaneous emission lifetime should be determined through quantum electrodynamics[2]. However, it can be shown that the same result can be determined from classical electrodynamics [55]. In a classical picture, the dipole radiation field acts on an oscillating dipole and causes the dipole moment to decay, which accounts for the spontaneous emission. Following the methods outlined in section 2.2 for solving Maxwell's equations, the classical approach to spontaneous emission can be implemented numerically with relative ease providing a means to determine the spontaneous emission rate in any arbitrary dielectric structure describable by the finite difference time-domain method. Since determination of the spontaneous emission

---

[2] The quantum mechanical view of spontaneous emission will be considered in chapter 3

rate is an open radiation problem, the PML absorbing boundary condition proposed by Berenger [52] and briefly described in section 2.2.2, will be used.

2.3.1 Classical analysis of spontaneous emission

It is well known that although the phenomenon of spontaneous emission is quantum mechanical in nature, it can be understood within a classical framework [56]. In this section, it will be briefly shown that the quantum mechanical spontaneous emission rate can be determined from the rate of energy transfer from a classical radiating dipole to the electromagnetic field described by Maxwell's equations, Eq. (2.1) and Eq. (2.2).

The electric field of an oscillating dipole can be separated [41] into a longitudinal or irrotational part that has $\nabla \times \vec{E}_{long} = 0$ and a transverse or solenoidal part that has $\nabla \cdot \vec{E}_{tran} = 0$. In the coulomb gauge, it can be shown that the transverse radiation field is given by the vector potential alone and that the wave equation for the vector potential can be expressed entirely in terms of the transverse current[3]. The longitudinal electric field is the unretarded Coulomb field due to the dipole source and the surrounding dielectric environment and does not contribute to the dipole radiation power [41]. In the following, the longitudinal field will be neglected and the subscripts *tran* and *long* will be dropped. The transverse electric field of an oscillating dipole in an inhomogeneous charge-free medium must satisfy the generalized transverse field condition [57]:

$$\nabla \cdot \Big(\epsilon(\vec{r})\vec{E}(\vec{r},t)\Big) = 0 \tag{2.35}$$

and the transverse electric field wave equation can be written as

$$\nabla \times \nabla \times \vec{E}(\vec{r},t) + \epsilon(\vec{r})\mu_0 \frac{\partial^2 \vec{E}(\vec{r},t)}{\partial t^2} + \mu_0 \frac{\partial^2 \vec{P}(\vec{r},t)}{\partial t^2} + \mu_0 \frac{\partial \vec{J}(\vec{r},t)}{\partial t} = 0 \tag{2.36}$$

---

[3] This is the origin of the alternate names, "radiation gauge" or "transverse gauge" for this choice of gauge.

where $\epsilon(\vec{r})$ is the spatially dependent dielectric constant. The inhomogeneous medium will be assumed to be a linear, lossless dielectric such that $\epsilon(\vec{r})$ can be assumed to be a real number. However, these results can be easily generalized to account for medium loss or amplification (complex $\epsilon(\vec{r})$). The electric polarization in Eq. (2.36) represents a point dipole source which is assumed to oscillate in time with magnitude $d(t)$ at $\vec{r} = \vec{r}_0$.

$$\vec{P}(\vec{r},t) = d(t)\,\hat{d}\,\delta(\vec{r}-\vec{r}_0) \tag{2.37}$$

where $\hat{d}$ is the polarization of the oscillating dipole. For convenience, a dissipation current $\vec{J}(\vec{r},t)$ proportional to the electric field and with magnitude γ, has been included in Eq. (2.36):

$$\vec{J}(\vec{r},t) = \gamma\epsilon(\vec{r})\vec{E}(\vec{r},t) \tag{2.38}$$

The proportionality constant γ will later be set to zero in the case of a lossless dielectric medium. The radiation electric field is now expanded in terms of a complete set of orthonormal transverse modes $\{\vec{F}_n(\vec{r})\}$ with mode frequencies $\{\omega_n\}$, as defined in reference [57]

$$\vec{E}(\vec{r},t) = \sum_n \alpha_n(t)\vec{F}_n(\vec{r}) \tag{2.39}$$

satisfying the eigenmode equation

$$\nabla \times \nabla \times \vec{F}_n(\vec{r}) = \epsilon(\vec{r})\mu_0\omega_n^2\vec{F}_n(\vec{r}) \tag{2.40}$$

and the orthonormality condition

$$\int d^3r\,\epsilon(\vec{r})\vec{F}_n^*(\vec{r})\cdot\vec{F}_m(\vec{r}) = \delta_{m,n} \tag{2.41}$$

Substituting the electric polarization due to the dipole Eq. (2.37), the dissipation current Eq. (2.38) and the modal expansion Eq. (2.39) into the transverse field wave equation Eq. (2.36), we have

$$\mu_0\epsilon(\vec{r})\sum_n\left[\ddot{\alpha}_n(t)+\gamma\dot{\alpha}_n(t)+\frac{\alpha_n(t)}{\mu_0\epsilon(\vec{r})}\nabla\times\nabla\times\right]\vec{F}_n(\vec{r})=-\mu_0\ddot{d}(t)\,\hat{d}\,\delta(\vec{r}-\vec{r}_0) \tag{2.42}$$

and then using the eigenmode equation Eq. (2.40) and the orthonormality condition Eq. (2.41), the equation of motion for the mode amplitude $\alpha_n(t)$ is,

$$\ddot{\alpha}_n(t)+\gamma\dot{\alpha}_n(t)+\omega_n^2\alpha_n(t)=-\ddot{d}(t)\left[\hat{d}\cdot\vec{F}_n^*(\vec{r}_0)\right] \tag{2.43}$$

Assuming a perfect harmonic dipole oscillation $d(t)=\mu\exp\left(-i\omega_0 t\right)$, the modal equation of motion, Eq. (2.43), can be solved for the mode amplitude time dependence:

$$\alpha_n(t)=d(t)\frac{\omega_0^2}{\omega_n^2-\omega_0^2-i\omega_0\gamma}\left[\hat{d}\cdot\vec{F}_n^*(\vec{r}_0)\right] \tag{2.44}$$

The dipole emission power is given by the integral [41]

$$P_{classical}=\frac{-1}{2}Re\left\{\int d^3r\frac{\partial\vec{P}^*(\vec{r},t)}{\partial t}\cdot\vec{E}(\vec{r},t)\right\} \tag{2.45}$$

Substitute the mode expansion Eq. (2.39) and Eq. (2.44) into the above equation, the result for the classical spontaneous emission power is

$$P_{classical}=\frac{1}{4}\omega_0^2\mu^2\sum_n\left|\hat{d}\cdot\vec{F}_n(\vec{r}_0)\right|^2\frac{\gamma/2}{(\omega_n-\omega_0)^2+\gamma^2/4} \tag{2.46}$$

Under the previous assumption of a lossless medium, the classical radiation power is given in the limit of $\gamma \to 0$ as [4]:

$$P_{classical} = \frac{1}{4}\pi\mu^2\omega_0^2 \sum_n \left|\hat{d}\cdot\vec{F}_n(\vec{r}_0)\right|^2 \delta(\omega_n - \omega_0) \tag{2.47}$$

Compare the above result with that for the spontaneous emission power derived from cavity quantum electrodynamics considerations [55, 57]

$$P_{quantum} = \hbar\omega_{eg}R_{sp} = \pi\omega_{eg}^2\mu_{eg}^2 \sum_n |\hat{d}\cdot\vec{F}_n(\vec{r}_0)|^2\delta(\omega_n - \omega_{eg}) \tag{2.48}$$

where ω_{eg} is the transition frequency from the excited state to the ground state, μ_{eg} is the dipole matrix element between the excited state and the ground state and R_{sp} is the spontaneous emission rate given by Fermi's golden rule. It should be noted that this is the same result as we will find in chapter 3, Eq. (3.37), when the different mode normalization conventions are taken into account. If we identify μ and ω_0 in Eq. (2.47) with μ_{eg} and ω_{eg} in Eq. (2.48), respectively, the two expressions only differ by a factor of 4. This constant proportionality allows us to calculate the spontaneous emission rate using the classical dipole radiation power $P_{classical}$. For the spontaneous emission lifetime $\tau_{spon}^{bulk} = 1/R_{sp}^{bulk}$ in bulk material and the spontaneous emission lifetime $\tau_{spon} = 1/R_{spon}$ in some arbitrary inhomogeneous dielectric medium of interest, after dividing Eq. (2.48) by Eq. (2.47),

$$\frac{\tau_{spon}^{bulk}}{\tau_{spon}} = \frac{R_{sp}}{R_{sp}^{bulk}} = \frac{P_{classical}}{P_{classical}^{bulk}} \tag{2.49}$$

where $P_{classical}$ is the classical radiation power for a dipole in the structure of interest, and $P_{classical}^{bulk}$ is the classical dipole emission power in a bulk dielectric material.

This relation, Eq. (2.49), therefore provides a method to calculate the quantum mechanical modification of the spontaneous emission rate (as described in chapter

---

[4] The Lorentzian lineshape function in this limit becomes a delta function:

$$\lim_{\gamma\to 0} \frac{\gamma/2}{(\omega_n - \omega_0)^2 + \gamma^2/4} = \pi\delta(\omega_n - \omega_0)$$

3) through the classical Maxwell's equations. First, the classical radiation field for a dipole in the structure is calculated using the finite-difference technique of section 2.2 and the radiated power is determined by integration of the Poynting vector over a surface enclosing the dipole source. Comparison with radiation power of the same dipole in a homogeneous medium (bulk), according to Eq. (2.49) will give the quantum mechanical modification of the spontaneous emission lifetime. An example of this calculation for a dielectric slab waveguide is shown in Fig. 2.3 for a discretized slab thickness of 10 cells. Since the source dipole is centered in the slab, primarily the even modes are excited as seen by the enhanced peak in the spontaneous emission rate near the cutoff for the second TE mode. Weaker peaks in the spontaneous emission rate are seen for the odd modes (TE_1 and TE_3) because of the discretization error approximating the dipole source as uniformly distributed across the computational unit cell, which allows some coupling with the odd modes.

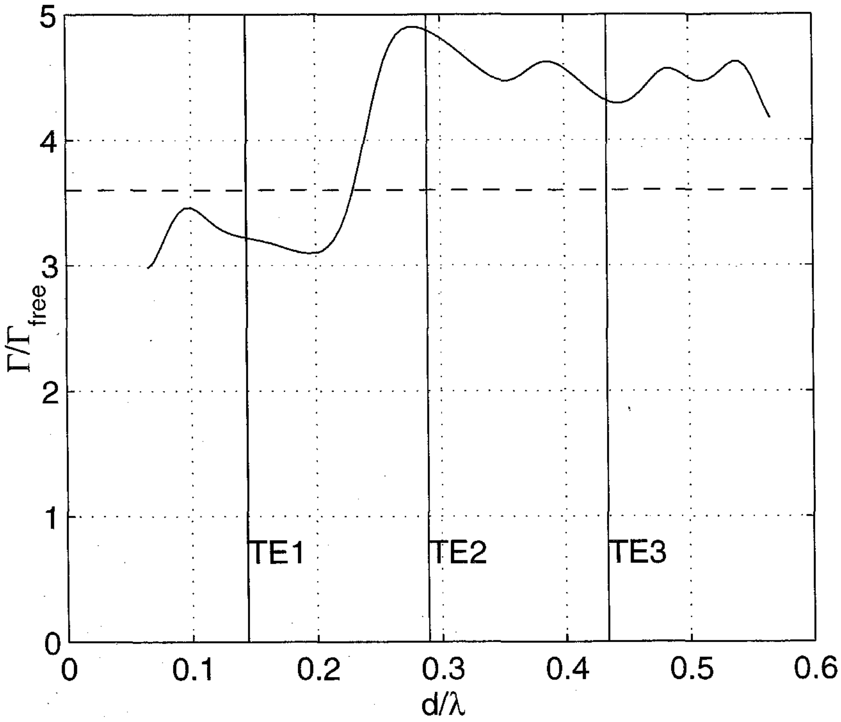

Figure 2.3: Calculated spontaneous emission rate from a dielectric slab for transverse electric(TE) modes using a three-dimensional finite difference algorithm. The vertical lines indicate the cutoff frequencies for different TE modes. The horizontal dashed line indicates the expected bulk rate enhancement ($\Gamma \approx n\Gamma_{free}$).

Chapter 3 Modified spontaneous emission

3.1 Introduction

The interaction of an electromagnetic field with an atom is commonly discussed in terms of *Fermi's Golden Rule*, a well known relation that describes the transition probability between electronic states in the presence of an electromagnetic field. Given an electronic system, the spontaneous emission rate can then be calculated. However, blind application of this relation can lead to the belief that the spontaneous emission rate is a fixed property of the electronic or atomic system. In 1946, E.M. Purcell predicted [14] that if the electronic system was coupled to a resonator, the spontaneous emission rate could be strongly modified due to the properties of the resonator. Additionally, the spontaneous emission rate is also modified when the emitter is embedded in a dielectric host where the rate is scaled by the real part of the refractive index at the transition frequency [58, 59, 60, 61]. This and related effects have been extensively studied in the field of cavity quantum electrodynamics. However, the basis of Purcell's prediction extends beyond resonators. The spontaneous emission is dependent on the local electromagnetic environment in addition to the electronic structure. The interaction of an atomic or any general electronic system with a complex electromagnetic environment must be considered carefully.

Microcavities formed using photonic bandgap crystals have been frequently suggested for light emitting devices exhibiting strongly modified spontaneous emission [7, 62]. Due to the possibility of strong photonic crystal reflectivity over a relatively large spectral bandwidth and solid angle, such structures are promising candidates for significantly modified spontaneous emission behavior. Spontaneous emission from semiconductor microcavities of various geometries based on photonic crystal structures has been experimentally examined [11, 63, 64, 65]. In fact, lasing in these photonic bandgap microcavities has been reported [66]. Lasing in similar but smaller microcavities will be discussed in chapter 5 and have been reported in [67, 68].

3.2 Quantized electromagnetic field

The quantization of the electromagnetic field in a medium with a non-uniform dielectric constant ϵ is similar to the method used for a uniform dielectric constant system except that the eigenmodes are no longer plane waves [57]. Beginning with the classical Maxwell equations (in MKS units) assuming no free charges or currents

$$\nabla \times \vec{H} = \frac{\partial \vec{D}}{\partial t} \tag{3.1}$$

$$\nabla \cdot \vec{B} = 0 \tag{3.2}$$

$$\nabla \times \vec{E} = -\frac{\partial \vec{B}}{\partial t} \tag{3.3}$$

$$\nabla \cdot \vec{D} = 0 \tag{3.4}$$

with the constitutive relations

$$\vec{B} = \mu \vec{H} \qquad \vec{D} = \epsilon \vec{E} \tag{3.5}$$

we introduce the vector potential $\vec{A}$, which is related to the electric and magnetic fields.

$$\vec{E} = -\frac{\partial \vec{A}}{\partial t} \tag{3.6}$$

$$\vec{B} = \nabla \times \vec{A} \tag{3.7}$$

Substituting the vector potential in Maxwell's equations yields a vector wave equation of the form

$$\nabla \times \nabla \times \vec{A} = \mu\epsilon \frac{\partial^2}{\partial t^2} \vec{A} \tag{3.8}$$

In the case of uniform dielectric constant, the solutions to this vector wave equation Eq. (3.8) takes the form of plane waves. For arbitrary $\epsilon = \epsilon(\vec{r})$, we will assume that the solutions of Eq. (3.8) form a complete set of orthogonal modes. In this case, the canonical quantization procedure can be applied by the introduction of the photon creation and annihilation operators, $a^\dagger$ and a. Then, the operator of the vector potential can be written as a sum over the normal modes for the system [69]

$$\hat{A}(\vec{r},t) = \sum_{c=0}^{N} \sqrt{\frac{\hbar}{2V_c\epsilon(\vec{r})\omega_c}} \left(\mathrm{a}_c \vec{A}_c(\vec{r}) \mathrm{e}^{i\omega_c t} - \mathrm{a}_c^\dagger \vec{A}_c^*(\vec{r}) \mathrm{e}^{-i\omega_c t} \right) \tag{3.9}$$

where the mode function has been normalized to satisfy

$$\int_c \epsilon(\vec{r}) \frac{\hbar\omega_c}{2V_c\epsilon(\vec{r})} \left|\vec{A}_c\right|^2 d^3r = \int_c \epsilon(\vec{r}) \left|\vec{E}_c\right|^2 d^3r = \frac{\hbar\omega_c}{2} \tag{3.10}$$

for each mode and the integration extends over the quantization volume. In Eq. (3.9) $\vec{A}_c(\vec{r})$ describes the spatial distribution of the classical eigenmode c at a frequency ω_c. The operators for the electric and magnetic fields are simply derived using Eq. (3.6) and Eq. (3.7).

$$\begin{aligned} \hat{E}(\vec{r},t) &= -i \sum_{c=0}^{N} \sqrt{\frac{\hbar\omega_c}{2V_c\epsilon(\vec{r})}} \left(\mathrm{a}_c \vec{A}_c(\vec{r}) \mathrm{e}^{i\omega_c t} - \mathrm{c.c.} \right) & (3.11) \\ \hat{B}(\vec{r},t) &= \sum_{c=0}^{N} \nabla \times \vec{A}_c(\vec{r}) & (3.12) \end{aligned}$$

Then, using Eq. (3.11) and Eq. (3.12), the Hamiltonian for the electromagnetic field is

$$\begin{aligned} \mathcal{H}_{em} &= \frac{1}{8\pi} \int d^3r \left(\hat{E} \cdot \hat{E}^\dagger + \hat{H} \cdot \hat{H}^\dagger \right) & (3.13) \\ &= \sum_c \hbar\omega_c \left(\mathrm{a}_c^\dagger \mathrm{a}_c + \frac{1}{2} \right) & (3.14) \end{aligned}$$

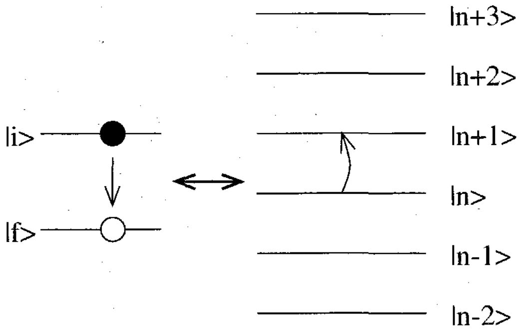

Figure 3.1: Transition of a two-level electronic system (left) coupled to a quantized electromagnetic field (right).

3.3 The dipole approximation in semiconductor quantum wells

In this section the dipole approximation in a semiconductor quantum well is briefly considered, within the context of arbitrary electromagnetic field solutions of section 3.2. The classical electromagnetic fields will be used; however, the results are easily extended for quantized field solutions.

The interaction Hamiltonian of a single electron in a quantum well with an electromagnetic field within a single band, effective mass model for the semiconductor is given by [69]

$$\mathcal{H}(\vec{r},t) = \frac{1}{2m_*}\left(P - qA(\vec{r},t)\right)^2 + qV + \mathcal{H}_{em} \tag{3.15}$$

where m^* is the effective mass, V is the unperturbed quantum well potential function, and $\mathcal{H}_{em}$ is the electromagnetic field portion of the Hamiltonian. The single band effective mass model for the semiconductor quantum well simplifies the problem to one similar to a simple two-level electronic system coupled to the electromagnetic field as shown in Fig. 3.1. The details of the electronic wavefunction within this approximation will not be considered. The Hamiltonian can be separated into the unperturbed quantum well contribution:

$$\mathcal{H}_{qw} = \frac{P^2}{2m^*} + V \tag{3.16}$$

the 'atom'-field interaction contribution

$$\mathcal{H}' = -\frac{q}{2m^*}\left(P \cdot \vec{A}(\vec{r},t) + \vec{A}(\vec{r},t) \cdot P\right) + \frac{q^2}{2m^*}A^2(\vec{r},t) \tag{3.17}$$

and the unperturbed field portion given in Eq. (3.14). As discussed in section 3.2, the vector potential in a domain with an inhomogeneous dielectric constant has a normal mode expansion given by Eq. (3.9). We will consider a single mode, and dropping the c subscripts for notational simplicity, the vector potential is given as

$$\vec{A}(\vec{r},t) = \vec{A}(\vec{r})\mathrm{e}^{i\omega t} + \text{c.c.} \tag{3.18}$$

3.3.1 The linear term

It can be easily verified that the commutator of P and A is given by

$$\left[P, \vec{A}(\vec{r},t)\right] = -i\hbar\nabla \cdot \vec{A}(\vec{r},t) \tag{3.19}$$

The term $\nabla \cdot \vec{A}$ is simply determined by the choice of gauge. P and A commute in the case of the Coulomb gauge [41], in which $\nabla \cdot \vec{A} = 0$. In this case, the linear interaction term can be written as

$$\mathcal{H}'_{linear} = -\frac{q}{m^*}P \cdot \vec{A}(\vec{r},t) \tag{3.20}$$

The matrix elements of this interaction term of the Hamiltonian will have the form

$$\mathcal{H}'_{ij} = -\frac{q}{m^*}\left\langle i \left| P \cdot \vec{A}(\vec{r},t) \right| j \right\rangle \tag{3.21}$$

Typically for optical frequencies, the variation in the photon field (represented by $\vec{A}(\vec{r},t)$) is slow compared to either the atomic wavefunctions or the inter-atomic spacing. In this case, over the electron wavefunction $|j\rangle$, the vector potential can be taken as a constant at the atomic position $\vec{R}_0$ so that $\vec{A}(\vec{r},t) = \vec{A}(\vec{R}_0,t)$ can be taken outside the inner product (the dipole approximation [70]). This simplifies the matrix element to be

$$\mathcal{H}'_{ij} = -\frac{q}{m^*}\vec{A}(\vec{R}_0,t)\cdot\langle i\,|P|\,j\rangle \tag{3.22}$$

where we have used commutation of $\vec{A}$ and P. From the definition of the vector potential in Eq. (3.6) and the form of the vector potential modes in Eq. (3.9),

$$\mathcal{H}'_{ij} = -\frac{iq}{\omega m^*}\vec{E}(\vec{R}_0,t)\cdot\langle i\,|P|\,j\rangle \tag{3.23}$$

Using the operator equivalence [71] the matrix element of the momentum operator between two states i, j can be written as[1]

$$\langle i\,|[\mathcal{H}_{qw},\hat{r}]|\,j\rangle \equiv \left\langle i\left|\frac{i\hbar}{m^*}P\right|j\right\rangle \tag{3.24}$$

Inserting this relation into the interaction matrix element and introducing the energy difference between the two electronic states (which is also equal to the photon energy ω) $\omega = (E_i - E_j)/\hbar$ this gives [72]

$$\mathcal{H}'_{ij} = -\frac{iq}{\omega m^*}\vec{E}(\vec{R}_o,t)\cdot\omega\hbar\frac{m^*}{i\hbar}\langle i\,|\hat{r}|\,j\rangle \tag{3.25}$$

This gives the traditional simple dipole interaction term [2]

$$H'_{linear} = -q\vec{E}(\vec{r},t)\cdot\vec{r}_{ij} \tag{3.26}$$

---

[1] This can be shown using the definitions $[p,r] = i\hbar$ and $\mathcal{H}_{qw} = p^2/2m^*$.

[2] This interaction term can also be derived from the multipolar form for the Hamiltonian by a unitary transformation of the $P\cdot\vec{A}$ form (the minimal coupling form). See [73].

The derivation of Eq. (3.26) shows that the dipole approximation and the electric dipole form of the interaction ($\vec{E}\cdot\vec{r}$) is not dependent on the assumption of plane-wave solution for the electromagnetic field. The dipole approximation is valid for arbitrary field solutions under the assumptions that the intensity is low (neglect the A^2 term as shown in the following section) and that the spatial variations of the field are slow compared to the electronic wavefunctions.

3.3.2 The A^2 term

Using the electromagnetic mode described by Eq. (3.18) and the interaction Hamiltonian $\mathcal{H}'$ from Eq. (3.17), the matrix element for the A^2 interaction term between two states Ψ_i and Ψ_f becomes

$$W_{A^2} \equiv \left\langle \Psi_f \left| \frac{q^2 \left|\vec{A}(r)\right|^2}{m^*} \left[1 + \cos\left(2\omega t\right)\right] \right| \Psi_i \right\rangle \tag{3.27}$$

Under the dipole approximation, the vector potential is assumed to vary slowly as compared to the spatial extent of the electronic wavefunctions at location r_0. Consider a Taylor expansion of the vector potential

$$\vec{A}(\vec{r}+\vec{r_0}) = \vec{A}(\vec{r_0}) + \vec{r}\cdot\nabla\vec{A}(\vec{r_0}) + \frac{|\vec{r}|^2}{2!}\nabla^2\vec{A}(\vec{r_0}) + O\left(\vec{r}|\vec{r}|^2\right) \tag{3.28}$$

$$\begin{aligned}\left|\vec{A}(\vec{r}+\vec{r_0})\right|^2 &= |\vec{A}(\vec{r_0})|^2 + 2\vec{r}\cdot\nabla\vec{A}(\vec{r_0})\cdot\vec{A}(\vec{r_0}) + \\ &\quad |\vec{r}|^2\left(\left[\nabla\vec{A}(\vec{r_0})\right]^2 + \vec{A}(\vec{r_0})\cdot\nabla^2\vec{A}(\vec{r_0})\right) + O\left(|\vec{r}|^3\right)\end{aligned} \tag{3.29}$$

The matrix element then becomes

$$\begin{aligned}W_{A^2} &= \frac{q^2\left(1+\cos\left(2\omega t\right)\right)}{m^*(z)} \times \left\langle \Psi_f \left| |\vec{A}(\vec{r_0})|^2 + 2\vec{r}\cdot\nabla\vec{A}(\vec{r_0})\cdot\vec{A}(\vec{r_0}) + \right.\right. \\ &\quad \left.\left. + |\vec{r}|^2\left(\left[\nabla\vec{A}(\vec{r_0})\right]^2 + \vec{A}(\vec{r_0})\cdot\nabla^2\vec{A}(\vec{r_0})\right) + O\left(|\vec{r}|^3\right) \right| \Psi_i \right\rangle\end{aligned} \tag{3.30}$$

Due to orthogonality, the first term of this matrix element is zero since the two electronic states Ψ_i and Ψ_f are different. The second term is non-zero and is dependent on

$$\vec{A}(\vec{r_0})\cdot\nabla\vec{A}(\vec{r_0})\cdot\vec{r}_{fi} \tag{3.31}$$

where $\vec{r}_{fi}$ is the dipole matrix element between the two electronic states. We saw in the previous section that $\vec{A}(\vec{r_0})$ has a magnitude proportional to $\vec{E}(\vec{r_0})$ (also see Eq. (3.6)). The factor involving $\nabla\vec{A}(\vec{r_0})$ is small by assumption that over the extent of the electronic wavefunctions, the vector potential is slowly varying. If the vector potential is nearly constant, then the gradient must also be small. Clearly, therefore, the term containing Eq. (3.31) is small compared to the dipole term from Eq. (3.26).

It can be shown [70, 73] that for all weak or moderately intense fields at optical frequencies, the term resulting from $|\vec{A}|^2$ is small and can be neglected. Only at extremely high intensities, where multi-photon processes dominate, will it become necessary to include this term. The contribution due to this term will be ignored hereafter.

3.4 Spontaneous transition rate

In general, the electric field for an arbitrary dielectric structure (e.g. $\epsilon = \epsilon(\vec{r})$) can be written as an expansion over the normal modes of the system. Following Eq. (3.11),

$$\vec{E}(\vec{r},t) = \sum_{c=0}^{N} -i\sqrt{\frac{\hbar\omega_c}{2V_c\epsilon(\vec{r})}}\left(\mathrm{a}_c^\dagger(t)\vec{F}_c^*(\vec{r}) - \mathrm{a}_c(t)\vec{F}_c(\vec{r})\right) \tag{3.32}$$

where $\mathbf{a}_c^\dagger$ and $\mathbf{a}_c$ are the raising and lowering operators for photons into mode c. Assume now that the interaction Hamiltonian can be approximated as

$$\mathcal{H}' = -q\vec{E}(\vec{r},t)\cdot\hat{r} \tag{3.33}$$

We can write the transition probability as

$$R_{fi} = \frac{2\pi}{\hbar} \left|\mathcal{H}'\right|^2 \delta(E_{\text{initial}} - E_{\text{final}}) \tag{3.34}$$

For an electromagnetic system described by Eq. (3.32), this is

$$\begin{aligned} R_{fi}(\vec{r},\nu) \; &= \; \frac{e^2}{\hbar^2} \sum_c \frac{\hbar\omega_c}{2V_c} \left| \left\langle 1, n_c + 1 \left| \frac{1}{\sqrt{\epsilon(\vec{r})}} \left(\mathrm{a}_c^\dagger \vec{F}_c^*(\vec{r}) - \mathrm{a}_c \vec{F}_c(\vec{r}) \right) \cdot \hat{r} \right| 2, n_c \right\rangle \right|^2 \times \\ & \quad\; \delta(\nu_{\text{initial}} - \nu_{\text{final}}) \end{aligned} \tag{3.35}$$

Assume that the electric field can be taken as constant over the size of the atom. This is equivalent to saying that the electric field is slowly varying compared to the electronic wavefunctions $|n\rangle$. Also assume that the dielectric constant $\epsilon(\vec{r})$ is slowly varying compared to the wavefunction. The electric field terms can then be taken outside the inner product. We also note that for spontaneous emission, we are only interested in the transition by which the mode photon number is increased by one quanta. Introducing the local field polarization for a mode $\hat{\mathrm{e}}_c = \vec{F}_c / \left|\vec{F}_c\right|$, and the atom position in the lab frame of reference, $\vec{R}$, the transition rate for emission is

$$R_{fi}(\vec{R},\nu) = \frac{e^2}{\hbar^2} \sum_c \frac{\hbar\omega_c}{2V_c} \frac{\left|F_c(\vec{R})\right|^2}{\sqrt{\epsilon(\vec{R})}} \left|\left\langle 1, n_c + 1 \left| (\hat{\mathrm{e}}_c \cdot \hat{r})\, \mathrm{a}_c^\dagger \right| 2, n_c \right\rangle\right|^2 \delta(\nu_{\text{initial}} - \nu_{\text{final}}) \tag{3.36}$$

In order to simplify this expression, we introduce the dipole matrix element $\vec{r}_{12} \equiv \langle 1 \left| \vec{r} \right| 2 \rangle$. The photon creation operator $\mathrm{a}_c^\dagger$ has eigenvalue $n_k + 1$, where the n_k term gives rise to stimulated emission and spontaneous emission. Then, the spontaneous emission rate is

$$R_{sp}(\vec{R},\nu) = \frac{e^2}{\hbar^2} \sum_c \frac{\hbar\omega_c}{2V_c} \frac{\left|F_c(\vec{R})\right|^2}{\sqrt{\epsilon(\vec{R})}} \left|\hat{\mathrm{e}}_c \cdot \vec{r}_{12}\right|^2 \delta(\nu_{\text{initial}} - \nu_{\text{final}}) \tag{3.37}$$

3.5 Spontaneous emission in a microcavity

Following the procedure in the previous section, assume that the electromagnetic field expansion is given by Eq. (3.32) and that the transition probability is given as Eq. (3.34). Then, for a harmonic perturbation in time, the transition rate between two states can be expressed by Fermi's Golden Rule.

$$R_{fi}(\nu) = \frac{1}{\hbar^2} \left|\mathcal{H}'_{fi}\right|^2 \delta\left(\frac{E_i - E_f}{2\pi\hbar} - \nu\right) \tag{3.38}$$

Therefore, we can write the transition rate between two states f and i where the atomic system goes from state 2 to state 1 and the photon number in the mode increases by 1 using Eq. (3.34) and Eq. (3.33).

$$R_{fi}(\nu) = \frac{e^2}{\hbar^2} \sum_c \frac{\hbar\omega_c}{2V_c} \left| \left\langle 1, n_c + 1 \left| \mathbf{a}_c^\dagger \frac{\vec{F}_c^*(\vec{r}) \cdot \vec{r}}{\sqrt{\epsilon(\vec{r})}} - \mathbf{a}_c \frac{\vec{F}_c(\vec{r}) \cdot \vec{r}}{\sqrt{\epsilon(\vec{r})}} \right| 2, n_c \right\rangle \right|^2 \delta(\nu_\xi - \nu) \tag{3.39}$$

where the energy difference between the two electronic states has been taken as $E_i - E_f = 2\pi\hbar\nu_\xi$. Eq. (3.39) can be separated into two terms which represent the stimulated and spontaneous emission rates. We can simplify this expression by writing only the spontaneous rate into a particular mode of interest, c

$$R_c(\nu) = \frac{\omega_c}{2\hbar V_c} \left| \left\langle 1 \left| \frac{e\vec{F}_c^*(\vec{r}) \cdot \vec{r}}{\sqrt{\epsilon(\vec{r})}} \right| 2 \right\rangle \right|^2 \delta(\nu_\xi - \nu) \tag{3.40}$$

The electromagnetic spatial function as well as the spatially dependent permittivity, $\epsilon(\vec{r})$ are assumed to vary slowly compared to the atomic wavefunctions, $|1\rangle$ and $|2\rangle$. If this is the case then the mode and permittivity spatial functions can be taken out of the wavefunction inner product.

$$\left\langle 1 \left| \frac{e\vec{F}_c^*(\vec{r}) \cdot \vec{r}}{\sqrt{\epsilon \vec{r}}} \right| 2 \right\rangle \simeq \frac{\vec{F}_c^*(\vec{R})}{\sqrt{\epsilon(\vec{R})}} \cdot \langle 1 \left| e\vec{r} \right| 2\rangle = \frac{\vec{F}_c^*(\vec{R})}{\sqrt{\epsilon(\vec{R})}} \cdot \vec{\mu}_{12} \tag{3.41}$$

where $\vec{R}$ is the position of the atomic nucleus. This is essentially a repetition of the dipole approximation shown in Eq. (3.37). To specialize to the case of high-Q cavities, we must take into account both the finite lifetime of the atomic transition (characterized by the homogeneous lineshape function $g_h(\nu - \nu_\xi)$ for a transition centered at frequency ν_ξ), the homogeneous broadening, as well as the lineshape g_c, which results from the cavity photon lifetime. The inclusion of the atomic transition center frequency, which can be different than that for the cavity lineshape function, accounts for the cavity and the transition to be misaligned. If we consider first a transition where there is some uncertainty in the final state energy, we can introduce the atomic lineshape function $g_h(\nu - \nu_\xi)$, which represents the normalized lineshape due to homogeneous broadening of the transition centered around a frequency ν_ξ. In this case, the transition rate becomes

$$\begin{aligned} R_{fi}^{homog.\ part}(\nu) &= \frac{1}{\hbar^2}\left|\mathcal{H}'_{fi}\right|^2 \int \delta\left(\frac{E_i - E_f}{2\pi\hbar} - \nu\right) g_h(\nu - \nu_\xi)\, d\left(\frac{E_f}{2\pi\hbar}\right) & (3.42) \\ &= \frac{1}{\hbar^2}\left|\mathcal{H}'_{fi}\right|^2 \int \delta\left(\nu_\xi - \nu'\right) g_h(\nu - \nu')\, d\nu' & (3.43) \\ &= \frac{1}{\hbar^2}\left|\mathcal{H}'_{fi}\right|^2 g_h(\nu - \nu_\xi) & (3.44) \end{aligned}$$

To calculate the total spontaneous emission rate, we also need to take into account the inhomogeneous broadening, the distribution in energy of the electron-hole pairs, and then average over spatial positions. Take the inhomogeneous lineshape function as $g_i(\nu_\xi - \nu_{\xi_0})$, which is understood as being a distribution of transition center frequencies ν_ξ centered around ν_{ξ_0}. The spatial averaging can be taken by integrating over the active region. The total spontaneous transition rate (transitions per second) can then be calculated by integrating over transition center frequencies, ν_ξ, and then over all frequencies will give the total transition rate into a mode c.

$$\begin{aligned} R_c = \int_{V_a}\int_0^\infty\int_0^\infty\int_0^\infty \frac{\omega_c}{2\hbar V_c}\left|\frac{\vec{F}_c^*(\vec{R})\cdot\vec{\mu}_{12}}{\sqrt{\epsilon(\vec{R})}}\right|^2 \times \qquad (3.45) \\ g_c(\nu - \nu_c) g_h(\nu - \nu') N_i(\vec{R}) g_i(\nu_\xi - \nu_{\xi_0}) \delta(\nu_\xi - \nu')\, d\nu\, d\nu_\xi\, d\nu'\, d^3R \end{aligned}$$

where N_i is the density of excited state atoms such that $N_i g_i(\nu_\xi - \nu_{\xi_0})$ is the net excited state distribution. Define the average cavity dielectric permittivity using the property that the energy in the electric field for the mode with no photons is $\hbar\omega/2$.

$$\epsilon_{avg} \int_c E^2 d^3r = \epsilon_{avg} \int_c \frac{\hbar\omega_c}{2V_c} \left| \frac{\vec{F}_c^*(\vec{r})}{\sqrt{\epsilon(\vec{r})}} \right|^2 d^3r = \frac{\hbar\omega_c}{2} \tag{3.46}$$

This differs slightly from the normalization given by Eq. (3.10) to take into account the general situation of arbitrary $\epsilon(\vec{r})$. We can also define the mode filling factor Γ_r [74], which measures the alignment between the active region and the cavity mode.

$$\Gamma_r \overline{N_i} = \left(\int_a N_i(\vec{R}) \left| \frac{\vec{F}_c^*(\vec{r})}{\sqrt{\epsilon(\vec{r})}} \right|^2 d^3r \right) \Bigg/ \left(\frac{1}{V_c} \int_{cavity} \left| \frac{\vec{F}_c^*(\vec{r})}{\sqrt{\epsilon(\vec{r})}} \right|^2 d^3r \right) \tag{3.47}$$

where we have defined the total number of excited atoms in the cavity:

$$\overline{N_i} = \int_c N_i(\vec{R}) d^3R \tag{3.48}$$

Then, the total spontaneous emission rate reduces to

$$R_c = \frac{\omega_c \Gamma_r \mu_{12}^2}{4\hbar\epsilon_{avg}} \overline{N_i} \int_0^\infty \int_0^\infty g_c(\nu - \nu_c) g_h(\nu - \nu_\xi) g_i(\nu_\xi - \nu_{\xi_0})\, d\nu d\nu_\xi \tag{3.49}$$

where we have introduced a factor of 2 for averaging over dipole polarizations. For emission from a semiconductor quantum well, electron-heavy hole transitions are assumed to dominate which corresponds to restricting the dipole polarization to the plane of the quantum well. Typically in a uniform medium, it is assumed in averaging over the dipole polarizations $\langle \mu_{12,x}^2 \rangle = \langle \mu_{12,y}^2 \rangle = \langle \mu_{12,z}^2 \rangle$ so that the average over all possible orientations is $\mu_{12}^2/3$. For dipoles confined to the two-dimensional plane of the quantum well, this orientation average becomes $\langle \mu_{12,x}^2 \rangle = \langle \mu_{12,y}^2 \rangle = \mu_{12}^2/2$ and $\langle \mu_{12,z}^2 \rangle = 0$. To take this into account, we will use the notation $\bar{\mu}_{12}^2 = \mu_{12}^2/x$ where x can be either 1 or 2.

The total spontaneous emission rate given by Eq. (3.49) depends on three spectral effects: the homogeneous, inhomogeneous, and cavity lineshapes. These can be broadly characterized as being the contributions of the transition itself (homogeneous), the distribution of transitions (inhomogeneous), and a resonator Q contribution (cavity lineshape).

3.5.1 Case I: Inhomogeneous broadening dominated

Assume that the linewidths satisfy the relation:

$$\Delta\nu_h, \Delta\nu_c \ll \Delta\nu_i \tag{3.50}$$

This case is of particular interest in semiconductor materials where the inhomogeneous linewidth is due to the distribution of electron states in the bands and the Fermi distribution of electrons. At room temperature, this results in a relatively broad inhomogeneous linewidth.

Using the relation between the linewidths, the integrations in Eq. (3.49) can then be performed by approximating the homogeneous and cavity lineshape functions as delta functions.

$$\begin{aligned} R_c &\simeq \frac{\omega_c \Gamma_r \bar{\mu}_{12}^2}{2\hbar\epsilon_{avg}} \overline{N_i} \int_0^\infty g_c(\nu_\xi - \nu_c) g_i(\nu_\xi - \nu_{\xi_0})\, d\nu_\xi &(3.51)\\ &\simeq \frac{\omega_c \Gamma_r \bar{\mu}_{12}^2}{2\hbar\epsilon_{avg}} \left(\frac{\overline{N_i}}{\Delta\nu_i}\right) = \frac{e^2 \Gamma_r \bar{\mu}_{12}^2 \pi}{\hbar\epsilon_{avg}} \overline{N_i} Q_i &(3.52)\end{aligned}$$

where we have defined an effective Q for the inhomogeneous broadening $Q_i = \nu/\Delta\nu_i$. This means that if we have significant inhomogeneous broadening of the transition, there will not be any enhancement of the spontaneous emission rate regardless of the linewidth of the cavity. In fact, the relation between the homogeneous linewidth and the cavity resonance linewidth does not come into play if inhomogeneous linewidth is significantly larger.

In general, following a procedure similar to that used to derive Eq. (3.52), the lineshape function with the largest linewidth will dominate the spontaneous emission.

3.5.2 Case II: Cavity dominated

The case where the inhomogeneous linewidth is negligible can be practically important. This can occur in cases such as atomic transitions and isolated three-dimensional quantum confinement (e.g., single quantum dots or single quantum boxes). If the inhomogeneous broadening is neglected, assume that the cavity lineshape dominates over the homogeneous linewidth. In this case, the following relation holds between the linewidths:

$$\Delta\nu_i \ll \Delta\nu_h \ll \Delta\nu_c \tag{3.53}$$

Following the same argument as in the previous section, the spontaneous emission rate Eq. (3.49) reduces to

$$R_c \simeq \frac{\omega_c \Gamma_r \bar{\mu}_{12}^2}{2\hbar\epsilon_{avg}} \overline{N_i} \int_0^{\infty} g_c(\nu - \nu_c) g_h(\nu - \nu_{\xi_0})\, d\nu \simeq \frac{e^2 \Gamma_r \bar{\mu}_{12}^2 \pi}{\hbar\epsilon_{avg}} \overline{N_i} Q_c \tag{3.54}$$

This is the case of greatest practical interest because, as can be seen from Eq. (3.54), the spontaneous emission rate is now dependent on the cavity quality factor (Q) in addition to the material determined quantities. This provides an avenue for the modification of the fundamental spontaneous emission rate through cavity design.

3.5.3 Case III: Homogeneous broadening dominated

If the inhomogeneous linewidth is negligible, the homogeneous lineshape can dominate over the cavity. This case is included for completeness although it is of less practical interest than the previous two cases.

Assume that the linewidths satisfy the relation

$$\Delta\nu_i \ll \Delta\nu_c \ll \Delta\nu_h \tag{3.55}$$

In this instance, following the same procedure as before, the total spontaneous emission rate becomes

$$R_c \simeq \frac{\omega_c \Gamma_r \bar{\mu}_{12}^2}{2\hbar \epsilon_{avg}} \overline{N_i} \int_0^\infty g_c(\nu - \nu_c) g_h(\nu - \nu_{\xi_0})\, d\nu \simeq \frac{e^2 \Gamma_r \bar{\mu}_{12}^2 \pi}{\hbar \epsilon_{avg}} \overline{N_i} Q_h \tag{3.56}$$

Similar to Eq. (3.52), this spontaneous emission rate is dependent solely on material parameters. This can be used to describe the situation of atomic decay in free space. By definition, a single isolated atom undergoing a single particle transition can not have inhomogeneous broadening. Free space can be considered as a limiting case where the cavity linewidth goes to zero and the "cavity" modes become a continuum of closely spaced modes. Then, the total free space emission rate is taken as the sum of modes using Eq. (3.56), which becomes an integral over the continuum with a mode density function.

3.6 Stimulated emission and laser threshold

Following Eq. (3.49) we can write the total stimulated emission rate into a mode c with a photon number of n_c as

$$n_c R_c = \frac{\omega_c \Gamma_r \bar{\mu}_{12}^2}{2\hbar \epsilon_{avg}} n_c \overline{N_i} \int_0^\infty \int_0^\infty g_c(\nu - \nu_c) g_h(\nu - \nu_\xi) g_i(\nu_\xi - \nu_{\xi_0})\, d\nu d\nu_\xi \tag{3.57}$$

At the lasing threshold, the induced transition rate (per second) must equal the loss rate of photons from the cavity. Therefore, we can write a threshold condition

$$R_c = \frac{1}{\tau_{ph,c}} = \frac{\omega_c}{Q_c} \tag{3.58}$$

The total pumping rate is characterized by the overlap function Γ_r, which measures how well the mode overlaps the active material. Assuming that the active material spatial distribution is determined by the pump configuration, then the required pumping level to reach threshold can be characterized by the Γ_r parameter. At threshold using Eq. (3.57) and Eq. (3.58),

$$\begin{aligned} n_c\frac{\omega_c}{Q_c} &= \frac{\omega_c\Gamma_r\bar{\mu}_{12}^2}{2\hbar\epsilon_{avg}}\, n_c\overline{N_i}\int_0^\infty\int_0^\infty g_c(\nu-\nu_c)g_h(\nu-\nu_\xi)g_i(\nu_\xi-\nu_{\xi_0})\,d\nu d\nu_\xi \qquad (3.59)\\ \frac{2\hbar\epsilon_{avg}}{\bar{\mu}_{12}^2}\frac{1}{Q_c} &= \Gamma_r\overline{N_i}\int_0^\infty\int_0^\infty g_c(\nu-\nu_c)g_h(\nu-\nu_\xi)g_i(\nu_\xi-\nu_{\xi_0})\,d\nu d\nu_\xi \qquad (3.60)\end{aligned}$$

where the parameter $\Gamma_r\overline{N_i}$ characterizes the effective pumping for the mode.

3.6.1 Case I: Inhomogeneous broadening dominated

Following the method used in calculating the spontaneous emission rate, assume that

$$\Delta\nu_h, \Delta\nu_c \ll \Delta\nu_i \qquad (3.61)$$

To apply this to the spontaneous emission rate at the lasing threshold for the mode, the lineshape integrals in Eq. (3.60) can be approximated as

$$\int_0^\infty\int_0^\infty g_c(\nu-\nu_c)g_h(\nu-\nu_\xi)g_i(\nu_\xi-\nu_{\xi_0})\,d\nu d\nu_\xi \simeq \frac{1}{\Delta\nu_i} = Q_i \qquad (3.62)$$

The pumping at threshold then reduces to:

$$\Gamma_r\overline{N_i} = \left(\frac{2\hbar\epsilon_{avg}}{\bar{\mu}_{12}^2}\right)\frac{1}{Q_cQ_i} \qquad (3.63)$$

3.6.2 Case II: Cavity dominated

If the cavity linewidth is the dominating linewidth ($\Delta\nu_c$ is the largest), then the linewidths are assumed to be

$$\Delta\nu_i \ll \Delta\nu_h \ll \Delta\nu_c \qquad (3.64)$$

as was done for the same case with the spontaneous emission rate into the mode. Following the same procedure as before, from Eq. (3.60), the lineshape function integrals reduce to

$$\int_0^\infty \int_0^\infty g_c(\nu - \nu_c) g_h(\nu - \nu_\xi) g_i(\nu_\xi - \nu_{\xi_0})\, d\nu d\nu_\xi \simeq \frac{1}{\Delta\nu_c} = Q_c \qquad (3.65)$$

And the effective pumping at the lasing threshold becomes

$$\Gamma_r \overline{N_i} = \left(\frac{2\hbar\epsilon_{avg}}{\bar{\mu}_{12}^2} \right) \frac{1}{Q_c^2} \qquad (3.66)$$

3.7 Fluorescence of two modes

Consider two modes where mode 1 has a lower lasing threshold defined by Eq. (3.63) for case I ($\Delta\nu_i$ dominates). Then the effective pumping at threshold is given by Eq. (3.63):

$$\Gamma_{r,1} \left(\overline{N_i} \right)_{th} = \left(\frac{2\hbar\epsilon_{avg}}{\bar{\mu}_{12}^2} \right) \frac{1}{Q_{c1} Q_i} \qquad (3.67)$$

The effective pumping at threshold for mode 2 is given by a similar equation. From Eq. (3.67) it can be seen that the only cavity dependent part on the right hand side of Eq. (3.67) comes from the cavity Q-factor. Therefore, in assuming that mode 1 has a lower lasing threshold is equivalent to assuming that the Q of mode 1 is larger than the Q of mode 2 ($Q_1 > Q_2$).

$$\frac{\left(\overline{N_i} \right)_{th,1}}{\left(\overline{N_i} \right)_{th,2}} = \frac{\Gamma_{r,2}}{\Gamma_{r,1}} \frac{Q_{c2}}{Q_{c1}} \qquad (3.68)$$

Now, consider the spontaneous emission for the two modes. Again, assuming case I ($\Delta\nu_i$ dominates), the total rate of spontaneous emission into a mode of interest, k is given by Eq. (3.52).

$$R_k = \frac{\Gamma_{r,k}\, \bar{\mu}_{12}^2 \pi}{\hbar\epsilon_{avg}} \overline{N_i} Q_i \qquad (3.69)$$

So, the total spontaneous emission into mode 1 near the lasing threshold defined by Eq. (3.67) is

$$\begin{aligned} R_1 &= \frac{\bar{\mu}_{12}^2 \pi Q_i}{\hbar \epsilon_{avg}} \Gamma_{r,1} \left(\overline{N_i}\right)_{th} && (3.70) \\ &= \frac{\bar{\mu}_{12}^2 \pi Q_i}{\hbar \epsilon_{avg}} \left(\frac{2\hbar \epsilon_{avg}}{\bar{\mu}_{12}^2}\right) \frac{1}{Q_{c1} Q_i} && (3.71) \\ &= \frac{2\pi}{Q_{c1}} && (3.72) \end{aligned}$$

The spontaneous emission into mode 2 at the same pumping level can be similarly derived to be

$$R_2 = \frac{2\pi}{Q_{c1}} \frac{\Gamma_{r,2}}{\Gamma_{r,1}} \tag{3.73}$$

The ratio of spontaneous emission into these two modes of interest can be determined at the lasing threshold for mode 1.

$$\frac{\text{Emission into mode 1}}{\text{Emission into mode 2}} = \frac{R_1}{R_2} = \frac{\Gamma_{r,1}}{\Gamma_{r,2}} \tag{3.74}$$

This means that the spontaneous emission into each modes depends only on the relative filling factors between the modes. In other words, for equal total pumping, the mode that has the greatest overlap with the pumping region emits the most.

Assume now that $(\Gamma_{r,1}/\Gamma_{r,2}) < 1$, which means that the overlap between the pump and mode 2 is greater than that with mode 1. In this case, Eq. (3.74) indicates that the spontaneous emission into mode 2 will dominate. However, consider the relative excited atomic density at threshold given by Eq. (3.68). Mode 1 can reach threshold before mode 2 (even though there is more emission into mode 2), provided that

$$\frac{\left(\overline{N_i}\right)_{th,1}}{\left(\overline{N_i}\right)_{th,2}} < 1 \tag{3.75}$$

Using Eq. (3.68) and the assumed relation between the Q of the modes, this can be rewritten as the following condition:

$$\frac{Q_{c1}}{Q_{c2}} > \frac{\Gamma_{r,2}}{\Gamma_{r,1}} > 1 \tag{3.76}$$

3.8 Purcell enhancement factor

To consider only the cavity contribution to the spontaneous emission rate, we begin with the previously derived homogeneously dominated case for the spontaneous emission rate Eq. (3.54).

$$R_c \simeq \frac{\omega_c \Gamma_r \bar{\mu}_{12}^2}{2\hbar\epsilon_{avg}} \overline{N_i} \int_0^\infty g_c(\nu - \nu_c) g_h(\nu - \nu_{\xi_0})\, d\nu \simeq \frac{\Gamma_r \bar{\mu}_{12}^2 \pi}{\hbar\epsilon_{avg}} \overline{N_i} Q_{mat} \tag{3.77}$$

where we have used Q_{mat} for the material Q which in fact, may be homogeneous or inhomogeneous since both results have the same form. For a single particle transition, $N_i = 1$.

The regular unenhanced spontaneous emission rate is given by [75]

$$R_{free} = \frac{n^3 \mu_{12}^2 \omega^3}{3\pi\hbar c^3 \epsilon} \tag{3.78}$$

The Purcell enhancement factor is given by the ratio of the enhanced cavity emission to the free-space emission rate.

$$\frac{R_{cav}}{R_{free}} = \frac{3Q_{mat}\Gamma_r}{\pi} \frac{\bar{\mu}_{12}^2}{\mu_{12}^2} \frac{\epsilon}{\epsilon_{avg}} \left(\frac{\lambda}{2n}\right)^3 \tag{3.79}$$

From the definitions of Γ_r and ϵ_{avg} we can define an effective volume, since Γ_r has units of inverse volume. Also taking the quantum well case where $\bar{\mu}_{12}^2 = \mu_{12}^2/2$, this can be recast as the Purcell enhancement factor F

$$F = \frac{3Q_{mat}}{2\pi V_{eff}} \left(\frac{\lambda}{2n}\right)^3 \tag{3.80}$$

This expression differs slightly from that derived originally by Purcell [14] by a factor of $\pi/4$ which follows simply from the lineshape approximation and the polarization averaging of the dipole.

3.8.1 Purcell enhancement into band states

All the previous discussions in this chapter have dealt with emission into individual optical modes. However, consider the analogy with solid state physics and photonic crystals. In a periodic array of atoms, the individual atomic states interact and combine to form closely spaced states which become a near continuum for large numbers of atoms. Analogously, a period array of dielectric structures can combine to form continuous bands of states from the individual discrete states of the isolated dielectric structures (the dielectric 'atoms'). Spontaneous emission in this situation may be modified from the free-space solution in a similar manner as the modification of the emission rate in a microcavity. The band states can have a strongly modified spatial distribution since they have as their basis the localized states of the dielectric 'atoms.'

Since we wish to consider a continuous distribution of optical states within a so called *photonic band*, it will be assumed that the spectral width of the band is large compared to the homogeneous linewidth of the emitting species. The band width may also be large compared to the inhomogeneous linewidth however, this restriction will not be used at this point.

Begin by considering the previously derived spontaneous emission rate into a mode c given by Eq. (3.49).

$$R_c = \frac{\Gamma_r \bar{\mu}_{12}^2}{2\hbar\epsilon_{avg}} \overline{N_i} \int_0^\infty \int_0^\infty \omega_c g_c(\nu-\nu_c) g_h(\nu-\nu_\xi) g_i(\nu_\xi-\nu_{\xi_0})\, d\nu d\nu_\xi \tag{3.81}$$

In this case, the lineshape function for the cavity is replaced by a density of optical states $\rho(\nu)$. This can be easily seen by considering the sum over the spontaneous emission into all the modes $R = \sum_c R_c$ and then taking the limit for a near continuum of modes $\sum_c \rightarrow \int d\nu$. Assume that the homogeneous linewidth is narrow such that the spontaneous emission rate becomes

$$R_{band} = \int_0^\infty \frac{\omega\Gamma_r\bar{\mu}_{12}^2}{2\hbar\epsilon_{avg}} \overline{N}_i \rho(\nu) g_i(\nu - \nu_{\xi_0})\, d\nu \tag{3.82}$$

To see the effects of the optical band independent of the transition details, take the inhomogeneous linewidth to be narrow and the average excited state density $N_i = 1$. Then the spontaneous emission rate spectrum can be written as

$$R_{band}(\nu) = \frac{\omega\Gamma_r\bar{\mu}_{12}^2}{2\hbar\epsilon_{avg}} \rho(\nu) \tag{3.83}$$

It is clear that in comparison with the uniform space emission rate from Eq. (3.78), the equivalent band-enhanced Purcell factor is now

$$\begin{aligned} F_{band} &= \frac{3\pi\hbar c^3\epsilon}{n^3\mu_{12}^2\omega^3} \cdot \frac{\omega_c\Gamma_r\bar{\mu}_{12}^2}{2\hbar\epsilon_{avg}} \rho(\nu) & (3.84) \\ &= \frac{3\nu}{16\pi V_{eff}} \left(\frac{\lambda}{2n}\right)^3 \rho(\nu) & (3.85) \end{aligned}$$

Micro- or nano-cavities are not necessary to achieve modified spontaneous emission behavior. The idea introduced by Purcell of modified spontaneous emission in a resonator can be extended to consider these photonic bands. Clearly, within a photonic band gap the spontaneous emission could be strongly suppressed since, by definition, the band gap is a spectral region with a density of states $\rho(\nu) \rightarrow 0$. This was predicted by Yablonovitch in 1987 [7]. This band-enhanced Purcell factor also shows that enhanced spontaneous emission can occur at points of high density of states. The difference between this viewpoint and section 3.8 is in some sense merely a conceptual one, since the cavity mode lineshape peaks can also be considered as enhancements in the density of states. However, these two cases do differ in that the cavity modes are spatially localized to the cavity whereas the band states are distributed modes. In addition to the density of states dependence, Eq. (3.85) also includes a $1/V_{eff}$ dependence, which describes an enhancement to the spontaneous emission rate due to the spatial mode distribution. The Purcell enhancement can therefore be conceptually divided into a spectral ($\rho(\nu)$), related to the local electromagnetic density of states, and a spatial ($1/V_{\mathit{eff}}$) part. This will be discussed through numerical simulations in chapter 6.

Chapter 4 Photonic crystals for microcavity emitters

4.1 Introduction

High Q optical cavities are considered to be useful for high efficiency, low power light sources. Photonic crystal based structures have been suggested as a means towards such devices [11]. One-dimensional photonic structures have been used successfully in light emitting diodes (LED) to enhance efficiency and spontaneous emission [76]. Recently, two-dimensional structures have attracted a great deal of attention [77, 78, 79] due to the simpler geometry, in terms of both fabrication complexity and device design as compared to three-dimensional structures. Such structures have been considered as a means of controlling in-plane spontaneous emission, a significant loss mechanism in vertical-emitting structures [77]. However, experimental evidence [78, 80] has indicated that finite hole depth and waveguide geometry can lead to strong scattering of light into the substrate, which would limit the confinement possible with a 2D photonic crystal due to scattering out of the photonic crystal plane. One solution to this is the use of high index contrast cladding layers above and below the photonic crystal plane [81]. Scattering out of the photonic crystal plane can also be limited by extending the two-dimensional photonic crystal structure well into a lower index cladding layer [48, 64, 81].

Passive reflection, diffraction, and transmission measurements have recently been carried out in two-dimensional photonic crystal structures [82]. Berggren et al. [83] have also made active devices by including a low index contrast two-dimensional periodicity that did not have a complete bandgap. Borodistky et al. [84] have demonstrated photonic crystal microcavities where the photonic structure is used for output coupling in thin slab structures. Slab confined modes are scattered into free space

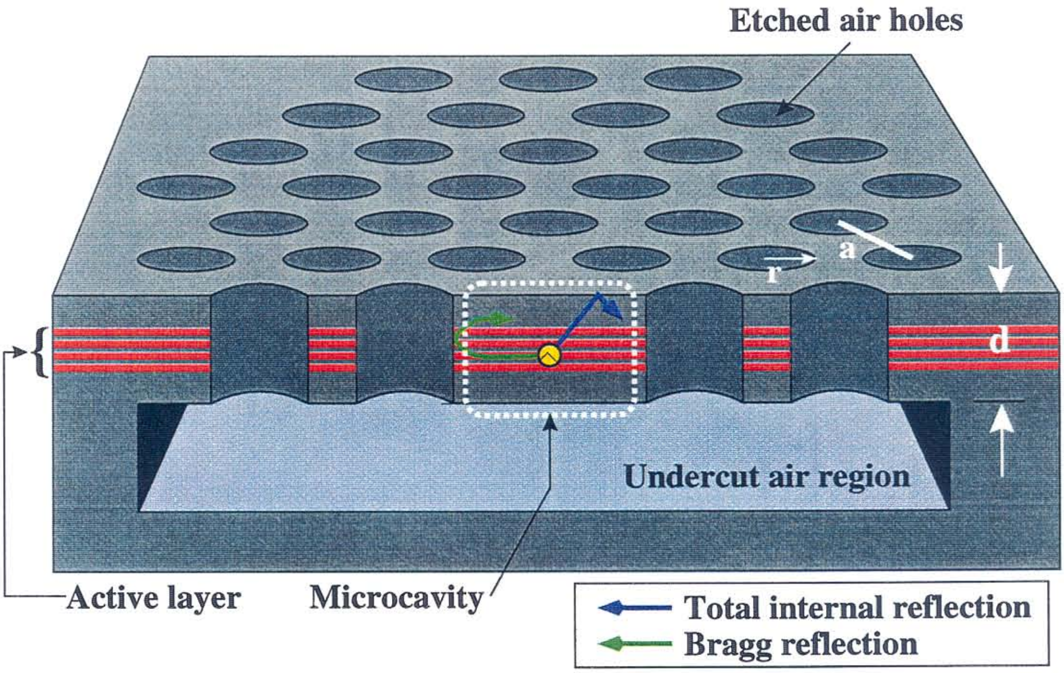

Figure 4.1: Schematic diagram of 2D triangular photonic bandgap structure. Light is confined in the slab plane by reflection from the photonic crystal and out of the plane by total internal reflection at the air interface. The slab thickness $d \approx \lambda/2n$.

radiation modes with a net external efficiency estimated at $\sim 70\%$.

Using the high index contrast between semiconductor and air for vertical confinement, two-dimensional photonic crystals can be successfully used to create well confined optical microcavity thin film-like structures [65, 66, 85]. In this chapter, the fabrication of such photonic crystal defined thin-film optical microcavities is discussed in section 4.2 and has been discussed in [85]. Spontaneous emission characteristics of hexagonally shaped microcavities [65] are presented in section 4.3. Room temperature pulsed lasing [66] under optical pumping is discussed in section 4.4 with respect to the predicted modal behaviour described in section 3.7.

4.2 Microcavity design and fabrication

A schematic of the photonic crystal based microcavity is shown in Fig. 4.1. Photons generated within the d $\approx \lambda/2$n high-index semiconductor slab are confined in the vertical direction by total internal reflection at the semiconductor-air interface.

The photonic crystal lattice then confines the light in the slab plane through Bragg scattering, which gives rise to an in-plane band gap. The slab membrane consists of 6 unstrained InGaAs quantum wells as an active layer with InGaAsP barriers grown by metalorganic chemical vapor deposition (MOCVD) on an InP substrate with a total waveguide thickness of 150 nm. The material epitaxial structure is shown in Table 4.1. The InGaAsP system was chosen for its relatively low surface recombination velocity [86] because of the high surface to volume ratio of these microcavities. The photonic crystal structure requires etching of holes through the slab membrane with a relatively high porosity resulting in a large free surface area with corresponding surface recombination. In most semiconductors, the ambipolar carrier diffusion length is on the order of microns that, for microcavities in the micron size scale, the surface of the cavity are within one or several diffusion lengths of all points in the cavity. Therefore, surface recombination can be a significant concern in active semiconductor microcavities. For the slab membrane structure, the surfaces in the z-direction (see Fig. 4.1) are not a significant concern because of the vertical confinement provided by the epitaxial quantum wells.

The quantum well emission was designed to be centered around a wavelength of 1.55 μm ($\sim$0.8 eV) with a barrier band gap energy of 1.1 eV corresponding with a wavelength of approximately 1.1 μm. The fabrication process for the membrane structure is shown in Fig. 4.2. The two-dimensional triangular photonic lattice is patterned using direct write electron-beam lithography into a poly-methylmethacrylate (PMMA) electron beam resist. The triangular lattice of air holes was chosen because it results in a relatively large in-plane bandgap [44] for electromagnetic modes with the electric field transverse (TE) to the slab (magnetic field $\vec{H}$ normal to the slab plane). The unstrained quantum wells emit primarily into TE modes since the electric dipole can be consider to be confined to the quantum well plane. The pattern in the PMMA resist is transferred into a multi-level intermediate mask layer composed of a thermally evaporated thin gold layer on top of a Si_3N_4 or SiO_2 layer by argon ion milling (for the Au layer) and reactive ion etching (for the silicon containing layer). The multiple mask layers are necessary because the InGaAsP etching is performed

150 nm	200 Å InGaAsP end cap	
	100 Å $In_{0.53}Ga_{0.47}As$ QW	
	100 Å InGaAsP barrier	
	100 Å $In_{0.53}Ga_{0.47}As$ QW	
	100 Å InGaAsP barrier	
	100 Å $In_{0.53}Ga_{0.47}As$ QW	
	100 Å InGaAsP barrier	
	100 Å $In_{0.53}Ga_{0.47}As$ QW	
	100 Å InGaAsP barrier	
	100 Å $In_{0.53}Ga_{0.47}As$ QW	
	100 Å InGaAsP barrier	(Eg=1.1 μm)
	100 Å $In_{0.53}Ga_{0.47}As$ QW	(Eg=1.72 μm)
	200 Å InGaAsP end cap	(Eg=1.1 μm)
	InP substrate	

Table 4.1: Undoped InGaAsP epitaxy for air suspended slab photonic crystal structures grown by Ortel Corporation. All layers are lattice matched to the InP substrate

at an elevated temperature, which is incompatible with the PMMA resist. The InGaAsP waveguide layer is then patterned using a Cl_2 chemically assisted ion-beam etch (CAIBE). The patterned waveguide layer is then separated from the substrate to leave a free standing membrane by using a selective wet etch solution (4:1 $HCl:H_20$) which removes the InP below the waveguide layer. This final wet etch is performed at low temperature ($T \sim 1^\circ C$) to reduce the etching speed to avoid the collapse of the membrane structure.

An oblique view scanning electron micrograph of a typical structure is shown in Fig. 4.3, which shows a hexagonal shaped microcavity surrounded by the triangular lattice photonic crystal. Clearly, other microcavity geometries are possible limited only by the discrete triangular lattice hole spacing. The smallest such cavity, formed by the removal of only a single hole will be referred to as a "defect" cavity and will be discussed in greater detail in chapter 5. Fig. 4.4 shows an oblique view of a cross-section through a typical patterned membrane structure showing the suspended structure. In this case an etch stop quaternary InGaAsP layer was included to stop

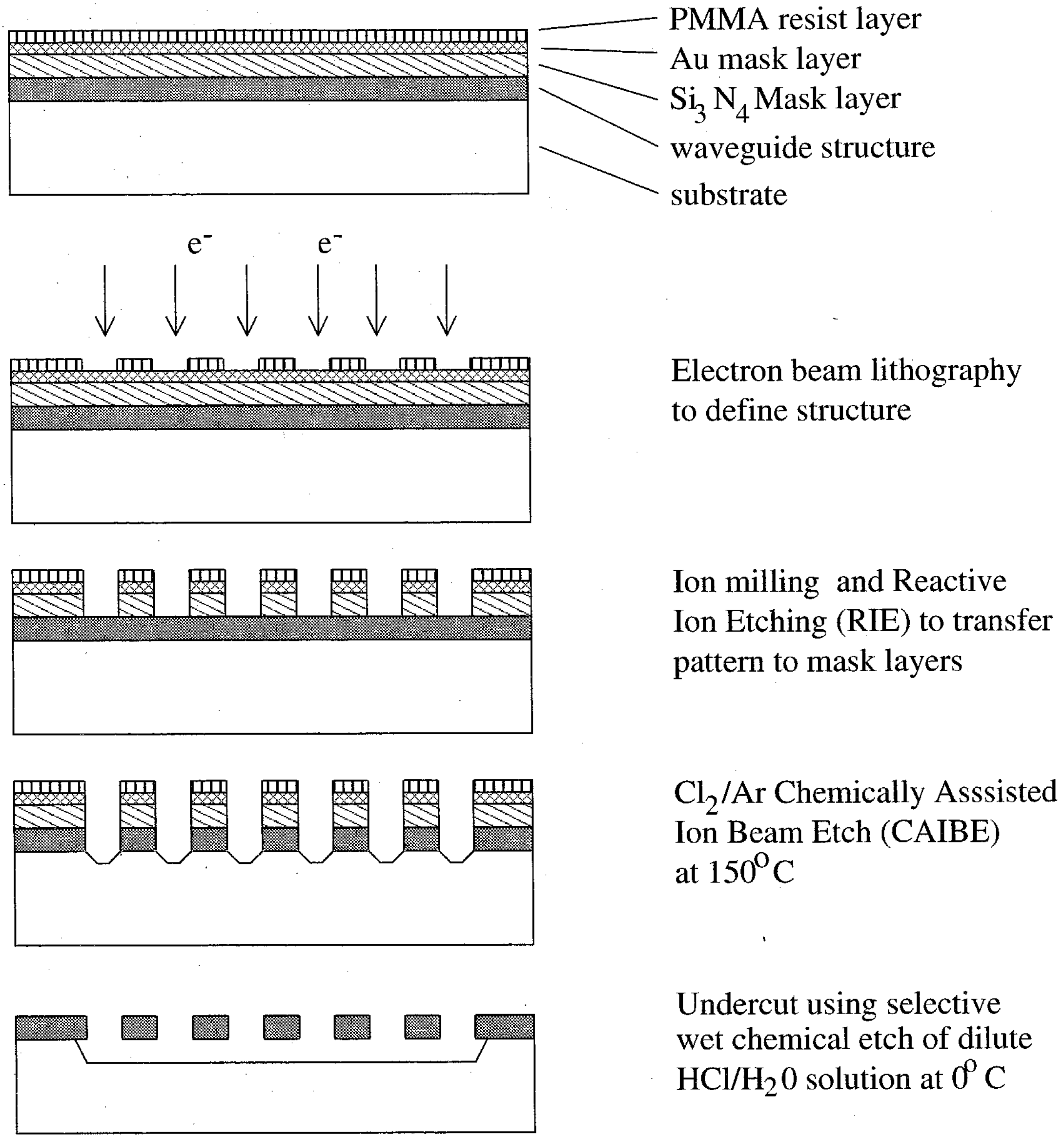

Figure 4.2: Process flow for fabrication of free standing membrane photonic crystal structures.

the under-cutting wet selective etch leaving a smooth bottom surface.

A typical in-plane band structure plot for this photonic lattice patterned into a thin slab calculated using the effective two-dimensional plane wave expansion described in section 2.1 and an effective index of $n_{eff} \approx 2.65$ is shown in Fig. 4.5. A band gap for TE modes is evident in the frequency range $a/\lambda = 0.29$ to 0.40 with no band gap for TM modes [27, 77, 87]. This can be compared with the bandstructure calculated using a three-dimensional finite difference time-domain (FDTD) technique, is shown on the left in Fig. 4.6. The trapezoidal upper boundary in the plot represents the light line and only confined modes below the light line have been shown. The two-dimensional approximation and the fully three dimensional band structures are similar showing bands with qualitatively the same shape and position. There is a significant difference in the precise bandgap position and width by approximately 20%. However, the similarities allow the use of the speed and efficiency of the two-dimensional approximation to be used as a first approximation design tool. It has been previously shown [27] that the finite extent of the photonic crystal in the vertical direction modifies the bandgap location and width as compared to an infinite two-dimensional approximation. Therefore, a full three dimensional bandstructure calculation is necessary for accurate design and comparison with experimental results. Fig. 4.6 was calculated for a structure with the ratio of the hole radius to the lattice parameter, $r/a = 0.35$ and the ratio of the waveguide thickness to lattice parameter, $d/a = 0.33$. This results in an in-plane bandgap in normalized frequency units between 0.348 and 0.465.

4.3 Hexagonal cavity spontaneous emission

We have designed and fabricated two-dimensional photonic crystals in a thin semiconductor membrane bounded above and below by air. The optical cavity consists of an approximately $\lambda/2n$ thick dielectric slab waveguide suspended in air. The membrane is patterned with a triangular two-dimensional array of air holes. A number of holes can be omitted to form hexagonally shaped cavities, providing in-plane localization as

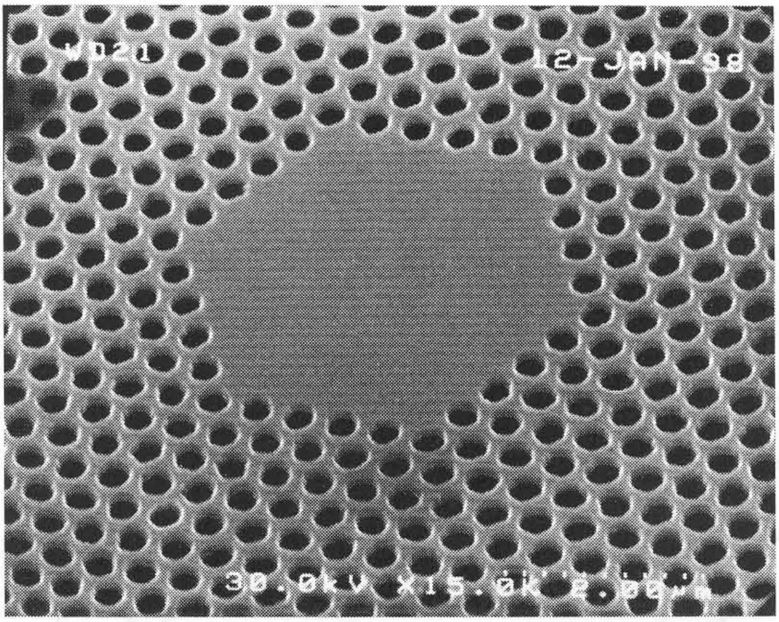

Figure 4.3: Oblique angle SEM image of typical two-dimensional photonic crystal cavity fabricated in an InGaAsP semiconductor slab. Each face of the microcavity is $\sim 2.2\ \mu$m.

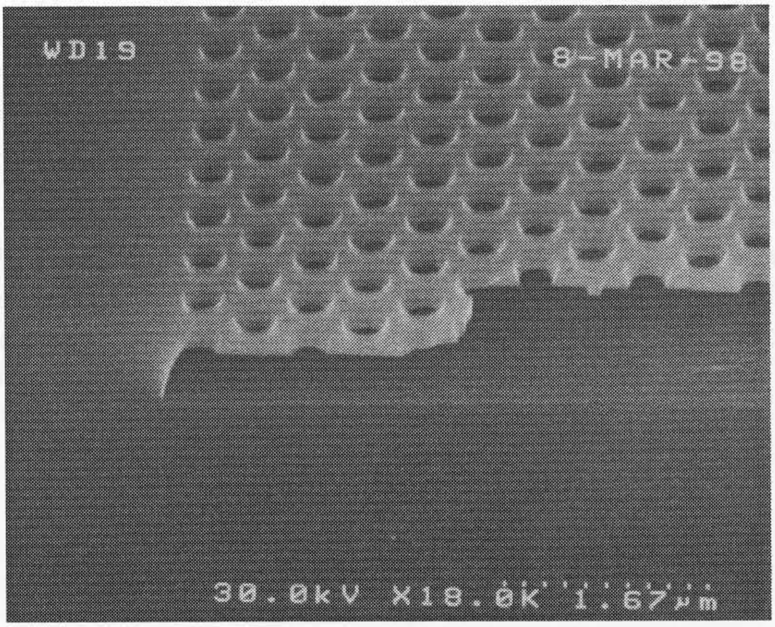

Figure 4.4: Cross-section through the patterned membrane structure. The InGaAsP slab in the measured devices is approximately 150 nm thick and the air gap underneath membrane can be seen.

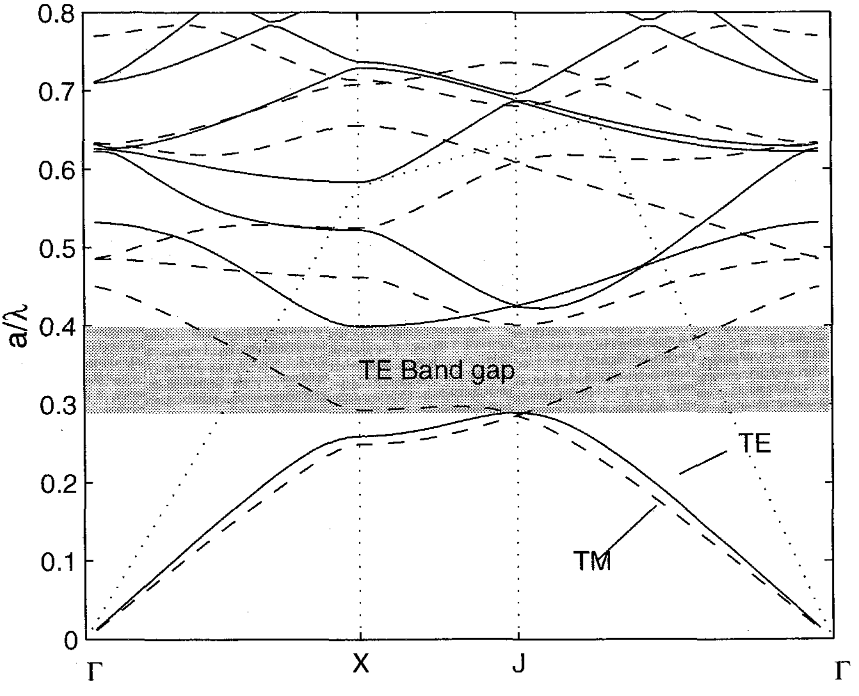

Figure 4.5: Bandstructure for triangular lattice of air holes using a two-dimensional effective index plane wave expansion method calculation using an effective index of $n_{eff} = 2.65$ and 441 plane waves. The dotted line trapezoid is the light line and the solid and dashed lines are the TE and TM modes respectively. The TE bandgap is from 0.29 to 0.40.

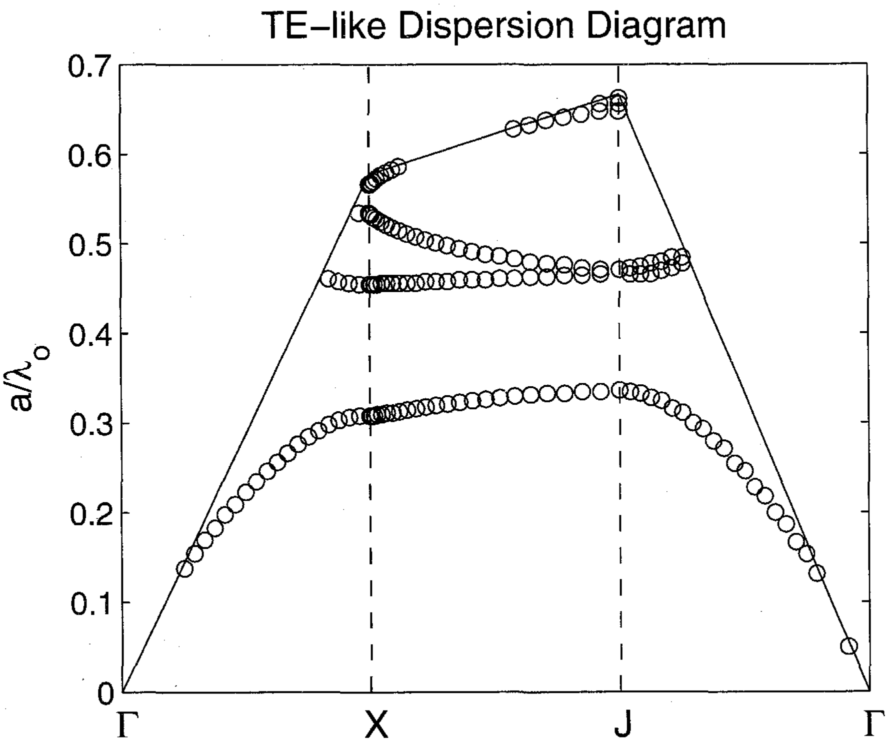

Figure 4.6: Full three-dimensional FDTD bandstructure showing only the slab confined modes below the light line for $d/a \approx 0.33$ and $r/a = 0.35$.

shown in Fig. 4.3 and Fig. 4.7. The cavities were designed with the photonic bandgap centered around the peak emission wavelength at a normalized frequency of approximately a/$\lambda = 0.32$ (lattice spacing of a = 500 nm for $\lambda = 1550$ nm). This normalized frequency is close to the bandgap center of a/$\lambda \approx 0.35$ from the two-dimensional approximate band structure in Fig. 4.5. Subsequent calculations with the full three-dimensional band structure in Fig. 4.6 have shown that this design parameter, may lie slightly below the lower band edge. The results in the following sections refer to cavities that have sides of the hexagonal cavity, 11 photonic lattice periods in length, which results is a cavity (at a = 500 nm) approximately 9.5 μm across (face to face, vertex to vertex is 11 μm). Because of the large size of the cavity compared to the wavelength ($\lambda/n \approx 456$ nm) this cavity would be expected to support a relatively large number of modes. The number of modes can be roughly estimated since for a two-dimensional rectangular cavity, the number of modes per unit area per unit frequency interval is [88]

$$g_\nu = \frac{8\pi\nu}{c^2} \tag{4.1}$$

So for the above 9.5 μm hexagon (with area of 78.6 μm^2), at a wavelength of 1.55 μm that corresponds to a bandgap of $\Delta\nu \approx 69$ THz for a gap from 0.348 to 0.465, this sets the approximate number of confined modes at 293 within the bandgap bandwidth $\Delta\nu$. A scanning electron micrograph of an 11-period per face device is shown in Fig. 4.7. A variety of devices were fabricated with lattice spacings from 300 nm to 1 μm while maintaining $r/a \approx 0.32$, thereby lithographically tuning the bandgap [89] across the emission spectrum. These devices are similar to microdisk lasers [16] but bounded by PBG material so that the total internal reflection of the microdisk is replaced by Bragg reflection from the photonic crystal. A finite difference time domain calculation [27] of the resonant mode in this structure (Fig. 4.8) is reminiscent of a microdisk whispering gallery mode even though the cavity is hexagonal rather than circular. Other types of modes also exist in this structure in addition to the whispering gallery-like modes. These are primarily modes that reflect between opposing faces of the hexagon. In these devices, it is possible to design the cavity modes by engineering the photonic band gap energy and by controlling the cavity shape.

The membrane microcavity was optically pumped by 200 nsec pulses from a semiconductor laser (Ortel 1911A-050 $\lambda = 980$ nm) as shown in Fig. 4.10 and focused to a spot size of approximately 8 μm. Photoluminescence from the quantum wells at $\lambda \simeq 1.55$ μm was collected normal to the membrane (Fig. 4.11). Fig. 4.12 shows the spectrum from unpatterned material and from a cavity showing strong resonances superimposed on the broader quantum well emission. The emission peak from the hexagonal cavity has been red shifted approximately 70nm as well as noticeably broadened due to heating of the membrane by the pump light, corresponding to a membrane temperature of approximately 375 K [90]. This heating is a result of the high peak pumping density ($\sim$ 10 kW/cm^2) as well as the poor thermal conduction. With the membrane thickness being only 150 nm and being air suspended, there is a relatively narrow thermal conduction path to remove heat from the membrane. Although there will also be some conduction as well as convection in the air surrounding the membrane, this has been seen to be insignificant by comparing these measurements with similar measurement made by placing the devices in a chamber evacuated to approximately 5×10^{-5} torr. All devices were fabricated in close proximity on the same wafer in order to minimize temperature variations between the measurements. The emission peak red shift was used to estimate the active layer temperature. Negligible differences were observed between devices at a given pumping level. This is an important consideration since heating can account for significant shift in the refractive index as well as change the internal quantum efficiency of the active layer material. The peak emission power from the hexagonal cavity has been enhanced by approximately 2.0× as compared to the unpatterned material as shown in Fig. 4.12. This enhancement is largely due to the fact that these structures are undercut leaving an air gap beneath the membrane. This agrees quite well with a predicted normal direction emission power enhancement of 1.81× for dipole emission in this slab waveguide structure suspended in air as compared to the same waveguide on an InP substrate even though this measurement only gives the enhancement

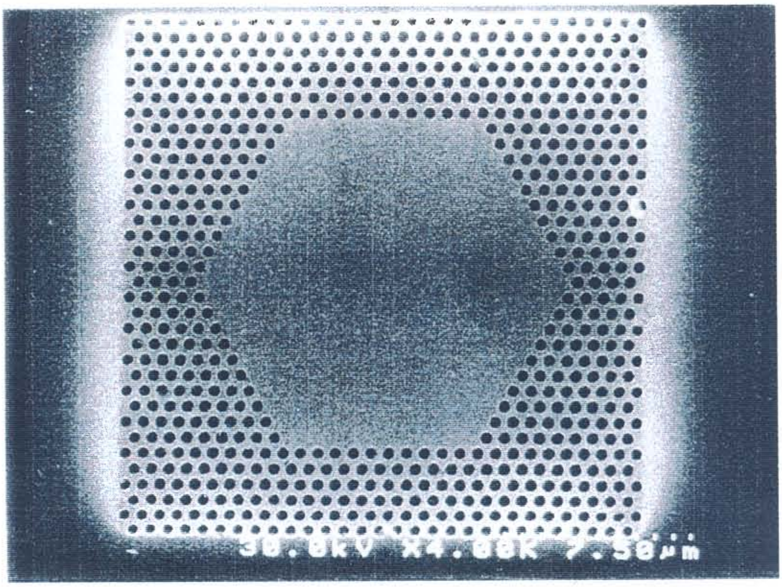

Figure 4.7: Scanning electron micrograph (top view) of a hexagonal membrane cavity bounded by 2D photonic bandgap crystal.

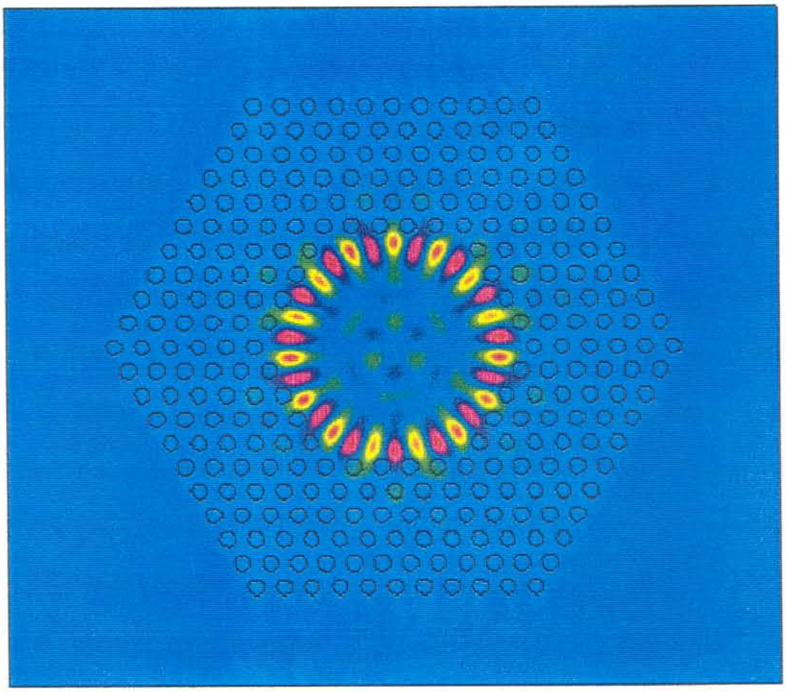

Figure 4.8: Calculated field distribution for a possible whispering gallery-like mode in a hexagonal photonic crystal cavity similar to that shown in Fig. 4.7.

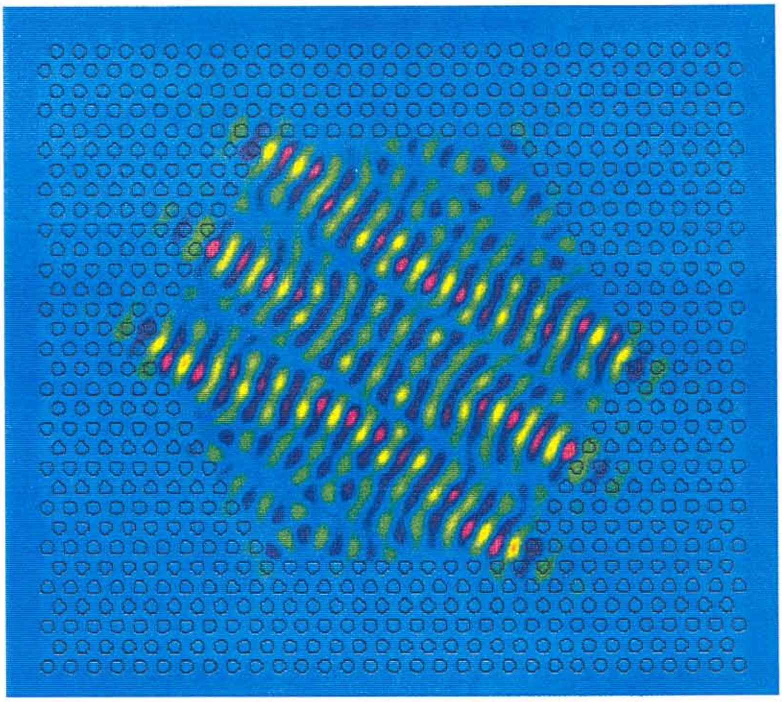

Figure 4.9: Calculated electric field amplitude distribution for a cavity mode that appears to reflect between opposing faces of the hexagon.

into the collection cone defined by the optics (numerical aperture NA = 0.6). This spontaneous emission enhancement calculation has been described in [20] and in [91].

The emission spectra from various hexagonal membrane cavities is shown in Fig. 4.14. Fig. 4.14a corresponds to a relatively large lattice spacing of a = 760 nm and is very similar to measured emission from unpatterned material. The peak in the spectrum at approximately $\lambda = 1440$ nm is due to the n=2 transition in the quantum well (second quantized state). The n=1 transition appears as the shoulder/peak in the emission at approximately $\lambda = 1570$ nm. Cavity resonances can be seen in Fig. 4.14b at a lattice spacing a $\approx$ 682 nm and at a $\approx$ 617 nm (Fig. 4.14c). For larger lattice spacings (Fig. 4.14a, a $\approx$ 760 nm) no cavity resonances are evident. For shorter lattice spacings the resonances are barely visible at a $\approx$ 563 nm (Fig. 4.14d) and then disappear for subsequent lattice sizes (Fig. 4.14e-g). This result is consistent with a cavity resonance reflecting from the photonic band gap crystal. If the reflection were a simple Fresnel reflection from the air interface or an effective index-type Fresnel reflection, the cavity resonance spacing would be seen to tune only with the cavity

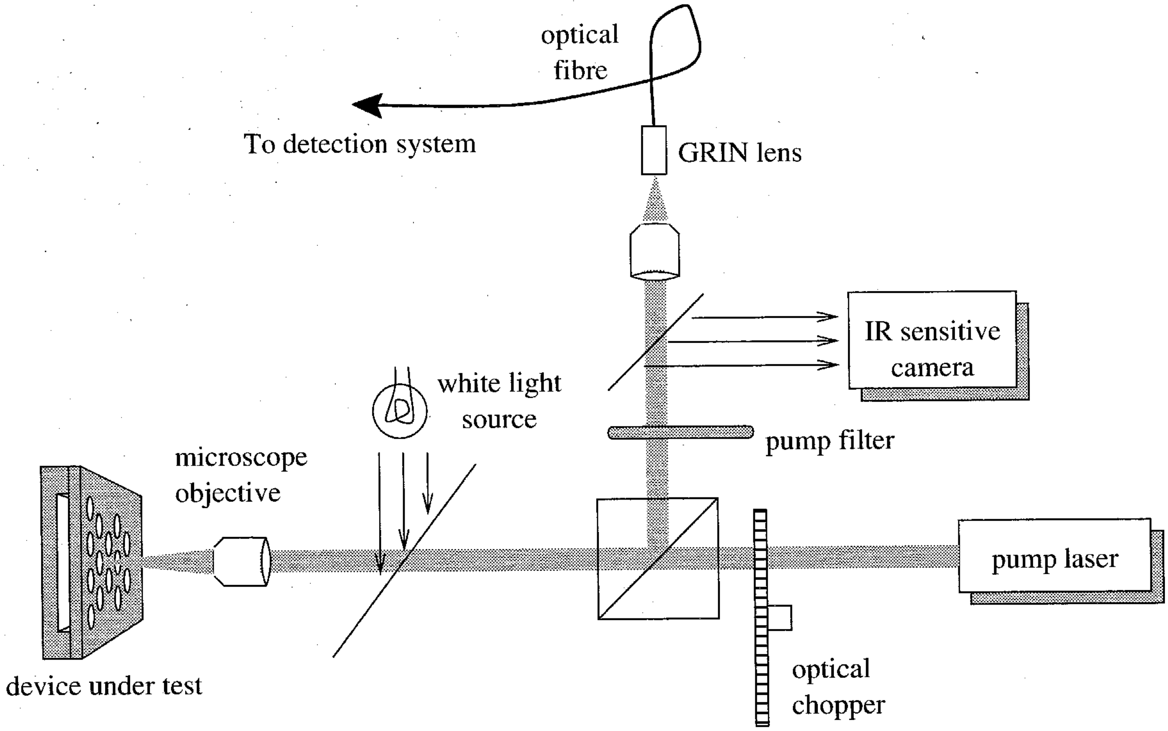

Figure 4.10: Micro-photoluminescence pumping setup.

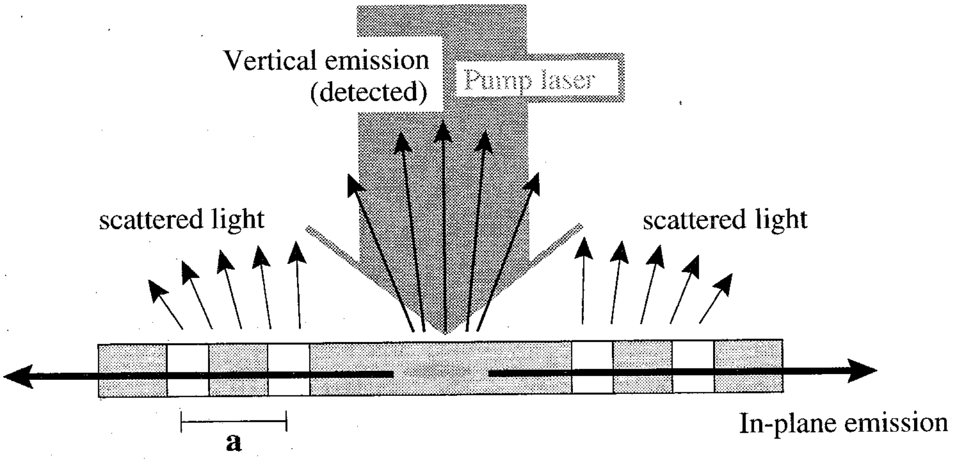

Figure 4.11: Power extraction and pumping geometry from photonic crystal thin-film devices.

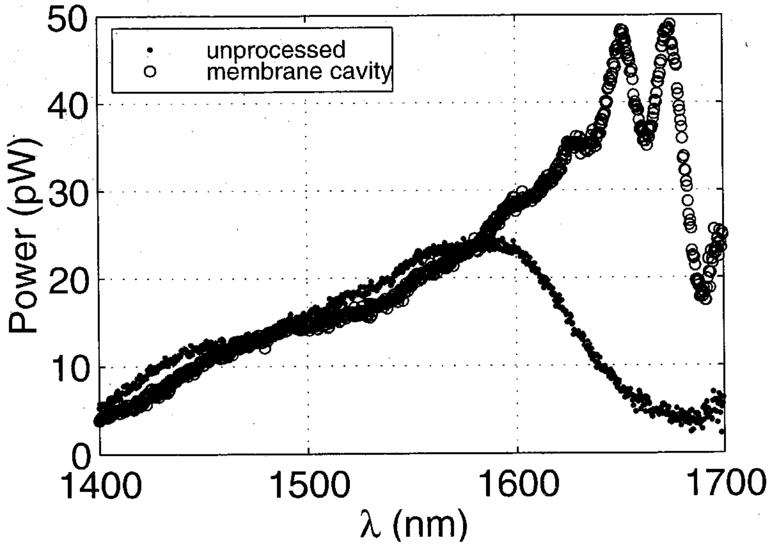

Figure 4.12: Spectrum showing enhanced emission from hexagonal membrane cavity measured with a 10 nm bandwidth. Peak power from the membrane device shows a 2.0× enhancement.

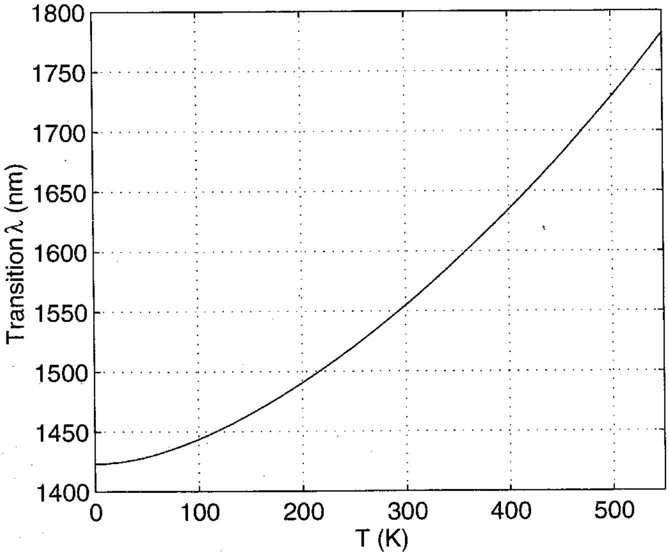

Figure 4.13: Temperature dependence of the transition wavelength for lattice matched $In_{0.53}Ga_{0.47}As$ on InP including estimated shift due to carrier confinement in the quantum wells after Landolt [90].

size (proportional to a) and resonances would be expected for all lattice sizes.

The cavity resonances in Fig. 4.14b (a $\approx$ 682 nm) appear with a spacing of $\Delta\lambda \approx$ 26.4 nm. Using a simple Fabry-Pérot approximation and a material index of n=3.4, this gives an effective cavity length of d=15.4 μm. This corresponds well with the hexagon size (vertex-to-vertex) measured by scanning electron micrograph (Fig. 4.7) of approximately 15 μm. This suggests that the spontaneous emission peaks in Fig. 4.12 and Fig. 4.14 may be associated with Fabry-Pérot-like modes that cross the hexagon as opposed to whispering gallery-like modes such as shown in Fig. 4.8. This is not surprising since the pump beam has a Gaussian profile centered near the center of the hexagon. As shown in section 3.7, Eq. (3.74), the relative spontaneous emission into various modes is proportional to the overlap between the mode and the pumping profile. For the devices with strong cavity resonances, the normalized emitted power can also be seen to be larger than for detuned bandgaps (e.g. Fig. 4.14a and c). The cavity resonances in Fig. 4.14 are seen to be strongest near a hole spacing of a = 682 nm as compared to the calculated bandgap center for this structure for a whole spacing of 500 nm as mentioned previously. However, due to strong heating in the device, the emission peak was red shifted significantly as compared to the original 1550 nm emission wavelength. Also because of the dramatic temperature change the material index and structure size (due to thermal expansion) are also slightly shifted, which could account for the difference between the calculated design and the measured resonances.

Fig. 4.15a-d show variations in the cavity resonances as the photonic crystal hole size is increased with a constant lattice spacing, thereby varying r/a around the design value $r/a = 0.31$. Fig. 4.15c corresponds to the same device as shown in Fig. 4.14b. As the value of r/a is increased, a shift of the bandgap towards higher frequencies (shorter wavelength) is expected [44]. This shift can be seen in Fig. 4.15 where the peak at $\lambda \approx$ 1650 nm in Fig. 4.15a gradually shifts to a shorter wavelength of $\lambda \approx$ 1635 nm in Fig. 4.15d. However, Fig. 4.15 shows that the strongest peak appears to jump to a longer wavelength from Fig. 4.15b to Fig. 4.15c. These are difficult to interpret because of the strong heating effects and the discrete number of r/a values.

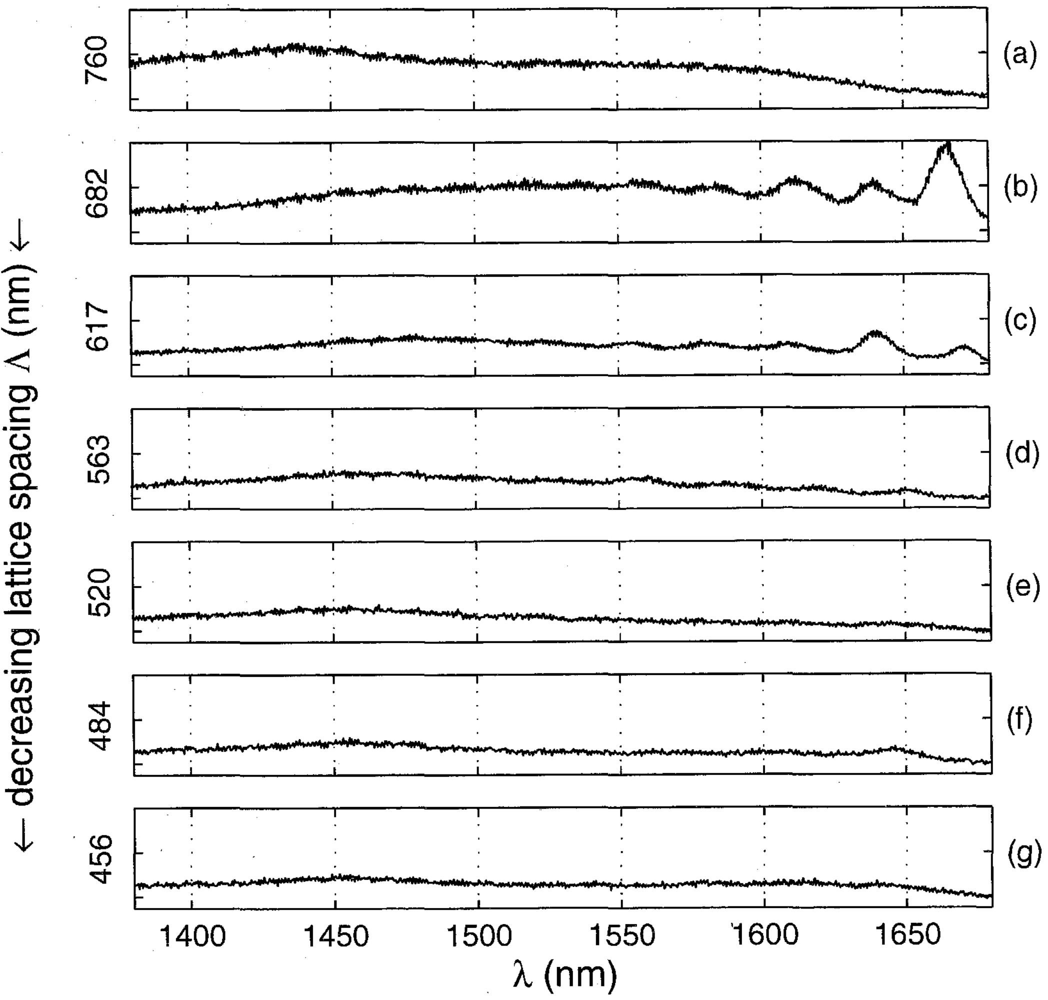

Figure 4.14: Vertical spontaneous emission spectra from hexagonal membrane cavities. The lattice parameter for each spectrum is shown (in nm) to the left of each curve decreasing from (a) to (g). The resonances only appear for lattice parameters where the emission is tuned to the photonic bandgap.

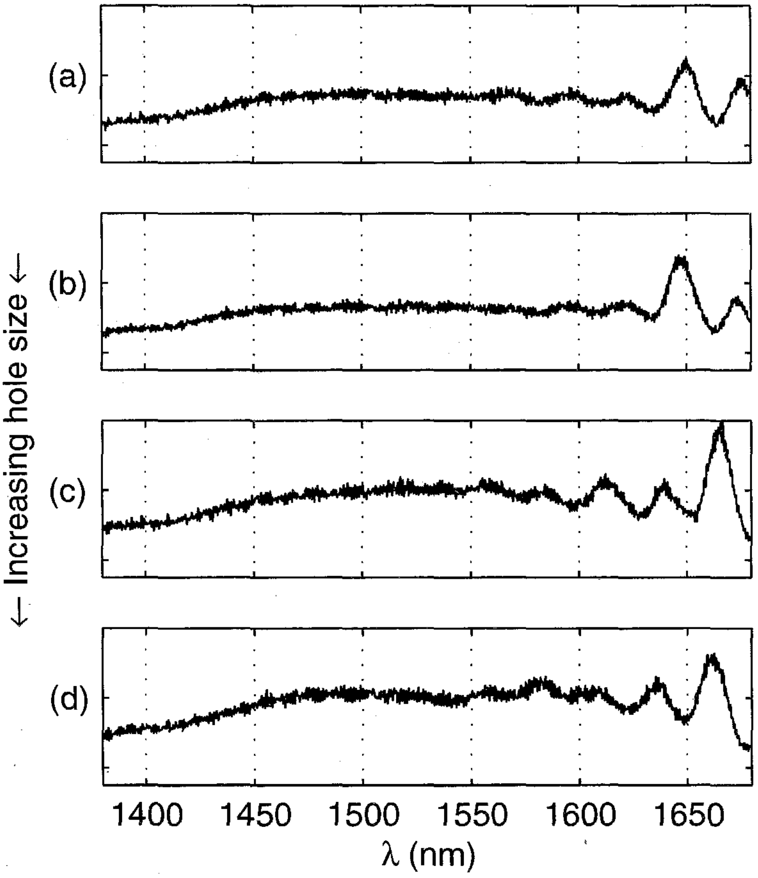

Figure 4.15: Spectra for cavities with the same nominal lattice spacing but varying the hole radius r/a. These devices correspond to a $\approx$ 682 nm showing the strongest resonances in Fig. 4.14. (c) corresponds to Fig. 4.14b.

4.4 The hexagonal disk laser

Since their introduction in 1992 [17], microdisk lasers have attracted significant attention as high-Q light sources with very strong optical confinement and small modal sizes. Their lasing modes approximate whispering gallery modes, which depend on total internal reflection at the curved boundary of the semiconductor disk. This concept can be extended to a photonic bandgap confined structure to create a qualitatively similar whispering gallery-like mode as shown in Fig. 4.8. One advantage in the use of a photonic bandgap structure lies in the ability to arbitrarily reduce the cavity size subject to the photonic lattice translation symmetry. For modes confined by total internal reflection, the radiation loss scales approximately as the inverse of the radius of curvature. In other words, the loss can increase rapidly as the structure size is reduced. However, using a photonic bandgap, since modes within the bandgap are disallowed, the loss is not directly related to the cavity size (ignoring for the moment the loss in the vertical direction). Therefore, the lateral confinement and the device size can, to some extent, be decoupled.

The microcavities were optically pumped normal to the membrane using an InGaAs laser emitting at 980 nm focused to a spot size of approximately 15 μm. The pump laser was pulsed with 10 nsec pulses at a duty cycle of 0.3% to 0.5%. The low duty cycle was used in order to minimize heating of the membrane, which lacks a good thermal conduction path for heat dissipation. Note that as compared with section 4.3, the pumping area has been increased and the pulse width and duty cycle significantly reduced. Luminescence from the quantum wells at $\lambda \simeq 1.55$ μm was collected normal to the membrane, in the same direction as the pump in the same way as in section 4.3 as shown in Fig. 4.11. Hexagonal photonic crystal disks similar to the device in Fig. 4.7 showed a lasing spectrum at room temperature as shown in Fig. 4.16. The lasing spectrum was centered at $\lambda \sim 1645$ nm with a linewidth measured to be less than ~ 2Å(limited by the spectrometer resolution). The lasing wavelength was significantly red-shifted from the designed quantum well emission peak of $\lambda = 1550$ nm because of heating of the active layer by the pump laser, which shifted the gain peak towards longer wavelengths. These lasers were fabricated with a lattice spacing of a = 640 nm. For a lasing wavelength of 1645 nm, this corresponds to a normalized frequency of 0.389, within the photonic band gap shown in Fig. 4.6, near the bandgap center frequency of 0.406. Fig. 4.16 also shows a number of side modes, spaced by $\sim$ 30 nm with full-width half-maximum (FWHM) linewidths of 20 nm, corresponding to a cavity quality factor Q $\sim$ 80. However, the large number of modes predicted for this cavity would suggest that these spectral peaks probably correspond to a large number of closely spaced modes that cannot be resolved because of the spectral resolution in this measurement. It is likely that the Q of the modes are actually much higher, but due to the large size of this cavity, are not spectrally resolvable.

The light output versus pump power response for the laser is shown in the inset of Fig. 4.17. Lasing threshold occurred at a peak pumping power of 66 mW. The relatively high threshold required is due to the mismatch between the pumping profile and the lasing mode, the possibly low Q and the spectral mismatch of the mode and the gain peak for this non-optimized structure. For a whispering gallery-like mode as shown in Fig. 4.8, the majority of the field intensity lies around the perimeter of the cavity. However, optically pumping the device with a Gaussian beam concentrates the peak pumping power at the center of the cavity. This poor pump to mode overlap was experimentally verified. Lasing occurred with a pump spot size of 15 μm; however, when the pump spot was focused to smaller sizes (2 - 10 μm), it was not possible to reach lasing threshold even with peak pump powers up to approximately 150 mW. The lasing mode in Fig. 4.16 does not correspond to one of the prominent equispaced ($\Delta\lambda = 30$ nm) modal peaks but occurs between two such resonances. Below threshold, only these regularly spaced side modes are visible with very little emission occurring at the lasing wavelength. This indicates that these side modes have a strong overlap with the pump profile, giving strong spontaneous emission, but low Q so that the lasing threshold is not reached. This type of mode can be seen in Fig. 4.9. From the electron micrograph Fig. 4.7, it can be seen that the two corners of the hexagon lie only 4 lattice spacings from the boundary of the patterned area (at the far left and

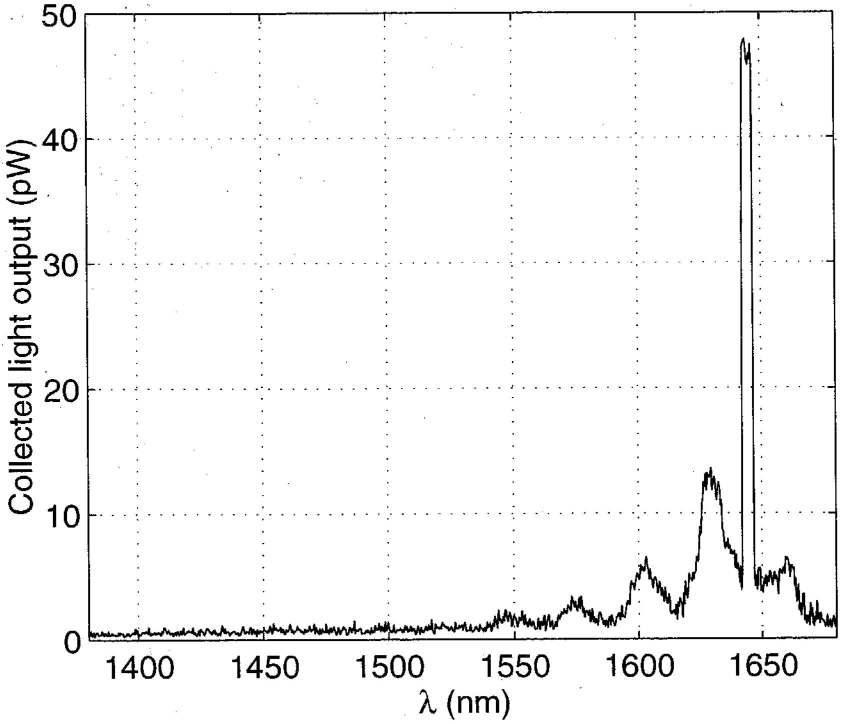

Figure 4.16: Spectrum from a lasing hexagonal PBG disk slightly above threshold with a spectral resolution of 5 nm. The lasing line is clearly visible at 1650 nm.

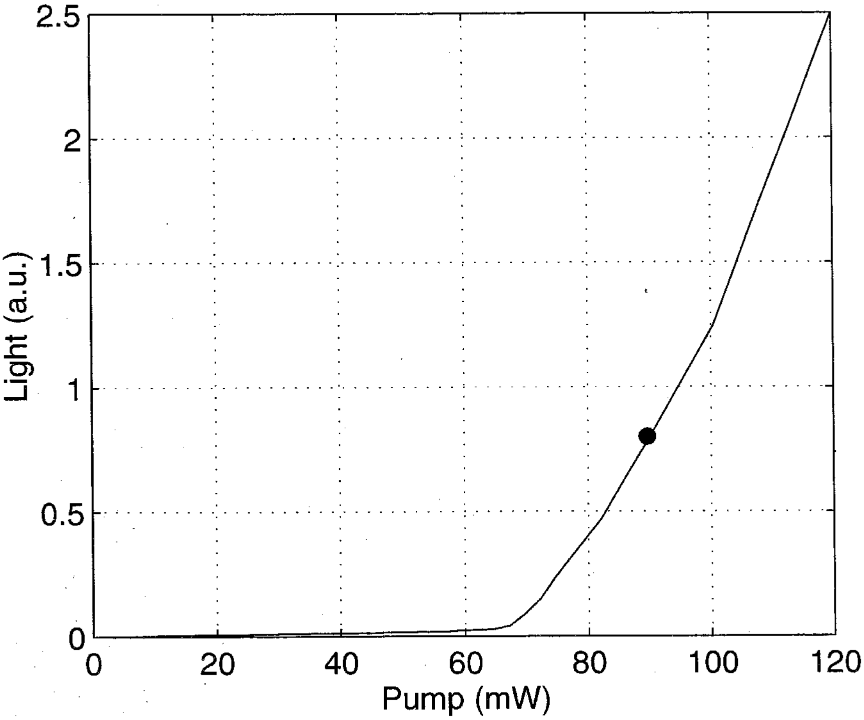

Figure 4.17: Light output versus pumping power. The dark circle indicates the power for the spectrum in Fig. 4.16.

far right of the structure). At these points, a mode such as the one shown in Fig. 4.9 can suffer significant field tunneling through the thin photonic crystal region resulting in a reduced mode Q. This behaviour can be seen qualitatively in Fig. 4.9 at the far left and far right corners of the hexagon. The lasing mode is a much higher Q mode, which lowers the lasing threshold but has a relatively poor overlap with the pump. These regularly spaced modes have been discussed in the previous section and in [65].

Finite difference time domain calculations have shown that the relatively large hexagonal cavities exhibit an extremely complex modal structure including whispering gallery-like modes (Fig. 4.8), as well as more plane-wave like modes reflecting between opposing faces of the hexagon (Fig. 4.9). However, because the photonic crystal has a very wide bandgap (and is thus highly reflective over a wide range), these can all be relatively high Q modes. This suggests the possibility of using pumping geometry to select the lasing mode (and therefore also the lasing wavelength) due to the differences in spatial field distribution between the modes. By adjusting the pump beam alignment with the laser cavity, we have been able to observe an abrupt shift of the lasing wavelength to $\lambda = 1660$ nm corresponding to one of the previously mentioned regularly spaced modes. The sub-threshold spectrum and spectra for the same device lasing at two different wavelengths is shown in Fig. 4.18.

The narrow peaks visible in Fig. 4.18c appear due to a combination of the higher spectral resolution used in this measurement and the change in pumping geometry. As discussed in section 3.7, the relative spontaneous emission depends only on the differences in overlap between the pumping region and the mode profile. Conceptually, the mode switching demonstrated in Fig. 4.18 may be explained schematically as shown in Fig. 4.19. The original lasing mode of Fig. 4.16 and Fig. 4.17 (the same mode as Fig. 4.18b) did not appear in the sub-threshold spontaneous emission (Fig. 4.18a). As shown in section 3.7, this is possible if the mode-pump overlap is small but the modal Q correspondingly high. This case is shown schematically on the right in Fig. 4.19. The modes appearing in the spontaneous emission spectrum may be qualitatively more like the case shown schematically on the left in Fig. 4.19. By adjustment of the pumping area, the relative balance between overlap and Q between

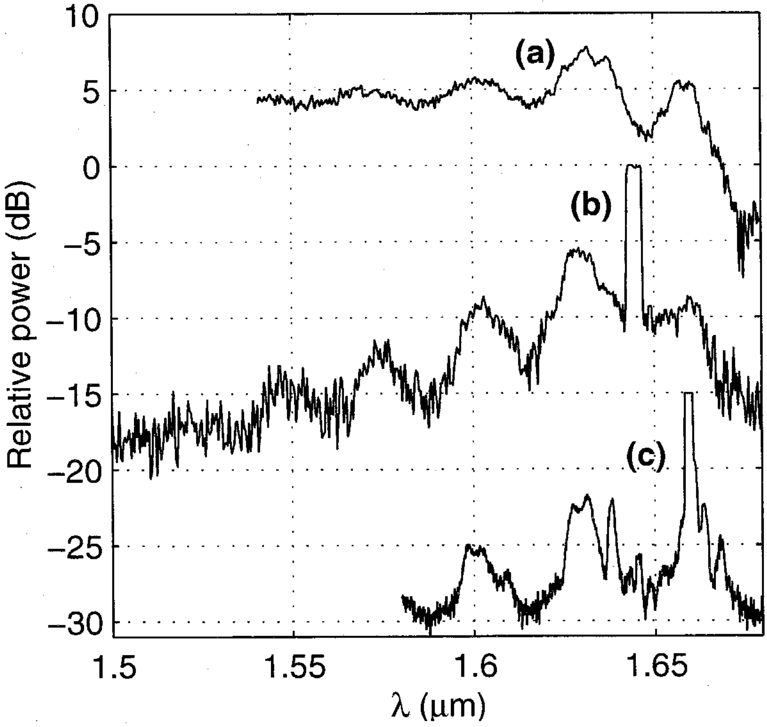

Figure 4.18: Spectra from hexagonal microcavity above and below threshold showing mode selection by changing the pump geometry. (a) Below threshold spectrum showing broad peaks regularly spaced by approximately 30nm. (b) Above threshold lasing spectrum with lasing peak appearing exactly at a minimum in the spontaneous spectrum. (c) Above threshold lasing spectrum after pump geometry adjustment showing shift to lasing at a peak in the spontaneous emission spectrum. The fine structure appears because of the higher spectral resolution used for this measurement.

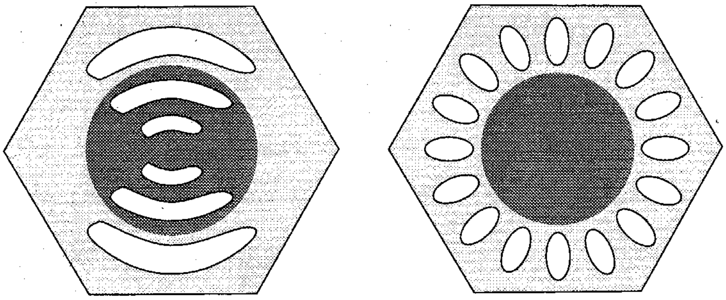

Figure 4.19: Schematic of different modes and their overlap with a circular pump region in a hexagonal planar microcavity. The light pseudo-elliptical regions represent the field energy peaks for the modes. The dark circle represents the circular pumping region.

the modes changes and lasing can change modes. Since the lasing mode in Fig. 4.18c corresponds with a peak of the sub-threshold spontaneous emission spectra, it is likely that this mode may have a strong overlap with the pumping area but a lower Q than the lasing mode in Fig. 4.18b. It should be noted, however, that the complexity and large number of the modes in this cavity preclude any conclusive discussion regarding the relative effects of enhanced spontaneous emission into the modes and mode-pump overlap.

4.5 Summary

In summary, we have demonstrated planar hexagonal disk lasers based on a two-dimensional photonic band gap structure in the InP material system. Mode peaks in the sub-threshold spontaneous emission spectra were observed only in the cases where the photonic bandgap was tuned to overlap with the semiconductor quantum well emission band. Lasing occurred at room temperature under pulsed pumping conditions in spite of the poor thermal conduction path for heat removal. Different lasing modes in the disk were selected by adjusting the pump alignment. A relatively high lasing threshold was observed due to the poor overlap between the pump and the lasing mode and the relatively high membrane temperature. Heat dissipation could be improved by including a supporting post similar to that found in microdisk lasers or by mounting the membrane onto a low index substrate to conserve the index contrast confinement but provide a heat conduction path.

The relative effects of enhanced spontaneous emission into a mode and the lasing threshold were seen through lasing mode switching and the subthreshold emission spectrum. However, the interpretation of the results is difficult due to the large number of modes supported by this microcavity. Reduction of the microcavity size would reduce the number of supported modes and may allow a more definitive interpretation of lasing results.

Chapter 5 Photonic bandgap defect mode cavities

5.1 Introduction

Localized electromagnetic modes can be achieved by introducing defects within the photonic crystal lattice. These so-called photonic crystal "defect" cavities can be considered simply as a limit in the size reduction (with correspondingly fewer modes) of the hexagonal photonic bandgap disk microcavity discussed in chapter 4. Particularly in the microwave regime, these have attracted considerable interest since their first observation in 1991 by Yablonovitch et al. [10] and by McCall et al. [92]. However, experimental work on optical frequency range photonic crystal defects has been hindered until recently by difficulties in fabrication of such small scale structures. Optical photonic crystal defect cavities can potentially provide a means towards very compact microcavity light sources, which are necessary components for the construction of high density integrated optical circuits [11]. The use of photonic crystals inherently provides the flexibility to lithographically control the defect mode radiation pattern [27] and emission wavelength through geometry.

Defects within a two-dimensional photonic bandgap crystal have been demonstrated [93] in the millimeter range to be able to achieve a cavity-Q on the order of 10^4. However, in semiconductor optical photonic crystal structures, finite hole depth and waveguide geometry have been shown to strongly limit the possible mode confinement [48, 78, 80] as compared to an infinite two-dimensional crystal. Recently Labilloy et al. [63] have observed two dimensional light confinement in a semiconductor disk structure with a cylindrical symmetry one-dimensional periodicity used for lateral mode confinement. The spontaneous emission properties of large hexagonal microcavity structures using two-dimensional photonic bandgap crystals for confinement have also been previously studied [64, 65] and discussed in chapter 4. We have recently demonstrated room temperature lasing in such structures under optical pumping [66]. Defect modes in two dimensional photonic bandgap crystals have been studied both numerically (see for example [94, 95]) and experimentally in the microwave regime [92] however experimental studies of two dimensional photonic crystal defects in the optical regime have been hampered by the nanometer-scale fabrication required to generate these structures. However, they are of significant interest because of the extremely small modal volumes possible [27, 28, 29]. In addition to the small modal volumes, these two-dimensional defect cavities have been theoretically predicted [27] to be able to achieve relatively high $Q > 10^4$ if the design is properly optimized. Vuckovic et al. [96] have also shown theoretically that lasers made in such cavities can exhibit large spontaneous emission couplings (β-factor > 0.7). Spontaneous emission and defect mode tuning have been presented in [97]. Lasing in semiconductor photonic crystal defect microcavities has been demonstrated [67] at low temperatures and at room temperature [68].

The defect cavities discussed in this chapter are air-suspended membrane structures patterned with a triangular lattice of air holes and are similar in geometry to the larger hexagonal microcavities discussed in chapter 4. A schematic of the air-suspended membrane microcavity structure is shown in Fig. 4.1. Fabrication followed a similar procedure that described in section 4.2 and the process flow in shown in Fig. 4.2. Scanning electron micrographs of a typical defect cavity device are shown in Fig. 5.1 and Fig. 5.2 with the relevant structural parameters indicated. Similar to the hexagonal microcavities discussed in chapter 4, the membrane epitaxy for the defect mode devices in this chapter is shown in Table 4.1 and the photonic crystal lattice was nominally designed for $r/a \approx 0.35$. Using a three-dimensional FDTD algorithm, two-dimensional electric field amplitude distributions in the slab plane and perpendicular to the slab plane, for a defect cavity mode are shown in Fig. 5.3 (which will be referred to as the x-mode) and Fig. 5.4 (y-mode). Due to the symmetry of the cavity, this mode of the cavity is doubly degenerate.

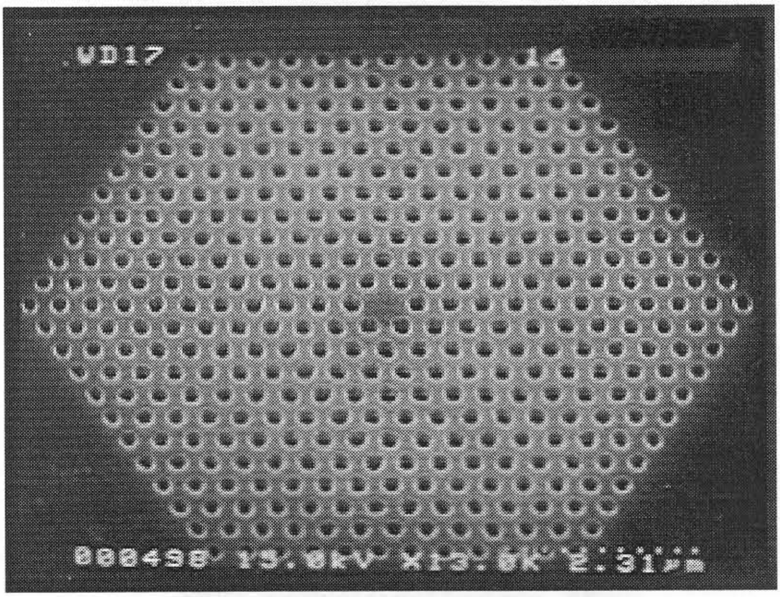

Figure 5.1: Oblique angle SEM image of typical 2-dimensional photonic crystal defect cavity fabricated in an InGaAsP semiconductor slab.

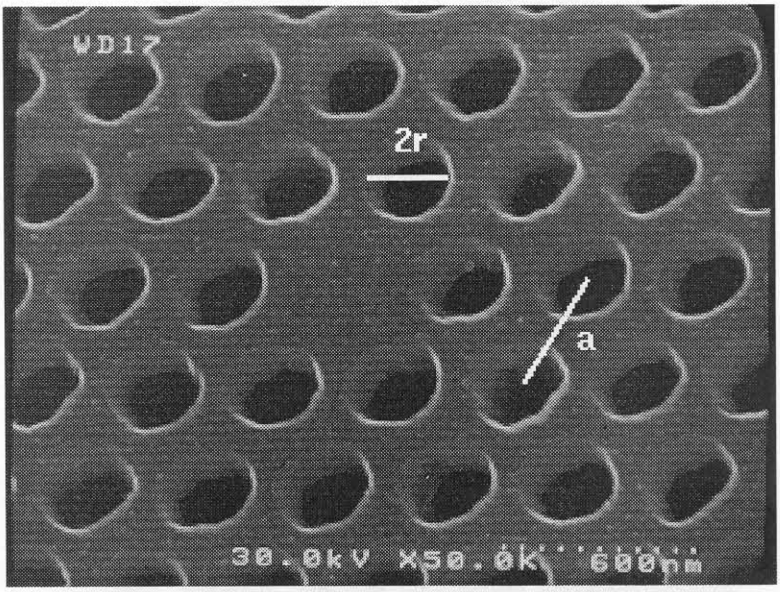

Figure 5.2: Close-up oblique angle SEM image of the 2-dimensional photonic crystal defect cavity seen in Fig. 5.1. The structural parameters defining the photonic structure are indicated.

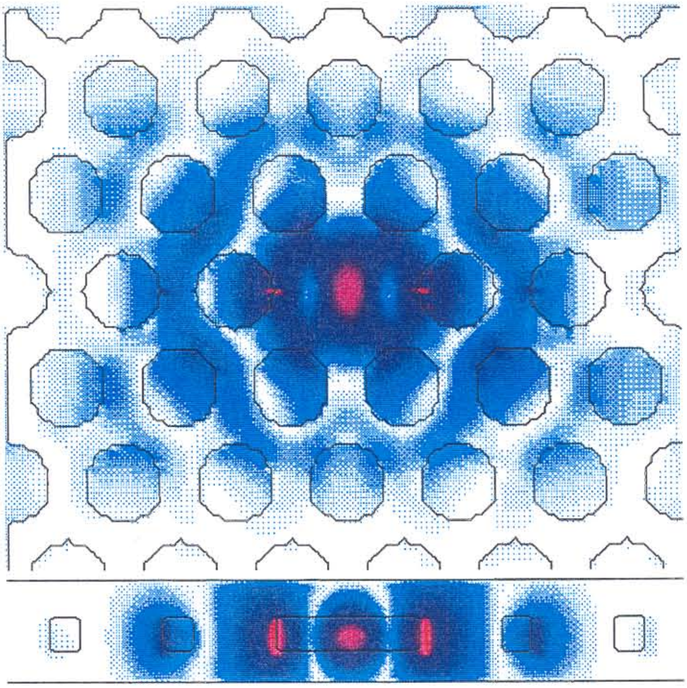

Figure 5.3: Two-dimensional slice through the slab showing the defect x-mode electric field magnitude distribution with r/a ~ 0.35. A slice in the x-y plane is shown above with the corresponding y-z plane slice through the center of the defect, below.

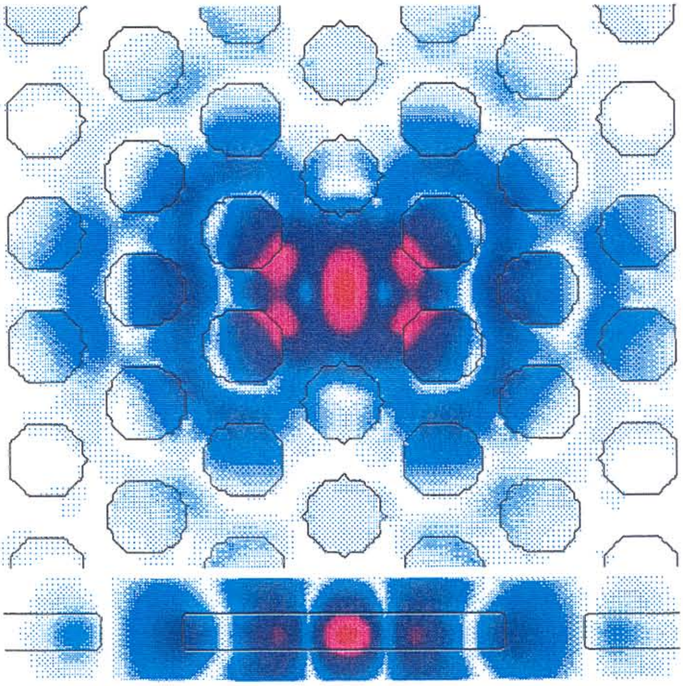

Figure 5.4: Two-dimensional slice through the slab showing the defect y-mode electric field magnitude distribution which is degenerate with the mode in Fig. 5.3. A slice in the x-y plane is shown above with the corresponding y-z plane slice below.

5.2 Measurement of defect emission

The membrane microcavity was optically pumped by 10 nsec pulses at a repetition rate of 100 kHz to 500 kHz from a semiconductor laser ($\lambda = 980$ nm) focused to a spot size of approximately 5 μm. Photoluminescence from the quantum wells at $\lambda \simeq 1.55$ μm was collected normal to the membrane (see Fig. 4.11). The photoluminescence was passed through a monochromator and then detected using a New Focus femtowatt photoreceiver similar to the configuration shown in Fig. 4.10. Fig. 5.5 shows a comparison of the photoluminescence from a semiconductor membrane patterned with the photonic crystal lattice (Fig. 5.5, top) and an identical photonic crystal membrane containing a single defect (Fig. 5.5, bottom). In both cases the photonic bandgap crystal was fabricated with a lattice spacing of a $\approx$ 591 nm and r/a $\approx$ 0.348 measured by a scanning electron microscope. The upper plot in Fig. 5.5 shows that there is essentially no detectable power emitted by the photonic crystal membrane above the noise floor. Given the sensitivity of the detection system, this corresponds to a collected emission power of less than approximately 0.25 fW/nm. When compared to the collected emission power from a simple unpatterned membrane, this is a reduction in the detected spontaneous emission power by more than one order of magnitude.

The decrease in emission power can be explained by three possible effects. First, since the photonic bandgap crystal is a relatively high surface-to-volume ratio structure, significant non-radiative recombination due to free surfaces would be expected and could dominate the total carrier recombination rate. The defect within the photonic crystal has a slightly lower surface-to-volume ratio thereby reducing the contribution of non-radiative surface recombination. This is a serious concern in the design of an active device since a non-radiative dominated recombination rate could lead to very low device efficiency. This will be discussed further in section 5.3. The second possible effect could be a change in the spatial distribution of radiation. It is important to recognize that this is not a measurement of total emission power, but rather, the emission power into a solid angle defined by the numerical aperture of

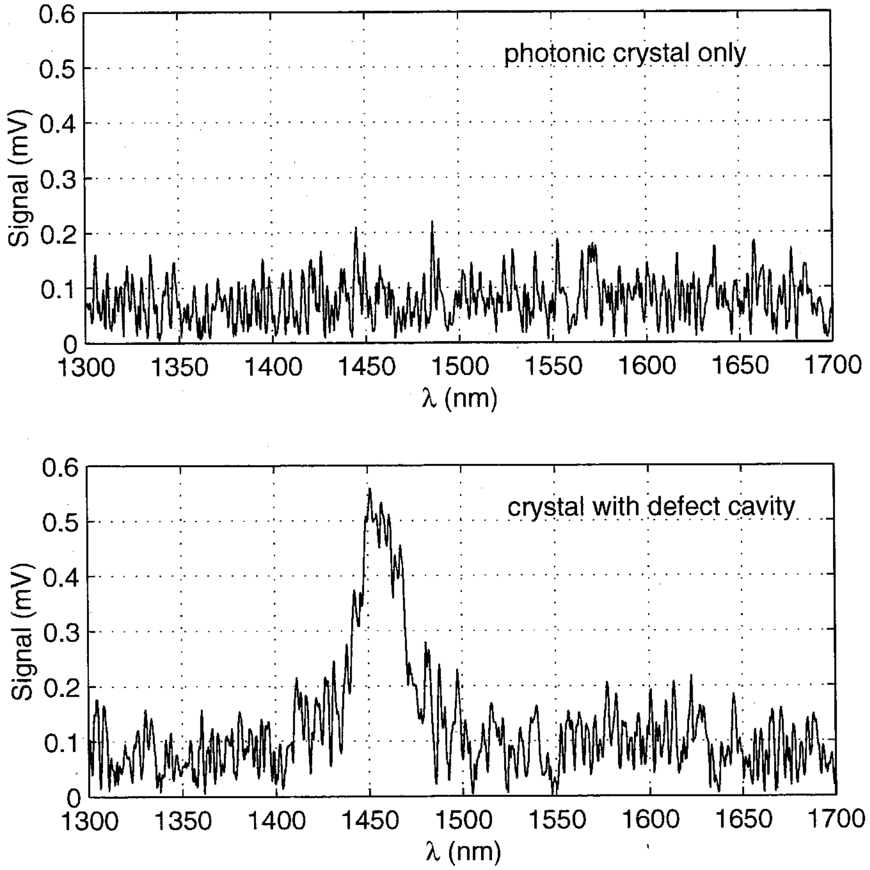

Figure 5.5: Comparison of photoluminescence spectra from a photonic crystal slab and a slab with a single defect cavity with a lattice spacing of a $\approx$ 591 nm. The top figure shows that the emission spectrum from the crystal slab has been inhibited below our measurement sensitivity limit. The lower figure shows the cavity resonance.

the collection optics. In this measurement, a lens system with a numerical aperture of NA = 0.6 was used. The perceived changes in the emission power could be the result of a change in the collection efficiency and not necessarily a change in the emitted power. Theoretical simulations of these types of microcavities [27, 28, 29, 98] have shown that the cavity mode and the emission pattern are strongly dependent on the cavity geometry, which could in turn affect the collection efficiency. The third possible effect contributing to the reduced emission power could be a fundamental modification of the spontaneous emission rate because the active material emission linewidth lies completely within the two-dimensional photonic band gap. When a single defect is introduced into the photonic lattice, a strong emission peak is seen as shown in the lower plot in Fig. 5.5. When the defect is pumped at a time averaged power of 250 μW, the total integrated power detected is enhanced by a factor of more than 100× over that for the photonic crystal alone (with no defect cavity). Given the difference in surface-to-volume ratio between the photonic crystal structure and the defect microcavity, such a large change in the total integrated emission power is not expected assuming a constant surface recombination velocity for the two cases. This suggests that a fundamental modification of the spontaneous emission rate may be occurring. However, as previously discussed, this could also be partially attributed to a change in collection efficiency. The modification of the spontaneous emission rate in the photonic crystal slab structure (without cavity) is discussed theoretically in chapter 6 and experimentally in chapter 7.

The defect emission peak shown in Fig. 5.5 is centered around a wavelength of λ = 1455 nm for a lattice size of a $\approx$ 591 nm giving a normalized frequency for the defect mode of a/λ = 0.4062. This defect frequency lies very close to the calculated bandgap center, a/λ = 0.4065 shown on the left in Fig. 5.6. The bandstructure was calculated using a three-dimensional FDTD algorithm similar to the results shown in Fig. 4.6. The defect emission peak has a full width half maximum linewidth of approximately 20 nm in Fig. 5.5. This corresponds to a cavity quality factor (Q) approximated as $\lambda/\Delta\lambda \approx 73$, which corresponds very well to a value of $Q \sim 75$ from numerical FDTD simulations [27]. For a structure fabricated in active material, it

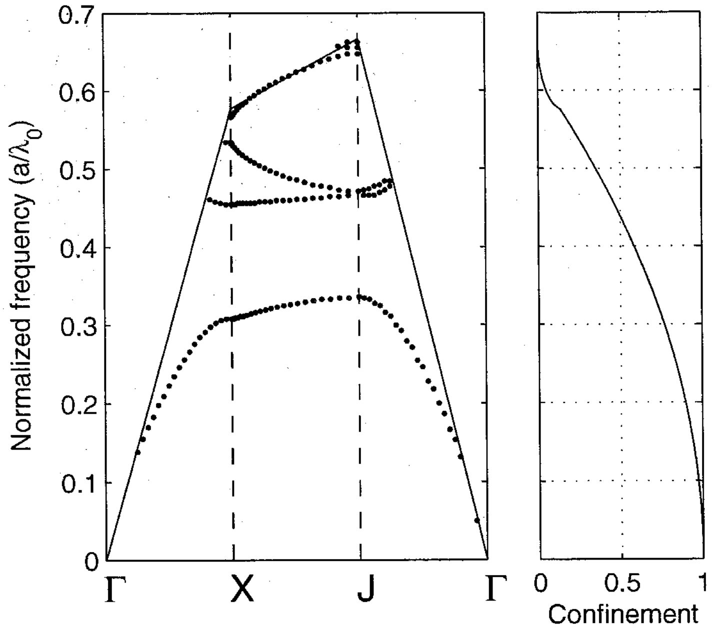

Figure 5.6: *Left* - calculated bandstructure for the 2-dimensional photonic crystal for the design parameters d/a ≈ 0.33 and r/a ≈ 0.35. The band gap lies in the frequency range 0.348 – 0.465 with the midgap at ≈ 0.4065 *Right* - fraction of the first Brillouin zone which lies below the light line.

would be expected that absorption losses should reduce the measured Q as compared to the value derived from a cold cavity calculation. This means that the spontaneous emission linewidth in an active device is not necessarily a good measure of the cold cavity quality factor. The correspondence between the measured values and those predicted from a passive cavity calculation can be explained by allowing for gain in the active material. If the structure is pumped strongly enough such that significant stimulated emission occurs, a condition can be reached where gain due to stimulated emission helps to compensate the absorption loss. For an active cavity below the lasing threshold, the emission linewidth can be written as follows [75].

$$\Delta\nu_{mode} = \Delta\nu_{1/2}\left(1 - \frac{G_{m0}}{G_0}\right) \tag{5.1}$$

where $\Delta\nu_{mode}$ is the measured emission mode linewidth, $\Delta\nu_{1/2}$ is the cold cavity linewidth, G_{m0} is a parameter proportional to the population inversion $(N_2 - (g_2/g_1)\,N_1)$, which is related to the material gain (or loss) and G_0 is a parameter proportional to the cavity losses (ω/Q). Eq. (5.1) can be interpreted as meaning that for a cavity with absorption, $G_{m0} < 0$, and the measured mode linewidth is larger than the cavity linewidth. For the case of $G_{m0} > 0$ the lasing threshold is reached as $G_{m0} \rightarrow G_0$ and the linewidth narrows. The cold cavity linewidth is only equal to the measured emission linewidth when $G_{m0} = 0$, which implies that the inversion is zero and the active material exhibits neither net gain nor net loss (transparency). Furthermore, since G_0 is proportional to cavity losses (and thus inversely proportional to Q), the slope of the linewidth versus pump power (and thus carrier density) curve is proportional to the cavity Q. If the measured Q $\approx \lambda/\Delta\lambda$ is small, then the deviation from $G_{m0} = 0$ can be larger and still give a reasonable estimate of the actual cavity Q. Conversely, if the Q is large, then the deviation from $G_{m0} = 0$ must be small in order to get a good measure of cavity Q. In this case, the measured linewidth corresponds to a relatively low Q of approximately 80 so that a relatively slow change in linewidth versus carrier density is expected. The emission mode linewidth varied by less than ± 3 nm around approximately 20 nm while sweeping the time-averaged pumping power from 200 μW up to 500 μW. This amount of linewidth change is not significant due to the 5 nm spectral resolution used for this measurement. Stimulated emission in these devices is discussed further in section 5.3.

The relatively low estimated quality factor from these cavities are the result of non-optimized device design. Numerical simulations of the defect cavity Q [27] have shown that the Q depends on the relative position of the bandgap to the light line. This positioning depends on the photonic crystal r/a parameter as well as a parameter that can be considered as characterizing the finite extent of the lattice in the third dimension, d/a (where d is the waveguide thickness). Physically, the dependence of the Q on the vertical confinement can be understood simply by a careful examination of the band structure. For defects within a photonic band gap at higher frequencies, a larger portion of the first Brillouin zone lies above the light line, as shown qualitatively in Fig. 5.6 (right). This plot shows the fraction of the first Brillouin zone confined below the light line for the slab waveguide as a function of normalized frequency. This can be interpreted as the fraction of solid angle in three dimensions, which can be affected by the two dimensional photonic lattice. Only emission into this affected solid angle can be strongly modified. For defects within a photonic band gap at lower frequencies, the portion of the first Brillouin zone within the band gap and below the light line increases. Therefore, the effective Q can be increased by moving the defect frequency to lower frequencies. This qualitatively indicates that for a given photonic band gap width, stronger confinement and therefore larger cavity quality factors would be expected for lower mid-gap frequencies (and hence also defect frequencies assuming that the defect remains near the mid-gap position). This type of relatively simple confinement estimate can be used as a convenient design tool to optimize the cavity geometric parameters.

This type of behavior agrees qualitatively with the experimentally measured linewidths for different devices. The position of the bandgap relative to the light line is inversely related to the parameter d/a as shown in Fig. 5.7. Therefore, this parameter can be used to control the cavity Q. Measurements on defects fabricated with r/a = 0.35 and d/a = 0.43 result in a bandgap at slightly lower frequencies and, therefore, deeper below in-plane light line, with a calculated defect frequency of $a/\lambda = 0.34$. These devices show narrower linewidths of $\Delta\lambda = 7$ nm and therefore a correspondingly larger Q of ~ 250 in agreement with FDTD numerical simulations. Compare this with the emission spectrum shown in figure 5.5 where a cavity Q of approximately $\lambda/\Delta\lambda = 73$ was observed for a normalized defect frequency of $a/\lambda = 0.41$. These higher Q defect microcavities are discussed in greater detail in section 5.5.

5.3 Defect tuning and stimulated emission

Photonic crystal defect cavities provide an inherent flexibility for control of the cavity emission through lithographic changes in the geometry [89]. Figure 5.8 shows the spontaneous emission spectra for photonic crystal defect cavities fabricated with different lattice spacings from a = 960 nm to a = 512 nm. The dark gray shaded regions represent the range of ±1% around the numerically estimated defect frequency in this structure of $a/\lambda \approx 0.407$. The lighter gray shaded region represents the approximate

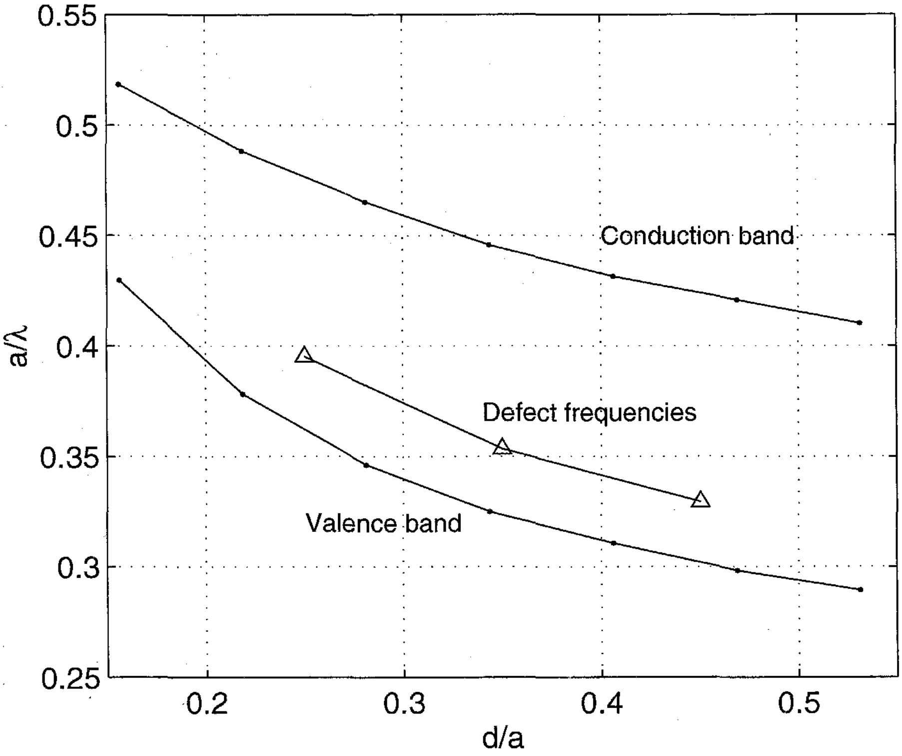

Figure 5.7: Band edge and defect frequency dependence on slab thickness from three-dimensional FDTD calculations. These band edge and defect frequencies have been calculated for r/a=0.35.

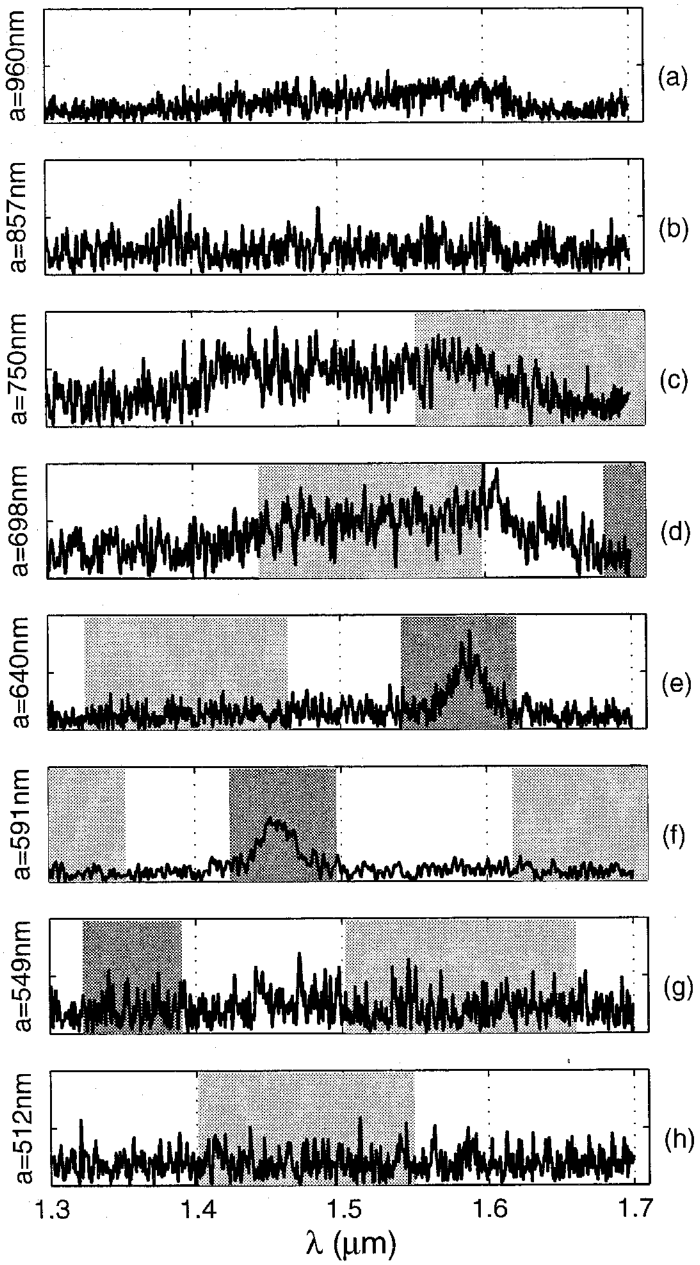

Figure 5.8: Defect cavity spontaneous emission tuning. The normalized spontaneous emission spectrum for defect cavities based on photonic crystals with different lattice spacings are shown with the lattice spacing 'a' given to the left of each plot. The dark gray bands indicate the FDTD estimated defect frequency $a/\lambda \approx 0.407 \pm 1\%$. The light gray bands indicate the estimated bandgap edge positions.

range for normalized frequencies where numerical simulations predict a photonic band gap (from 0.348 to 0.465 for d/a = 0.33 and r/a = 0.35). This particular choice of parameters is only accurate for one of the devices shown in figure 5.8 since it has been shown that for this geometry, there can be a noticeable shift in the bandgap towards higher frequencies as the lattice spacing a increases relative to the fixed waveguide slab thickness d. However, systematic fabrication errors act to negate this bandgap shift which coincidentally results in the predicted defect frequency being approximately correct for the resonances shown in Fig. 5.8. The bandgap shift and the source and type of systematic fabrication errors are discussed in section 5.4.

When the photonic crystal lattice size is tuned so that the band gap occurs at longer wavelengths than the spontaneous emission bandwidth of the material (Fig. 5.8a) a broad spontaneous emission spectrum similar to an unpatterned sample is seen (compare with the unpatterned material spectrum from Fig. 4.12). Fig. 5.8b-d show cases where the band gap frequency is tuned to longer wavelengths than the emission bandwidth as in Fig. 5.8a. However, the spectrum is modified from the smooth spontaneous emission peak characteristic of the unpatterned material. These spectral features are caused by the modes of the photonic crystal bands (the 'conduction' band modes) which slightly modify the spontaneous emission. Peaks in the spectra corresponding to the different individual conduction bands are not clearly separated in this case because the emission is angle-integrated around the in-plane $k = 0$ point over the solid angle defined by the collection optics with a numerical aperture of 0.60. Angle resolved spontaneous emission spectra from photonic crystal slabs have been used to experimentally map portions of the photon bandstructure by Boroditsky et al. [99].

When the photonic band gap and the defect mode frequency are well aligned with the emission bandwidth in Fig. 5.8e, a narrow emission peak can be seen at $\lambda \simeq 1.58$ μm with most of the emission at other wavelength being suppressed. The defect mode frequency can be tuned across the emission bandwidth while maintaining a similar cavity quality factor as well as emission power. Fig. 5.8f shows a defect mode peak tuned to shorter wavelength at $\lambda \simeq 1.46$ μm. This represents a tuning of over 120 nm while maintaining similar emission power and linewidth. It should be noted that the apparent higher signal-to-noise in Fig. 5.8f is not due to larger signal power from this defect as compared to Fig. 5.8e. The signal-to-noise change is due simply to a change in the signal bandwidth, which results in reduced noise. When the defect mode is further tuned to wavelengths shorter than the emission bandwidth, no significant spectral features are observed (Fig. 5.8g,h). Emission into the photonic bands below the band gap (the 'valence' band modes) is not observed because these modes lie completely below the light line and are thus confined within the membrane plane [28, 29]. The defect mode in Fig. 5.8g is also not observed because it lies off the emission band as seen in Fig. 5.8a.

The light output from the defect microcavity versus pumping power is shown in Fig. 5.9 for the device whose spontaneous emission spectrum is given in Fig. 5.8e. The expanded view (Fig. 5.9 inset, lower right) shows a gradual but clear change in the slope at an average pump power of approximately 30 μW. This change in slope is due to a change in the radiative efficiency as the pump power is increased due to the onset of stimulated emission. At higher pump powers, starting at approximately 750 μW, the slope efficiency gradually decreases until 1000 μW where the output power actually begins to decrease. This reduction in radiative efficiency is attributed to the changing active layer temperature and carrier density as the pump power is increased. The higher temperature leads to an increase in point defect and surface non-radiative recombination due to the increased carrier diffusion coefficient. In addition, and probably more importantly, the larger carrier density increases the contribution of Auger recombination, which is significant in long wavelength materials such as InP and increases as the cube of the carrier density as well as increasing exponentially with temperature. At high pumping powers, these non-radiative recombination terms dominate the total recombination rate resulting in decreasing output power versus increasing pump power.

This first evidence of stimulated emission at room temperature is significant for two reasons. As discussed at the beginning of section 5.2, the strong reduction in spontaneous emission power can be due to both non-radiative processes dominating

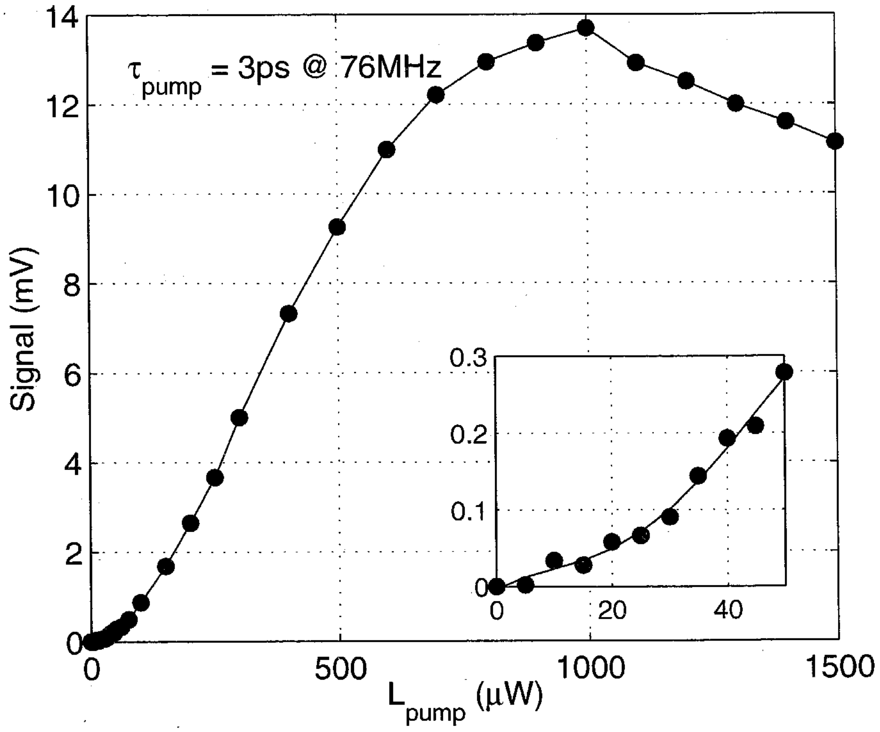

Figure 5.9: Defect cavity light output versus average pump power plot. The inset figure shows an expanded plot of the light output at low pump powers (bottom). The light output shows a clear change in slope efficiency indicating the onset of stimulated emission at approximately $P_{avg} = 30\ \mu W$. Above 1 mW, the roll-off in the radiative efficiency can be seen as the device begins to overheat.

the total carrier recombination and also a fundamental modification of the spontaneous emission rate. The first case would make useful light emitting devices very difficult because of the low radiative efficiency. Fig. 5.9 shows that the non-radiative processes, which tend to increase with increasing pumping power, do not dominate in the defect microcavity until well past the threshold for the onset of stimulated emission. The observation of stimulated emission is also significant with regards to the measurement of linewidth and its relation to the cavity Q. Eq. (5.1) showed that the measured linewidth corresponds to the actual cavity Q, only when the inversion is zero (no net gain or loss) which occurs at the onset of stimulated emission. This means that a good estimate of the cavity linewidth can be made by performing the emission linewidth measurement near the stimulated emission threshold point. Although evidence for stimulated emission was seen, lasing was not achieved with these devices. This is likely due to the relatively low Q for these microcavities as well as the expected fast carrier loss to surface recombination.

5.4 Proximity effect in electron beam lithography

As previously mentioned, there is a systematic shift of the bandgap energy due to the change in the d/a parameter since the slab thickness is constant for all devices, determined by the material epitaxy. Assuming constant r/a, the bandgap shift versus d/a is shown in Fig. 5.7 along with the associated shift of the defect frequency. However, examination of the tuning spectra shown in Fig. 5.8 shows that for Fig. 5.8e and Fig. 5.8f, the defect mode frequency occurs at the same normalized frequency whereas from Fig. 5.7 an approximately +3% shift in the normalized frequency would be expected. For a lattice spacing of 591 nm (Fig. 5.8f) this would result in a 43 nm shift to shorter wavelength. The deviation of the measured emission wavelength from the prediction of Fig. 5.7 as due to a systematic error in the fabrication process.

Careful examination of the devices by scanning electron microscope reveals that there is a small but systematic decrease in the parameter r/a with increasing lattice spacing a as shown in Fig. 5.10, which also leads to a shift in the bandgap energy.

This occurs during the electron beam lithography process. Since the electron beam is charged, there can be an electrostatic size-dependent proximity effect during the electron beam exposure. The charged electron beam interacts with residual charge left in the photoresist after exposure resulting in size dependent exposure of the resist for a constant exposure beam current. Size dependent exposure also results from electron backscattering from the substrate as well as secondary electron emission which can affect other exposures as far as 50 μm away [100]. This proximity effect can be corrected during the beam writing process but compensation can become quite complex depending on the minimum feature size and pattern geometry (see for example [101, 102, 103, 104]). Correction of the proximity effect can have an important effect, not only as a function of lattice size as shown in Fig. 5.10, but also within one device. Holes near the defect cavity experience a different local environment and therefore a different proximity shift in the lithography than holes away from the cavity. Therefore there can be a systematic shift in hole sizes within one photonic crystal pattern due to the proximity effect.

5.5 Defect low temperature lasing

As shown in Fig. 5.6, the possible confinement from the thin slab structure increases at lower normalized frequencies because a larger fraction of the two-dimensional Brillouin zone falls below the light line. The defect cavity Q can therefore be increased as discussed in 5.2 by increasing the slab thickness since this results in a shift of the bandgap to lower frequencies shown in Fig. 5.7. The epitaxial structure used for the laser structure is shown in Table 5.1 consisting of 4 slightly compressively strained quaternary quantum wells with emission designed for 1.55 μm emission. The strained quantum wells couple primarily with TE modes (electric field in the plane of the slab) which corresponds with the defect cavity mode polarization. Fabrication followed essentially the same procedure as previous devices and is schematically shown in Fig. 4.2.

A top view scanning electron micrograph of the defect cavity with the nearest

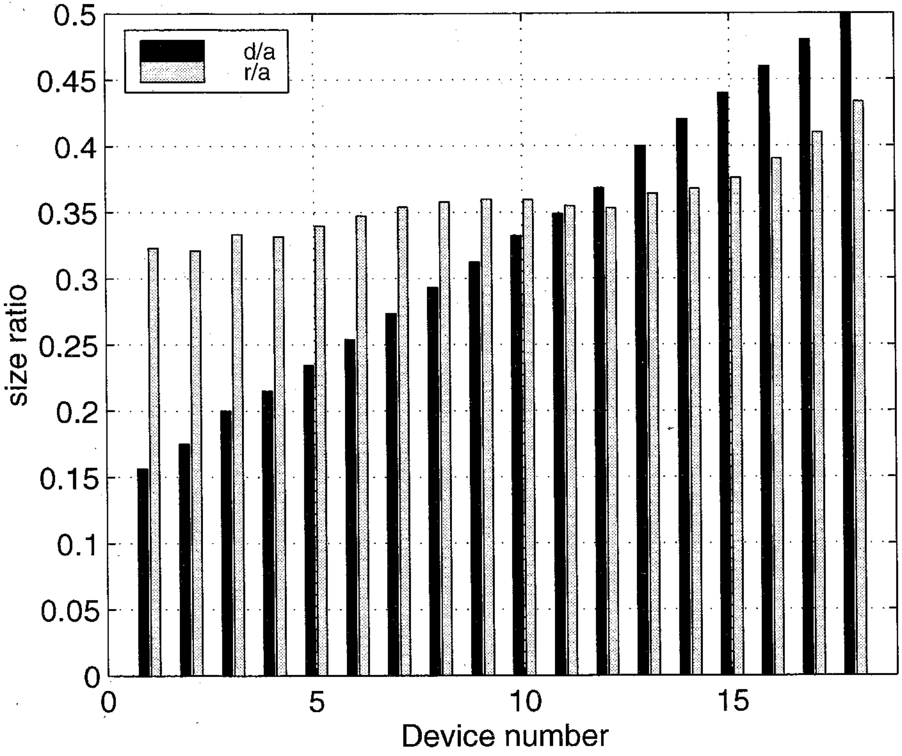

Figure 5.10: Measured devices parameters for sample Ortel-4 by scanning electron microscope. Due to electron beam proximity effects during lithography, there is a increase in the relative hole radius as the hole spacing is decreased (increasing device number).

220 nm	62 nm InGaAsP
	9 nm InGaAsP QW
	20 nm InGaAsP barrier
	9 nm InGaAsP QW
	20 nm InGaAsP barrier
	9 nm InGaAsP QW
	20 nm InGaAsP barrier (Eg=1.22 μm)
	9 nm InGaAsP QW (+.85 % compressive strain)
	62 nm InGaAsP (Eg=1.22μm)
684 nm	664 nm InP buffer layer
	20 nm InGaAs etch stop

Table 5.1: Modified InGaAsP epitaxy for higher Q and lasing devices.

neighbour holes in the x-direction enlarged to split the defect mode degeneracy is shown in Fig. 5.11. The defect cavity was formed within a triangular lattice of air holes photonic crystal with a lattice size of a = 515 nm and r/a ≈ 0.35. The measured hole radius was r = 180 nm and the two enlarged nearest neighbour holes have radii of r′ = 240 nm. Three-dimensional FDTD calculations for this geometry [67] assuming a material index of refraction of n = 3.4, predict a Q of 250 and a normalized defect mode frequency (for the degeneracy split structure) of a/λ ≈ 0.34. Following [29] and [27], the effective modal volume for the defect cavity mode can be defined as

$$V_{eff} = \frac{\int_V \epsilon(\vec{R}) \left|\vec{E}(\vec{r})\right|^2 d^3r}{\max\left(\epsilon(\vec{r}) \left|\vec{E}(\vec{r})\right|^2\right)} \tag{5.2}$$

Using this definition, the degeneracy split defect mode in this microcavity has an effective modal volume of 2.5 times a cubic half-wavelength in the material $\left[2.5\,(\lambda/2n)^3\right]$. For the lattice size shown in Fig. 5.11 and a mode frequency of 0.34, this corresponds

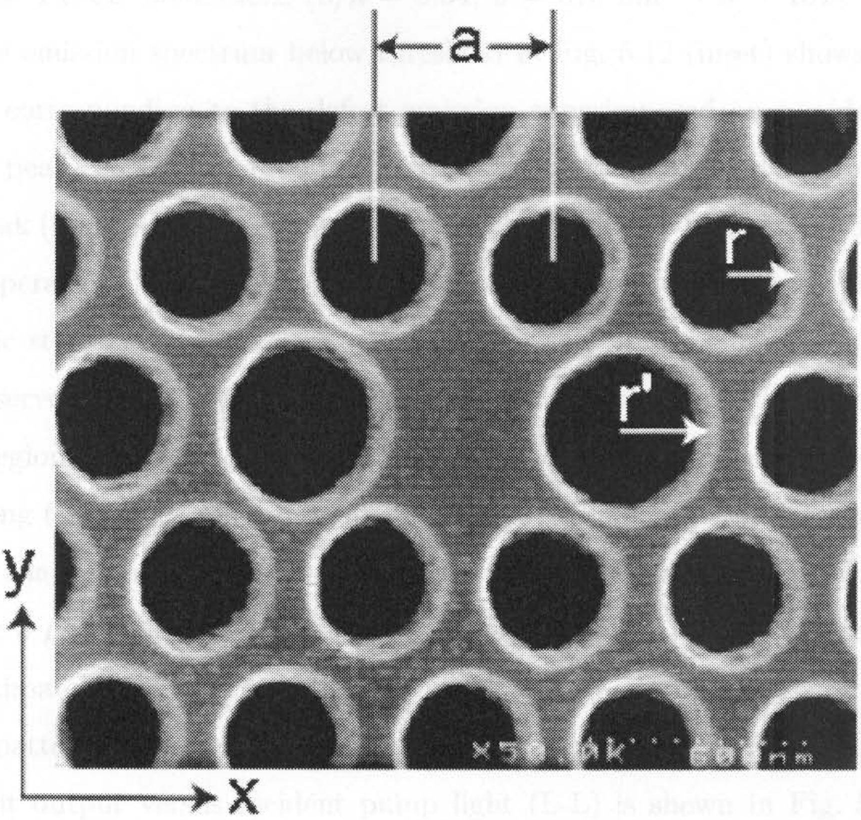

Figure 5.11: Top view of defect cavity with the two nearest neighbour holes in the x-direction enlarged (with radius r′) to split the mode degeneracy. The lattice size a = 515 nm and the hole radius of ∼ 180 nm (r/a = 0.35).

to a modal volume of 0.03 μm^3.

The laser cavity was optically pumped using a similar configuration used previously and shown in Fig. 4.10. The sample was mounted in a continuous flow helium cryostat allowing the substrate temperature to be controlled down to approximately 4 K. The complete microcavity device consisted of eight periods of the photonic lattice surrounding the defect region in a hexagonal domain similar to that shown in Fig. 5.1. A pump wavelength of 830 nm was used, focused to a spot size of ∼ 3 μm. The pump was pulsed at a frequency of 4 MHz with a pulse length of 10 nsec. The emission spectrum for this defect cavity is shown in Fig. 5.12. Above threshold, the lasing spectrum, centered at 1504 nm, has a linewidth of less than 2 Å, limited by the spectral resolution of the measurement. This lasing wavelength corresponds very well with the FDTD predictions ($a/\lambda = 0.34$, $a = 515$ nm $\rightarrow \lambda \sim 1515$ nm). The spontaneous emission spectrum below threshold in Fig. 5.12 (inset) shows a narrow small peak corresponding to the defect emission superimposed on a wider, shorter wavelength peak centered at 1460 nm. This wider peak corresponds to the material emission peak (blue-shifted from the design wavelength of 1550 nm due to the lowered sample temperature T = 143 K) and comes from the unprocessed areas surrounding the photonic structure and excited by the tails of the pump beam. This behaviour was not observed previously in Fig. 5.5 and Fig. 5.8. This occurs because the total patterned region in the lasing cavities covers 8 lattice periods around the defect region corresponding to a total area approximately 8 μm in diameter, which is only slightly larger than the 3 mum pump spot size. In the previous case, the pump was focused to a similar 5 μm pump spot, however the total patterned region covered a square area approximately 20 μm across. The complete pump beam was therefore contained within the patterned area so that no excitation of unpatterned material occurred.

The light output versus incident pump light (L-L) is shown in Fig. 5.13. The collected light power at the lasing wavelength was measured and shows the lasing threshold at an incident pump power of 6.75 mW. The relatively large threshold pump power is due to a relatively low Q (although significantly increased over the previous devices) as well as the poor pumping efficiency. For the 3 μm pump spot, the total pumping area is greater than 30 times larger than the defect mode. The detailed structure in the L-L plot near the threshold point has not been conclusively explained but may be due to the combined effects of changing surface and Auger recombination as the pump power is increased (increasing the membrane temperature) along with the changing radiative emission rate due to stimulated emission.

5.6 Summary

The promise of photonic integrated circuits will require the development of very compact, efficient and versatile light sources. Defects within a photonic bandgap crystal have frequently been suggested as a possible solution. Narrow linewidth emission

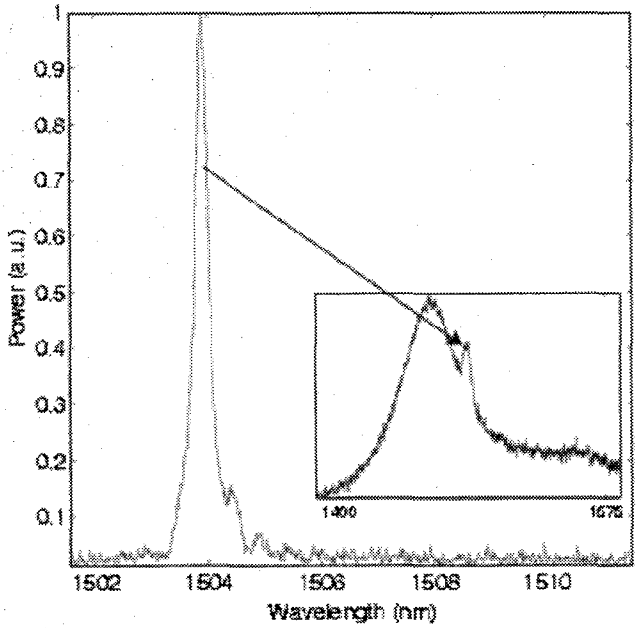

Figure 5.12: Emission spectrum from the degeneracy split defect cavity lasing at 1504 nm with a linewidth < 2 Å(resolution limited). The inset figure shows the emission spectrum well below threshold.

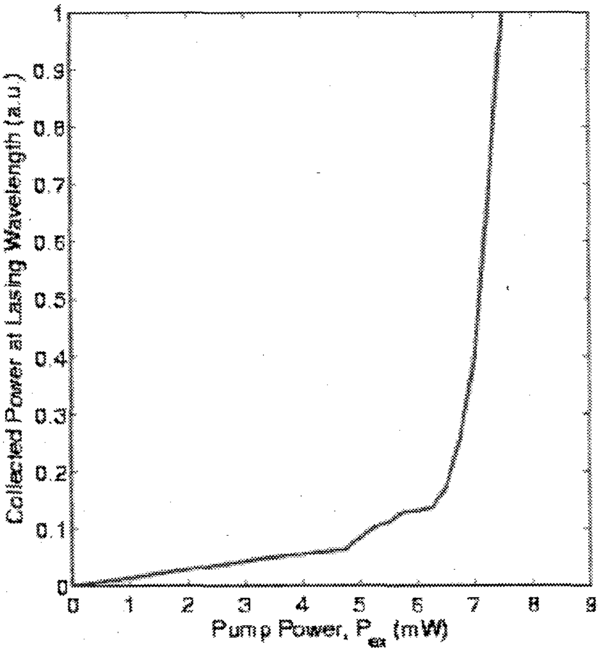

Figure 5.13: Light output versus pumping power at the laser wavelength for the degeneracy split defect cavity. The sample was cooled to 143 K and pumped with 10 nsec pulses.

from an isolated defect in a two-dimensional photonic band gap crystal in the InP material system. This type of cavity has a small modal volume [27] of $\approx 2.5\left(\frac{\lambda}{2n}\right)^3$. The effect of the photonic crystal defect results in a narrow spontaneous emission peak corresponding to the cavity response. Stimulated emission into the defect mode is demonstrated at room temperature under pulsed optical pumping conditions and the mode frequency is tuned lithographically across the material emission bandwidth. The fundamental defect mode degeneracy can be split by adjusting the cavity geometry, leaving a truly single mode microcavity. The cavity Q can also be adjusted by moving the defect mode to lower frequencies. Pulsed lasing under optical pumping at low temperature (143 K) has been demonstrated. Room temperature continuous lasing will require a higher Q cavity design as well as improved heat sinking providing a thermal conduction path for heat removal [16] from the microcavity.

Chapter 6 Spontaneous emission from 2D photonic crystal slabs

6.1 Introduction

Spontaneous emission from a radiating system can be significantly increased [14] or inhibited [15] in a resonant cavity. Photonic band gap (PBG) structures in light-emitting materials have been predicted to be able to exhibit enhanced or inhibited spontaneous emission [7, 8]. The possibility of control over the fundamental spontaneous emission properties has resulted in a great deal of recent interest. One possible application of photonic crystals is the light emitting diode (LED). The external efficiency of LEDs is typically relatively low, primarily due to low extraction efficiency of the spontaneously emitted radiation due to total internal reflection. Many approaches have been proposed to increase this extraction efficiency by enlarging the photon escape cone or using photon recycling [105]. The fundamental spontaneous emission properties of the device can also be modified, for example by use of a Fabry-Pérot microcavity [106]. However, these resonant cavity light-emitting diodes only modify the emission in a narrow spectral range.

In this chapter we show that the in-plane bandgap for a finite two-dimensional photonic crystal slab can be used to achieve an inhibition in the spontaneous emission rate by an order of magnitude even though it lacks a complete photonic bandgap. The effect of dipole position in the photonic lattice on the emission rate is briefly considered. The combination of changes in the emission pattern and the emission rate can result in an enhancement or inhibition of the external quantum efficiency.

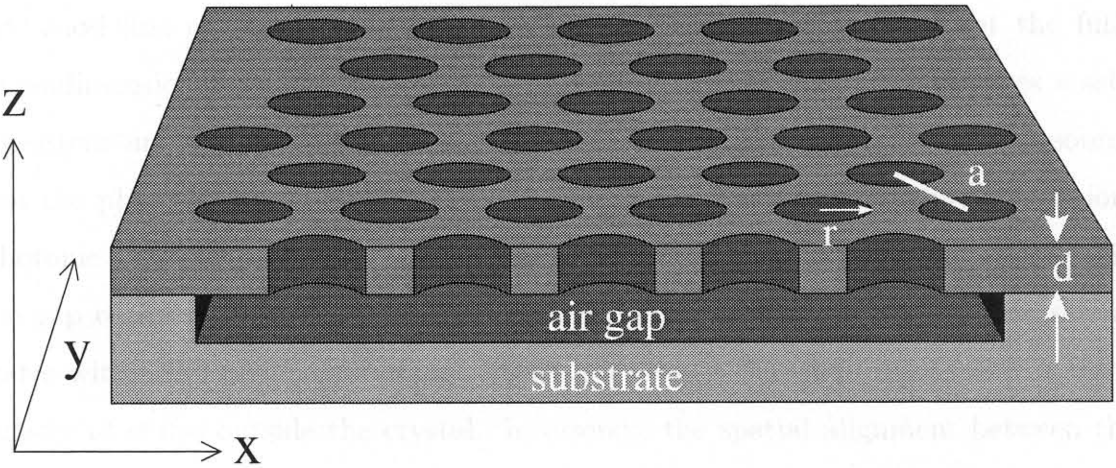

Figure 6.1: Schematic of the air-suspended triangular lattice photonic crystal slab structure.

6.2 Modified spontaneous emission results

6.2.1 Dipole position dependence

Recently [77], a new approach to modify the spontaneous emission and significantly increase the extraction efficiency in LEDs over a wide frequency range by using a thin slab of two-dimensional photonic crystal was proposed as shown in Fig. 6.1. However, only the modification to the emission pattern was considered. In a light emitting structure with residual non-radiative recombination, it is also necessary to consider the radiation rate. In the case where the extraction efficiency is strongly enhanced, if the radiation rate is correspondingly inhibited, the resulting net extracted power may be enhanced or reduced depending on the associated non-radiative recombination rate. It is in fact possible for the net extracted/detected power to be unchanged if the extraction efficiency change is balanced by the change in the radiative efficiency.

Spontaneous emission in a two-dimensional photonic bandgap structure has been theoretically examined for a honeycomb structure [47] as well as the 2D triangular array of holes [46]. However, these previous analysis of emission rate suppression in photonic crystals only estimate the fraction of solid angle that can be affected by the photonic crystal. Essentially, the spontaneous emission rate modification was estimated using an essentially two-dimensional approximation. Clearly, accurate modeling of the spontaneous emission rate must take into account the fully three-dimensional nature of the problem. A more precise evaluation requires a self-consistent analysis that takes into account the interaction between the light source and the photonic bands as well as finite size of the crystal in the third dimension. Photonic bandgap materials can completely suppress spontaneous emission within the gap region [7]. However, the radiation dynamics depend on the local density of states within the region containing radiating species rather than the total free space density of states outside the crystal. In essence, the spatial alignment between the optical states and the radiating species must be taken into account. Typically, Purcell enhancement factors are calculated assuming that the radiating species is spatially located at the maximum field point (see for example [99]). For the case of a microcavity, this may be a good approximation since the microcavity localizes the field to a small volume where the radiating species is located. However, using the spatial alignment of the modes with the radiators provides a means to completely control the radiation (inhibited or enhanced) within a finite photonic structure [107], which, being finite, cannot have a complete bandgap.

A finite-difference time-domain method for direct calculation of the spontaneous emission rate in an arbitrary dielectric structure has been proposed and demonstrated [20]. This method depends on the correlation between the fully quantum mechanical spontaneous emission rate calculation and a classically radiating dipole as described in section 2.3 and in [108]. Recently, Hwang et al. [109] have independently developed similar calculations of spontaneous emission rate in various photonic crystal structures using a similar finite-difference time-domain method. Although this method is generally useful in being able to deal with arbitrary structures and inherently includes all localized, guided, and extended modes, careful consideration must be given to the position dependence of the emission rate on the dipole source location. It is clear that the choice of regions for the calculation of the local density of states can have a significant effect on the resulting calculated radiation rate due to the non-uniform spatial distribution of the photonic crystal band modes [44]. Therefore, the single point dipole method used by Hwang et al. [109] to calculate the spontaneous emis-

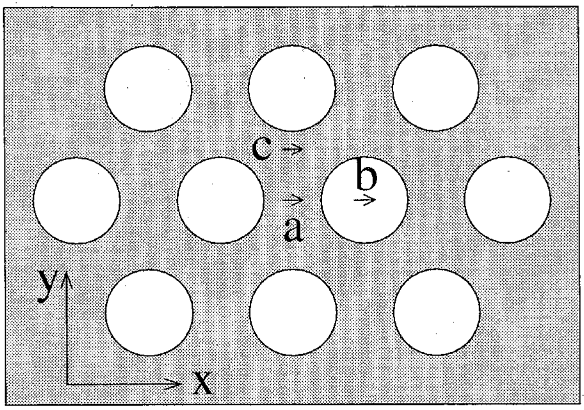

Figure 6.2: Schematic indicating the calculated dipole locations in the triangular lattice. Points "a" and "c" are high symmetry points in the dielectric region (dielectric-like). Point "b" is a high symmetry air-like point.

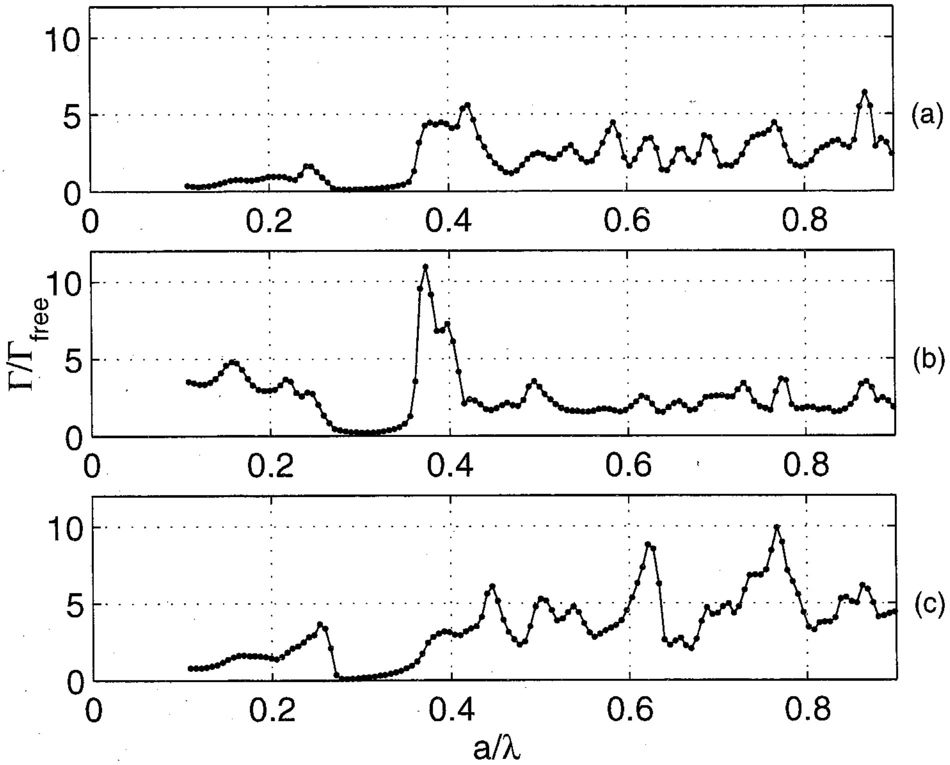

Figure 6.3: Position dependence of the spontaneous emission rate using a single point dipole at different locations in the photonic crystal structure. Spontaneous emission rate spectrum relative to the free space rate for the different dipole locations corresponding to Fig. 6.2

sion rate will depend on the choice of dipole position. To overcome this difficulty, an average over possible dipole positions is necessary to determine the spontaneous emission properties of the structure as a whole.

Fig. 6.3 shows an example of single dipole calculated spontaneous emission rates at various dipole positions for a triangular lattice of holes with $r/a = 0.32$ in a slab with thickness $d/a = 0.375$. Fig. 6.2 shows a schematic of the structure with three dipole locations indicated which correspond to the three spectra shown in Fig. 6.3. As expected, the emission rate spectrum can clearly be changed dramatically by the choice of dipole position within the photonic lattice. In all three cases, the bandgap region can be seen approximately in the frequency range 0.27 to 0.36. The strong coupling to the upper band edge seen in Fig. 6.3b demonstrates the nature of this band, which is spatially located primarily in the air regions [44] where the dipole (Fig. 6.2) is located (hence the terminology "air band"). Fig. 6.3 shows that the structure could exhibit strongly ($> 10\times$) enhancement of the spontaneous emission rate at certain frequencies, however, the radiator location must be considered. For example, Fig. 6.3a shows no peaks above $5\times$ enhancement.

It has been shown previously in section 2.3 and in [20, 108, 21] that the classical dipole radiation power in a finite-difference time-domain calculation can be used to determine the quantum mechanical spontaneous lifetime as

$$\left[\frac{P^{cav}}{P^{vac}}\right]_{quantum} = \left[\frac{P^{cav}}{P^{vac}}\right]_{classical} = \frac{\tau_{vac}}{\tau_{cav}}$$

where "*cav*" denotes values for the cavity structure and "*vac*" denotes values calculated for a vacuum. We use a fully vectorial three-dimensional calculation with a perfectly matched layer (PML) absorbing boundary conditions [52] to directly solve the vector Maxwell's equations (Eq. (2.27)). A large number of point dipoles (typically 1000 - 6000 dipoles were used) with random polarization, Lorentzian lineshape and Poisson distributed in time are used as radiation sources in order to average out dependencies on polarization and position within the lattice. Only dipoles polarized in the plane of the slab are considered since this corresponds to emission from semi-

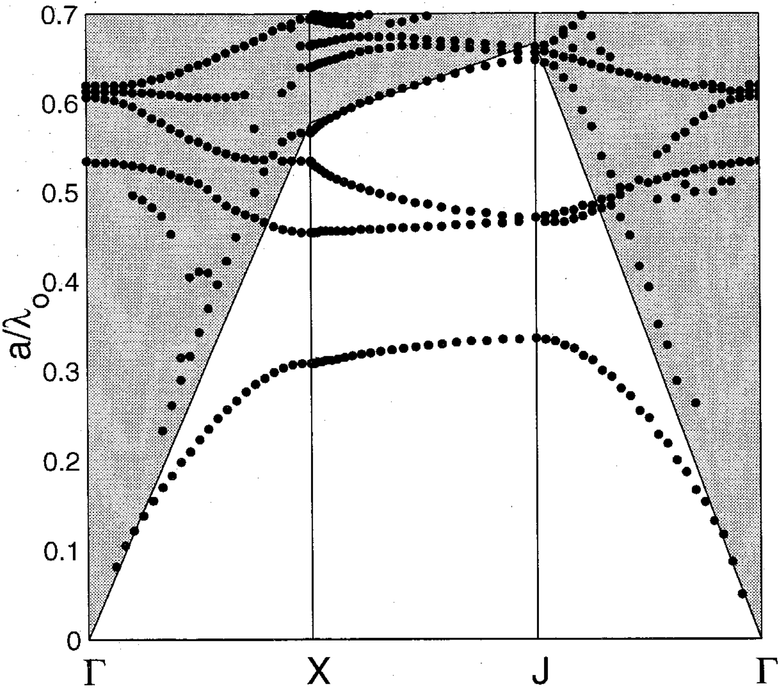

Figure 6.4: Calculated in-plane bandstructure with $d/a = 0.33$ and $r/a = 0.35$ for TE-like modes. The shaded region corresponds to the unguided (extended) modes.

conductor quantum wells (primarily TE-like). The dipole sources are also limited to the regions of high dielectric constant so that there are no radiation sources in the air regions. The single dipole calculations used broadband Gaussian pulse excitation analyzed by discrete Fourier transformation, which has been shown to be more computationally efficient in an FDTD algorithm [50] than the fast Fourier transform. The multiple dipole-averaged simulations used narrow band Lorentzian lineshape dipoles and the total time-averaged power flow. This is equivalent to averaging the frequency response over the dipole homogeneous linewidth modeled as the Lorentzian linewidth of the dipole sources.

Due to computational time restrictions, a small 6 × 6 photonic crystal unit cell domain was used. For comparison, an 8 × 8 cell domain was calculated and these results were not qualitatively different from the smaller calculations. The structure studied here is shown schematically in Fig. 6.1. We define the extraction efficiency, η_{ext}, as the ratio of power through the top surface of the computational domain (+z) to the total power. We also introduce a detection efficiency, η_{det}, to characterize the power, which might be practically collected normal to the slab. This is defined as the power emitted through a square surface parallel to the slab where the sides of the square subtend a half-angle of $\sim 52°$ (a collection cone with this half-angle corresponds to a numerical aperture of $NA \approx 0.8$).

6.2.2 Fixed d/a structure

We first consider a photonic crystal slab structure with fixed waveguide thickness to lattice parameter ratio d/a. This is the case that is normally considered experimentally, for example, in reference [99]. Since dimensions in Maxwell's equations are scalable [44], this is the computationally simplest case since the structure geometric parameters have constant relative sizes. The bandstructure for in-plane wavevectors for a structure with a slab thickness of d/a = 0.33 and hole radii of r/a = 0.35, is shown in Fig. 6.4 using a finite-difference time-domain method similar to that of Painter et al. [27]. Fig. Fig. 6.5 shows the corresponding spontaneous emission calculation results. The left plot shows the spontaneous emission rate (Γ_{sp}) relative to the value in free space. At low frequencies ($a/\lambda < 0.2$), the spontaneous emission rate is similar to the free-space value ($\Gamma_{sp}/\Gamma_0 \sim 1$). Since the wavelength is much larger than the lattice spacing, an effective index approximation can be used, which implies that the emission rate will scale roughly as the effective index. This means that the effective medium for emitters is approximately the spatial average of the index of refraction. Since the membrane is thin and relatively porous on a scale much smaller than the wavelength, this spatial average will be close to the index of refraction for air ($n_{air} = 1$). The emission rate within the in-plane band gap ($a/\lambda \approx 0.3 - 0.4$) shows a suppression by up to 3 times. Note that this inhibition may be limited by the small size of the calculation (6 lattice period domain). Above the upper band edge, there is a strong enhancement of the emission rate up to 8 times the free space rate, corresponding to emission into the photonic conduction bands. Broad peaks in the spontaneous emission rate in the frequency range $0.42 - 0.57$ and centered

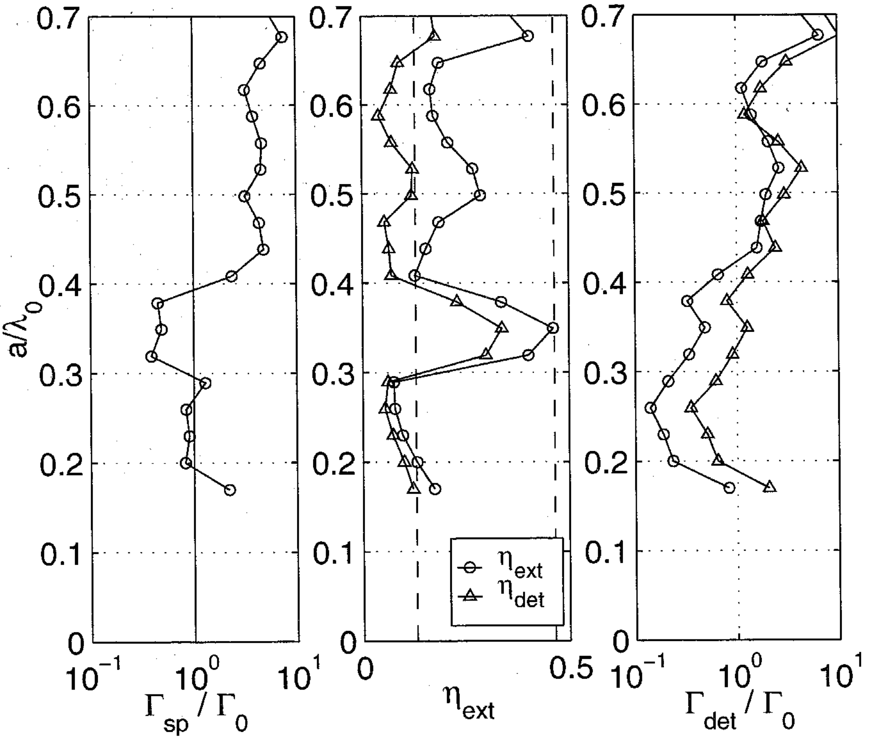

Figure 6.5: Spontaneous emission from a photonic crystal slab with d/a constant. *Left* - spontaneous emission rate normalized to the free space rate (logarithmic scale). *Center* - extraction (o) and detection ($\triangle$) efficiencies as defined in the text. The values for an unpatterned slab are indicated by the dotted lines. *Right* - Detection ($\triangle$) and extraction (o) rates (logarithmic scale) from a photonic crystal slab normalized to the rate for free space.

around 0.65 correspond respectively to the first two guided modes of the conduction band in Fig. 6.4 and the band that lies just below the light line in the **XJ** direction in Fig. 6.4. Compared with the single dipole cases shown in Fig. 6.3, the enhanced emission into the conduction bands exhibits a broad and relatively uniform enhancement over all conduction band frequencies shown in Fig. 6.5. This demonstrates the spatial averaging effect in the local density of states when all possible lattice positions are considered.

The extraction and detection efficiencies η_{ext} and η_{det} are shown in Fig. 6.5 (center). The total extraction efficiency rises to nearly 50% (complete extraction since the extraction efficiency was defined in only the positive z-direction) in the bandgap region along with an increase in the detection efficiency ($\sim$ 41%). This agrees quite well with the results of Fan et al. [77] and is attributed to the photonic crystal inhibiting guided modes within the slab. The relatively high detection efficiency indicates that the vertical emission is primarily in the normal direction as opposed to at acute angles with the slab plane. However, for frequencies above the band edge, both the extraction and detection efficiencies are significantly lower (at approximately a/$\lambda = 0.5$, $\eta = 25\%$ and 10% respectively). An increase in the extraction efficiency also occurs for frequencies above ~ 0.65 corresponding to crossing the light line to the unguided modes.

Although there are regions of nearly complete light extraction (e.g., within the bandgap region), in practice, this is not necessarily useful because of the greatly reduced emission rate at these frequencies. In a medium with finite non-radiative decay processes, the reduced emission rate can result in a corresponding reduction in the internal quantum (radiative) efficiency ($\eta_{rad} = \Gamma_{rad}/\left(\Gamma_{rad} + \Gamma_{nr}\right)$). If, for example a material has a $\eta_{rad} = 90\%$ in bulk form, the 3× reduction in the spontaneous emission rate results in η_{rad} being reduced to about 75% assuming a fixed non-radiative rate. The loss of radiative efficiency increases rapidly with decreasing spontaneous emission rate as well as with decreasing unmodified efficiency as shown in Fig. 6.6. A better comparison may be made by considering the emission rate through a surface of interest, the "*extraction rate*" Γ_{ext} for the infinite x-y plane in the +z direction or the "*detection rate*" Γ_{det} for the previously defined detection surface. This is shown in Fig. 6.5 (right) normalized to the corresponding rates for free space. The extraction and detection rate curves are very similar owing to the similarity in η_{ext} and η_{det}. Above the bandgap, the emission rate is enhanced enough to compensate for the lower extraction efficiency resulting in an up to $\sim 10\times$ enhancement of Γ_{ext} and Γ_{det} at $a/\lambda \sim 0.53$ and at $a/\lambda \sim 0.68$. In the bandgap frequency region and below, the extraction rate is much smaller than the free space rate. In the bandgap region, although the η_{ext} is high, the corresponding emission rate Γ_{sp} is low. The extraction rate at the bandgap center ($a/\lambda \sim 0.35$) shows that nearly perfect extraction efficiency is balanced by the inhibited emission rate such that the extraction rate remains nearly equal to the value calculated for free space radiation.

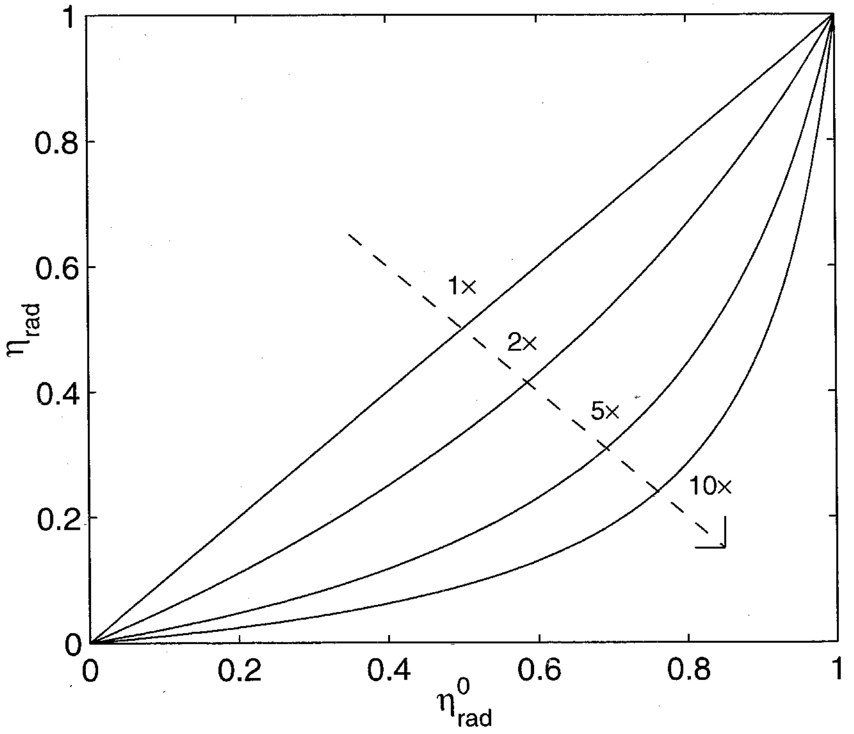

Figure 6.6: Effective radiative efficiency η_{rad} versus original bulk radiative efficiency η^0_{rad} for different inhibition factors (indicated in the figure) showing a rapid drop in efficiency when the radiation is inhibited.

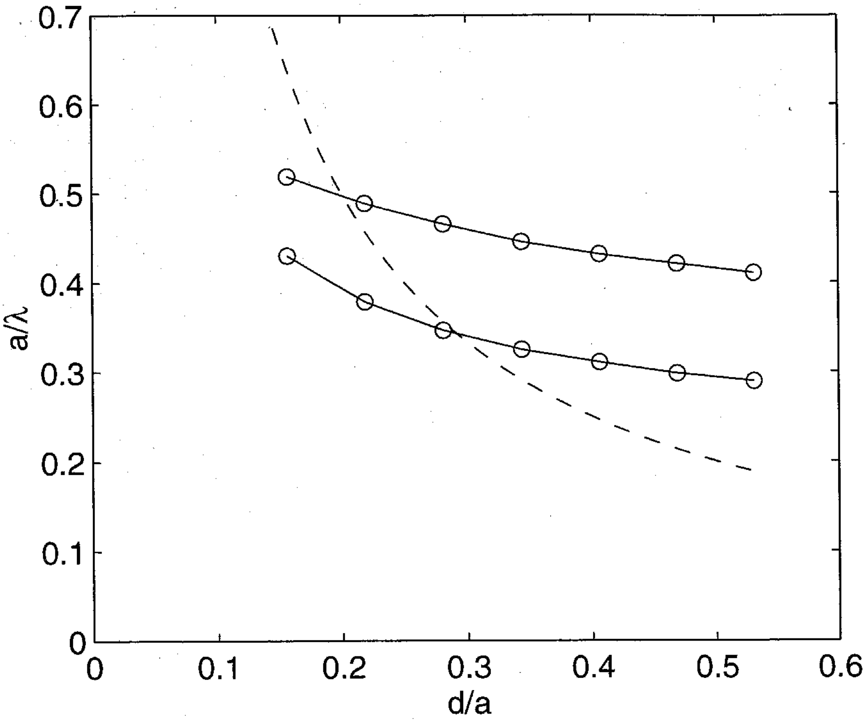

Figure 6.7: Variation in band-edge frequencies as a function of waveguide thickness d/a for a triangular lattice of holes with for constant $r/a = 0.35$ calculated using a three dimensional finite-difference time-domain method. The solid lines and circles are the calculated band edges. The dashed line represents the line of constant wavelength with $d/\lambda = 0.1$

6.2.3 Fixed d/λ structure

A structure consisting of a slab of photonic crystal in which the emission wavelength (λ) and slab thickness (d) are fixed and the lattice spacing (a) is varied is of interest due to the ease with which the lattice spacing can be easily varied lithographically [89] to tune the photonic crystal response. In this case for increasing normalized frequency (a/λ), the waveguide thickness d/a decreases. This results in a shift of the bandgap towards higher frequencies [27] as shown in Fig. 6.7. Since experimental measurements [85, 99, 110] are typically under conditions of constant thickness (d/λ) the calculations [77, 109] for constant d/a from the previous section cannot be directly compared. The emission rate, extraction and detection efficiencies, and the detection rate for the constant d/λ thickness are shown in Fig. 6.8. In this case the emission rates have been normalized to the corresponding slab waveguide rate instead of the free space rate. The strong suppression of the spontaneous emission rate by approximately 10× in the bandgap frequency range is again seen with the corresponding sharp increase in both the extraction and detection efficiencies such that nearly all emitted photons are extracted normal to the slab. However, above the bandgap region, there is no dramatic enhancement of Γ_{sp} and for $a/\lambda > 0.5$, Γ_{sp} is in fact inhibited by approximately 2×. Since the waveguide to wavelength ratio (d/λ) is fixed, the aforementioned bandgap shift upwards in frequency results in the conduction bands moving towards the light line. The vertical field confinement is thereby reduced, decreasing the enhancement of Γ_{sp} (Fig. 6.8 left). Also, the reduced vertical confinement by the slab index guiding result in a slightly higher extraction and detection efficiency into the conduction bands (Fig. 6.8 (center) $\sim 40\%$ and $\sim 15\%$ versus 25% and 10% in the previous case). In this case, although the extraction efficiency into the conduction bands is relatively high, the corresponding detection efficiency is approximately the same at the infinite slab efficiency. This implies that in the conduction bands, the radiation that is extracted in the half-plane (+z direction) occurs primarily at acute angles with the slab plane. Therefore, this emission cannot be usefully collected from the slab-normal direction (detection efficiency).

The extraction rate for d/λ fixed is shown in Fig. 6.8 (right). Below the upper band edge, Γ_{ext} remains similar to the slab extraction rate. This suggests that the inhibition that occurs within the bandgap is mostly due to the fraction of solid angle affected by the photonic structure. This is not surprising since away from the band edge, the lower band in Fig. 6.4 is only slightly modified from the infinite slab dispersion (represented by the light line). Γ_{ext} is directly related to the coupling of the dipoles to the unguided radiation modes so that the inhibition of guided modes does not strongly affect the extraction rate. Above the bandgap, there is a combination of enhanced extraction efficiency and only slight inhibition of Γ_{sp} resulting in a $\sim 5\times$ enhancement of the extraction rate. For a medium with non-radiative decay, similar behavior would be expected from a measurement of emitted power with increased power output above the upper band edge in the +z direction. Previously, sponta-

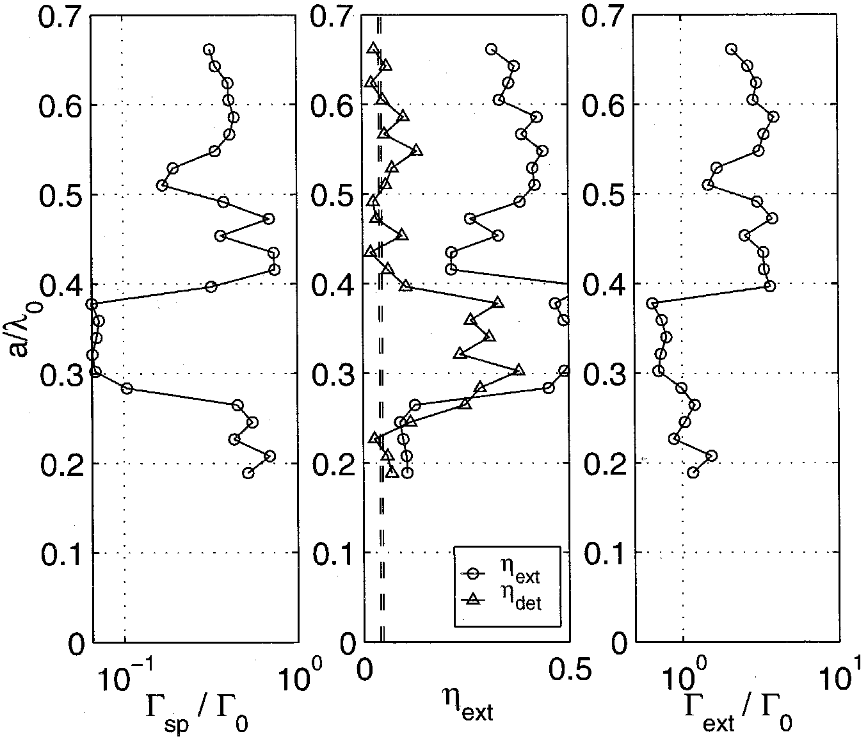

Figure 6.8: Power extraction from a photonic crystal slab with d/λ constant. *Left* - spontaneous emission rate (logarithmic scale) normalized to the value in a slab waveguide. *Center* - extraction ($\circ$) and detection ($\triangle$) efficiencies. The corresponding values for an unpatterned slab are indicated by dotted lines. *Right* - Extraction rate (logarithmic scale) from a photonic crystal slab normalized to the rate for an unpatterned slab with the same thickness d/λ.

neous emission power measurements from similar triangular lattice photonic crystal slabs have been presented [85, 99] that showed strongly enhanced power extraction ($\sim 10\times$) above the upper band edge. This qualitative behavior for a triangular lattice of air holes corresponds well with Fig. 6.8 (right), which shows a large power enhancement for frequencies above the bandgap over those below or within the gap region. Strong enhancement of the extraction efficiency from a hexagonal lattice of semiconductor microcolumns has also been observed by Baba et al. [110] but without a corresponding enhancement of the power extraction. For this geometry, there was no measurable change in the spontaneous lifetime [110]. However, the power extraction in the presence of non-radiative recombination mechanisms depends on both the spontaneous emission rate as well as the extraction efficiency. A detailed discussion of power extraction and lifetime measurements in a photonic crystal slab structure is given in chapter 7.

6.3 The triangular lattice of air holes

6.3.1 Local density of states maps

From the calculation for the enhanced spontaneous emission rate for single point dipoles and for the case of constant geometrical parameters (d/a constant), there are clearly points where the spontaneous emission experiences strong enhancement. The case calculated for constant slab thickness (d/λ constant) showed no enhancement of the spontaneous emission rate at any frequency below the light line. However, for inhibition of the spontaneous emission rate, the constant geometry structure showed only weak inhibition ($3\times$), whereas much stronger inhibition was seen for the constant thickness structure ($10\times$). In order to optimize these parameters, it is necessary to examine the variation in the local density of states (for slab confined modes) over a wide range of parameters. The enhancement of the spontaneous emission rate is proportional to the local density of states. Henceforth, the enhancement of the spontaneous emission rate and the enhancement of the local density of states will be used interchangeably for the purposes of these results.

Fig. 6.9 shows a two-dimensional map of the local density of states (LDOS) for the photonic crystal slab structure with constant geometry and a slab thickness d/a = 0.33 normalized to the free space value. They resemble the bandgap maps commonly used to show the bandgap position versus parameter space [44]. However, additional information in the form of the local density of states is represented by the map color (blue for low density to red for high density). These figures were calculated using the multiple dipole three-dimensional FDTD algorithm. In these calculations 3860 dipoles were used, distributed throughout one photonic crystal unit cell, Poisson distributed in time with Gaussian lineshapes. A Gaussian instead of Lorentzian lineshape was used because of discretization error in the time domain. The rapid variation on the leading edge of the Lorentzian time pulse requires a smaller time discretization for convergence than the more gradual variation in a Gaussian pulse. The randomly located dipoles were distributed throughout the photonic crystal unit cell (including in the air regions) to give the total slab-localized density of states (the previous section showed slab and high-index localized density of states).

The top figure in Fig. 6.9 shows the reduced density of states region corresponding to the in-plane bandgap with a maximum bandgap width at approximately r/a = 0.38. Maximum points in the LDOS occur near this point along the upper band gap edge. However, from the single dipole emission in Fig. 6.3, it is known that the upper band edge points are primarily coupled to the air regions. No significant change in the LDOS within the bandgap is visible in this figure except for r/a > 0.4 where the LDOS can be seen to gradually rise such that at r/a = 0.5 the LDOS is essentially uniform for all frequencies (remembering that this is normalized to the free space DOS). An enhanced view of LDOS is shown in the lower figure in Fig. 6.9. This shows that there are other enhanced emission points in the LDOS map that are in the range of 4× to 7× larger than the free-space value. At r/a ~ 0.38, peaks up to approximately 6× in the LDOS are visible on the lower band edge. In the parameter range r/a ~ 0.2 to 0.3, several ~ 6× enhanced bands are visible in the conduction band region. This shows that this structure is capable of significant enhancement

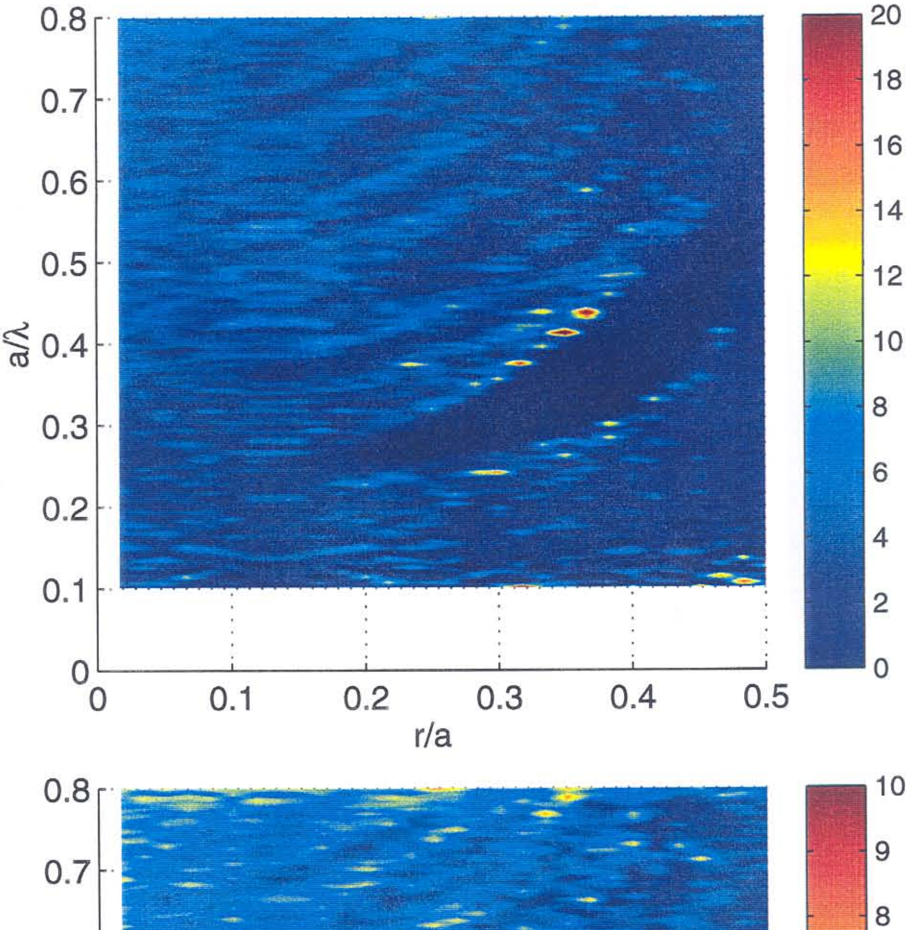

Figure 6.9: Slab-localized density of states with thickness $d/a = 0.353$. Lower plot is a scaled version of the upper plot to show the density of states band structure.

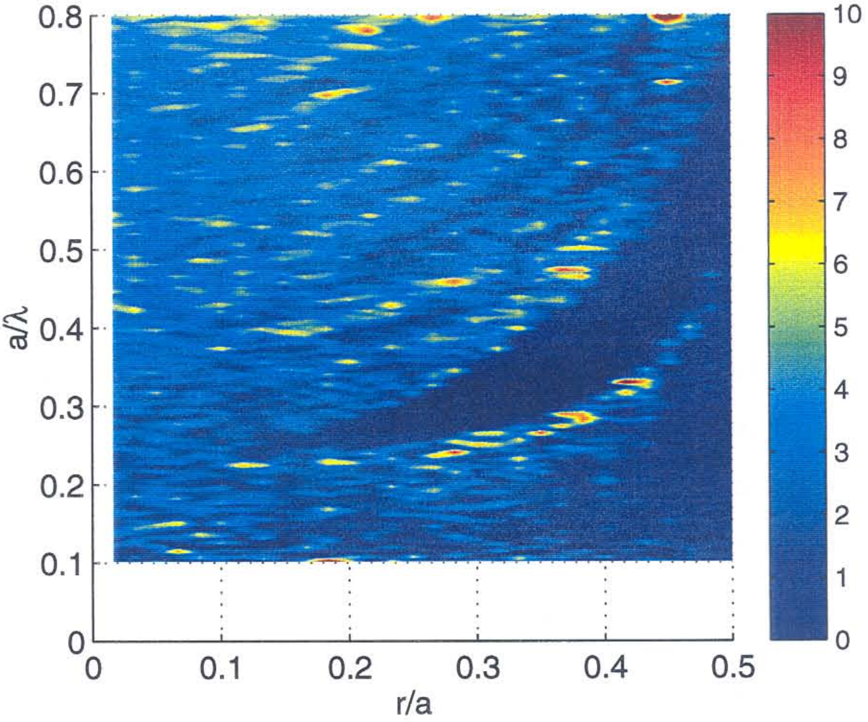

Figure 6.10: Slab-localized DOS with dipoles located only in high dielectric regions.

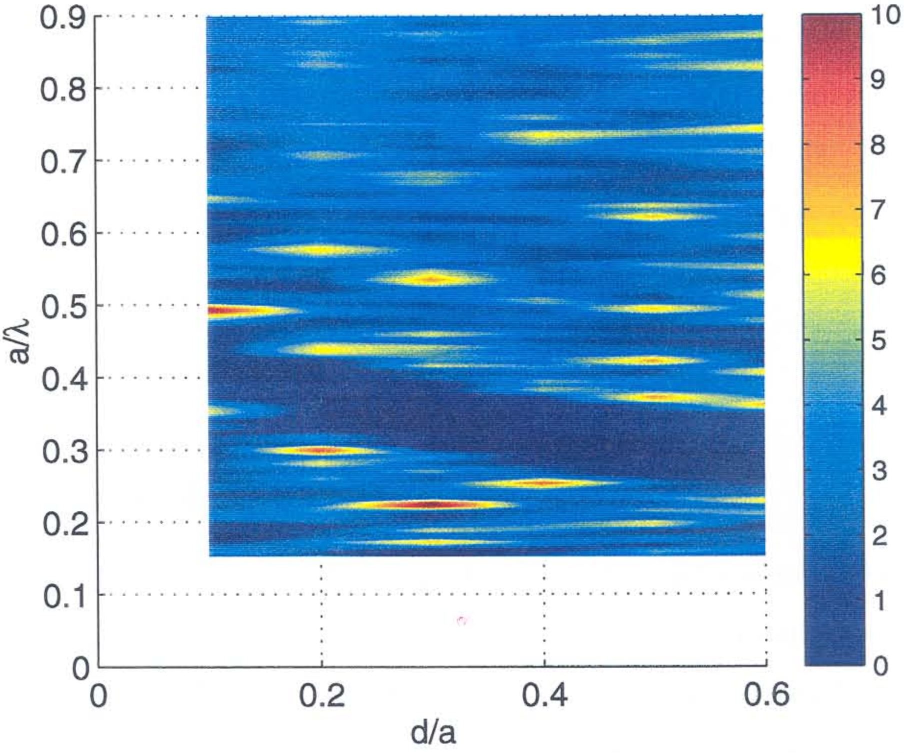

Figure 6.11: Slab-localized density of states versus slab thickness for $r/a = 0.32$

of the spontaneous emission rate even for structure which do not show an in-plane bandgap.

The localized density of states for the same structure as that shown in Fig. 6.9 is shown in Fig. 6.10 where the dipole sources have been restricted to the high dielectric regions. This is a more realistic case for emission from this type of structure and highlights the dielectric-coupled bands in the LDOS band map. A comparison of the total slab-localized DOS (Fig. 6.9 lower figure) and the slab and dielectric localized DOS (Fig. 6.10) shows that the some higher lying photonic conduction bands that showed LDOS peaks also show strong enhancement ($> 10\times$) when the dipoles are confined to the high dielectric regions. Clearly the upper band edge shows very weak enhancement of the density of states since these are known to be primarily located in the air regions. However, there are still enhanced peaks by greater than an order of magnitude, particularly at r/a $\approx$ 0.4 (a/$\lambda \approx$ 0.47) and at r/a $\approx$ 0.29 (a/$\lambda \approx$ 0.46).

The variation of the LDOS with slab thickness for fixed r/a = 0.32 is shown in Fig. 6.11. It is important to note that due to discretization of the structure, only 6 evenly space values of d/a were calculated. This means any structure in the LDOS narrower than $\Delta(d/a) \sim 0.1$ similar to the infinite slab enhanced emission structure shown in Fig. 2.3 may not appear. Fig. 6.11 clearly shows that the slab thickness primarily results in a shift of the in-plane bandgap to lower frequencies. However, there does not appear to be any significant change in the LDOS and therefore slab thickness appears to play only a small role in the enhancement or inhibition of the spontaneous emission rate.

6.3.2 Electric field distributions

The spatial distribution of the electric field magnitude can be critical since enhancement of modes primarily located in the air regions may not be useful since in practice, radiating species are located in the higher dielectric constant material. The field distributions at different frequencies for the structure discussed in the previous section are shown in Fig. 6.12 for r/a = 0.32 and a waveguide thickness of d/a = 0.353.

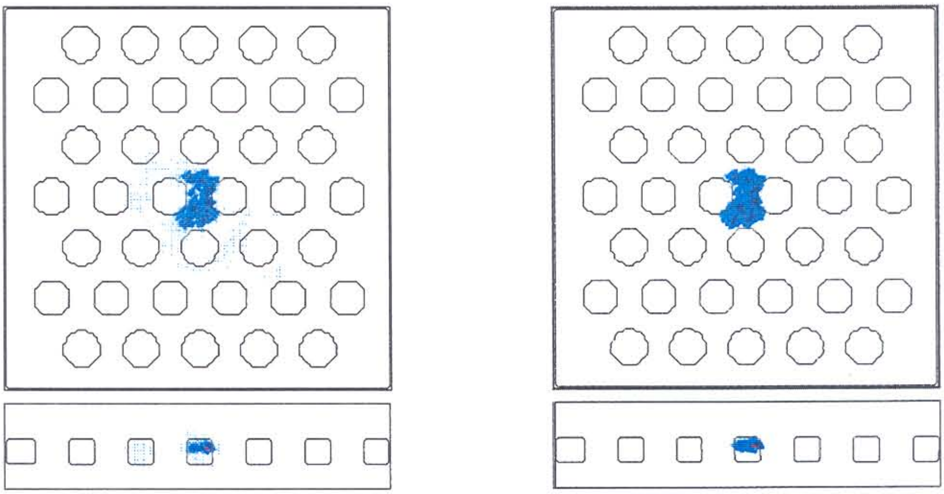

(a) $a/\lambda = 0.259$ lower band edge

(b) $a/\lambda = 0.30$ mid gap

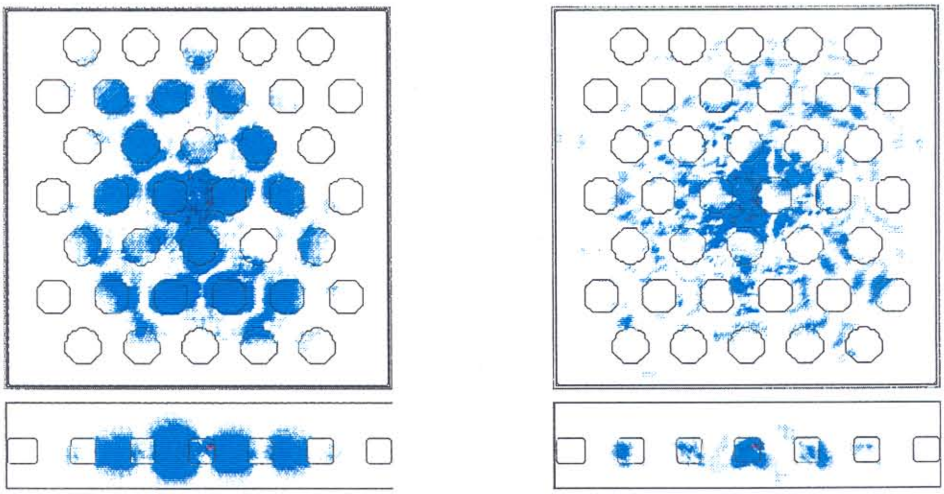

(c) $a/\lambda = 0.37$ upper band edge

(d) $a/\lambda = 0.62$ near (below) light line

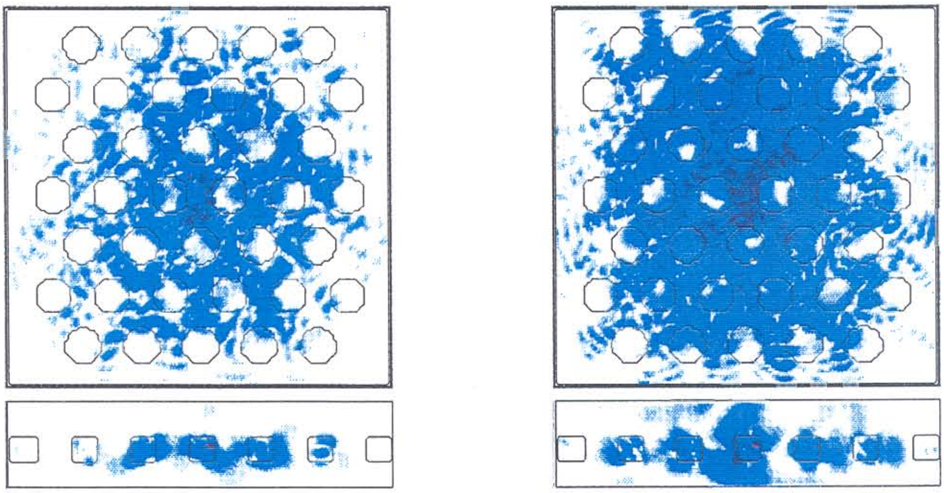

(e) $a/\lambda = 0.80$ near (above) light line

(f) $a/\lambda = 0.97$ above light line

Figure 6.12: Electric field distribution cross-sections in the x-y plane and the y-z plane at six different frequency points for the triangular lattice slab under excitation from multiple random dipoles.

Since these have been calculated using multiple random dipoles as sources, these do not represent individual modes since the field wavevector is not specified. However, some general behaviour at particular frequencies is visible. In Fig. 6.12b the dipole frequency lies approximately in the middle of the bandgap region and the field distribution is localized to the dipole source positions with no radiation in the plane of the slab. In Fig. 6.12a, slightly below the gap, the field radiates slightly into the photonic crystal. The frequency at the upper band edge shown in Fig. 6.12c clearly shows that, as previously mentioned, this band is primarily located in the air regions. It should be noted that the dipole sources in this calculation are confined to the dielectric regions. Fig. 6.12d-f show various points in the photonic conduction band in which the radiation penetrates well into the photonic crystal.

6.3.3 Size of the photonic crystal lattice

It was previously mentioned that the size of the computational domain did not result in any qualitative changes in the calculated modified spontaneous emission spectra. The LDOS spectra for computational domains with 2n layers of photonic crystal in each direction (x and y) is shown in Fig. 6.13 for n = 2 to 6. Although the spectrum is relatively complicated with many peaks in the conduction band region ($a/\lambda > 0.37$, it can be seen that most of the features in the spectrum occur for all calculated domain sizes. This implies that the band formation occurs relatively quickly such that for all computational domains considered here, the smallest being $\sim 4\times$ PBG unit cells, the qualitative behaviour of the LDOS is essentially unchanged. This allows the use of relatively small domains for these calculations without suffering significant changes in the behaviour due to the finiteness of the calculation. It should also be noted that the low-density of states band corresponding to the bandgap frequency region is well established even for small crystals with only 4×4 unit cells (indicated as 2 layers in Fig. 6.13).

Fig. 6.14 shows an expanded view of the LDOS dependence on the number of PBG layers for the bandgap region, which shows some notable features dependent on the PBG crystal size. The first thing of note is the shift in the lower band edge as the number of PBG layers is increased. The band edge transition from high to low density of states becomes steeper as the number of layers is increased. However, the shift in the band edge is relatively small and is likely insignificant compared to the discretization error of the structure. The more significant change as a function of crystal size occurs within the bandgap region. Clearly in Fig. 6.14, the "depth" of the gap increases significantly as the PBG crystal size is increased. From 2 layers up to 6 layers, the inhibition factor Γ_{sp}/Γ decreases by approximately one order of magnitude at the low frequency end of the bandgap ($a/\lambda \sim 0.2-0.29$). This corresponds well with defect cavity Q calculations [27], which have shown that the Q increases exponentially up to 7 layers of photonic crystal. The bandgap depth at the high frequency end of the gap region does not show as dramatic a change with crystal size and is also inhibited significantly less, by nearly 2 orders of magnitude for large numbers of layers. This occurs because the higher frequency points in the bandstructure in Fig. 6.4 occur closer to the light line implying lower confinement within the slab. Alternatively, at higher frequencies, a smaller portion of the Brillouin zone is contained below the light line resulting in a smaller fraction of 4π steradians, which is inhibited by the in-plane bandgap.

6.4 Modified square lattice

Although the triangular lattice of air holes has been the primary structure of interest in these calculations, other lattices must also be considered. In terms of inhibited spontaneous emission, it is likely that the triangular lattice of air holes may be a good choice since it exhibits the largest bandgap for TE-like modes among several symmetry choices [44]. However, Fig. 6.9 shows that enhanced emission points can occur without the presence of a bandgap due to the distributed band states of the photonic crystal. We consider here the modified-symmetry square lattice as a possible example.

The modification of the spontaneous emission rate due to the local properties of

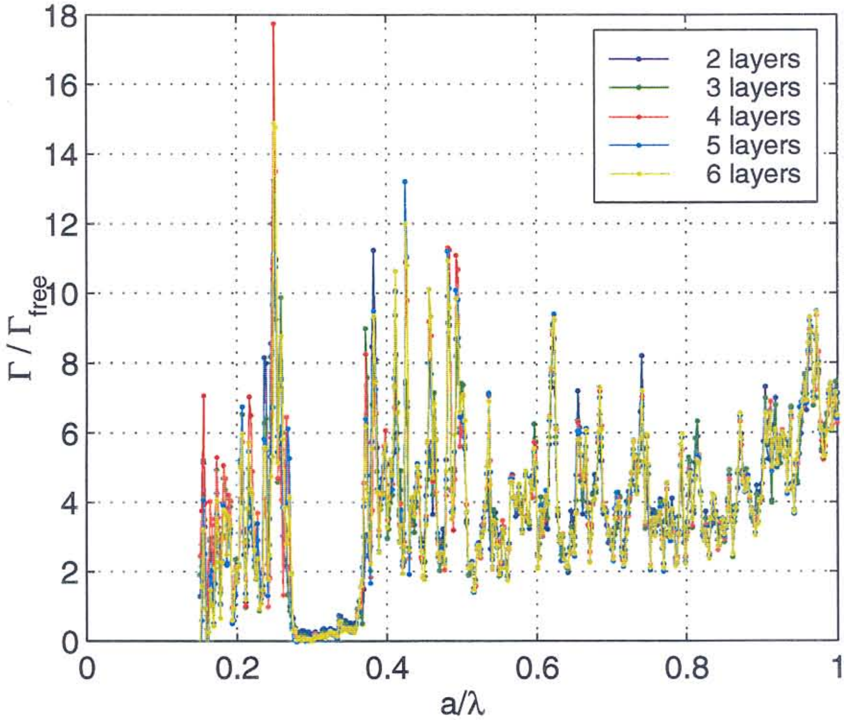

Figure 6.13: Slab-localized DOS dependence on the number of PBG layers with $r/a = 0.32$ and $d/a = 0.353$.

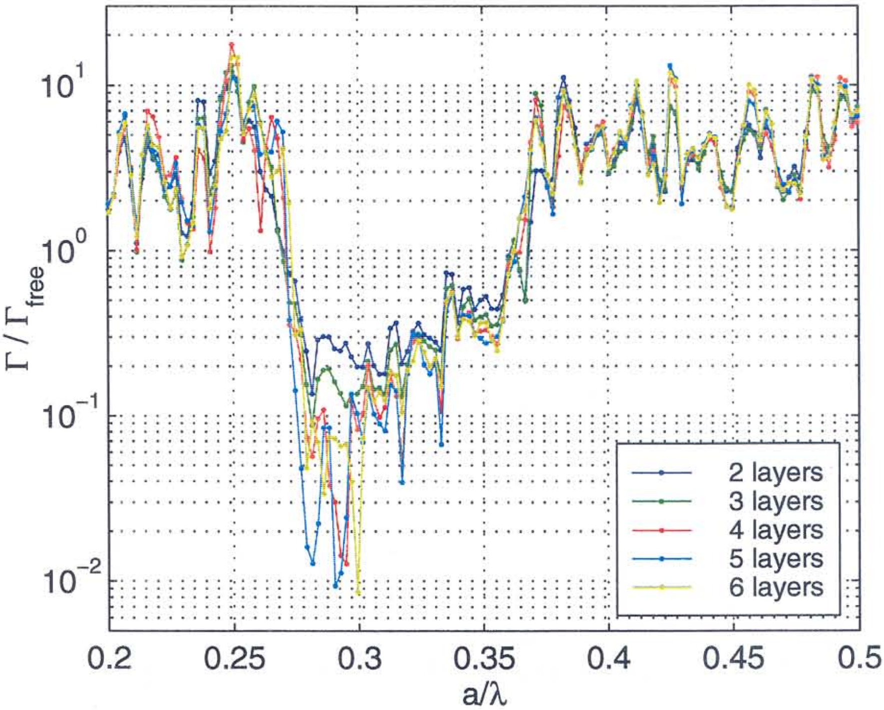

Figure 6.14: Expanded view of the LDOS in Fig. 6.13 versus number of PBG layers.

the field modes at the position of the emitter has been shown to obey a sum rule [111, 112] such that the transverse field emission rates with transition frequency ω_a satisfy

$$\int_0^\infty d\omega_a \frac{\Gamma_m(\vec{r},\omega_a) - \Gamma_0(\omega_a)}{\Gamma_0(\omega_a)} = 0 \tag{6.1}$$

where $\Gamma_0(\omega_a)$ is the spontaneous emission rate in free space and $\Gamma_m(\vec{r},\omega_a)$ is the emission rate at position $\vec{r}$ as modified by the local electromagnetic environment. This sum rule assumes that the size of the emitter is negligible and that the dielectric function conforms to the typical causality and asymptotic requirements (e.g., a perfect reflector for all frequencies will violate this sum rule but is also non-physical). This leads to the simple rule of thumb that any reduction or inhibition of the spontaneous emission rate over some range of frequencies ω_a must be accompanied by an associated increase over some other range or ranges of frequencies.

It is well known [58, 59, 60, 61] that for an emitter embedded in a dielectric host, the emission rate is scaled by the real part of the refractive index. Therefore using the sum rule of Eq. (6.1), we conclude that to find structures that show the strongest enhancement of the emission rate, we should focus our attention on materials with large real parts of their refractive indices and photonic structures with large bandgaps. Symmetry reduction [113, 114] through the introduction of a two-point basis set has been shown to be effective producing larger photonic band gaps in two-dimensional crystals. A two-point basis set has also been used to reduce the face-centered-cubic three-dimensional symmetry to a diamond structure to obtain a full three-dimensional photonic bandgap [45].

An example of symmetry reduction is shown schematically in Fig. 6.15 which shows a two-dimensional square lattice of air holes of radius r, with added holes with a different radius r′. This is referred to as the reduced-symmetry square lattice [113]. In a normal square lattice of air holes with a slab index of n = 3.4 and r/a = 0.45, the infinite two-dimensional photonic crystal has only a narrow bandgap for TE modes [44, 113]. Therefore, we would expect that a finite thin slab square lattice

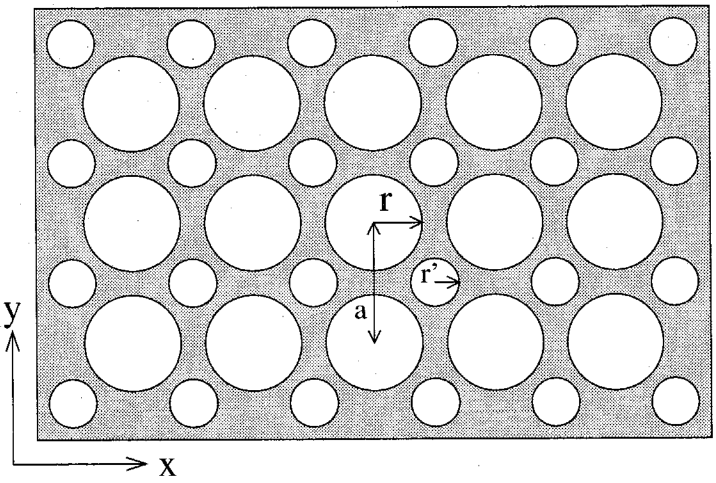

Figure 6.15: Schematic drawing of a reduced-symmetry square lattice photonic crystal.

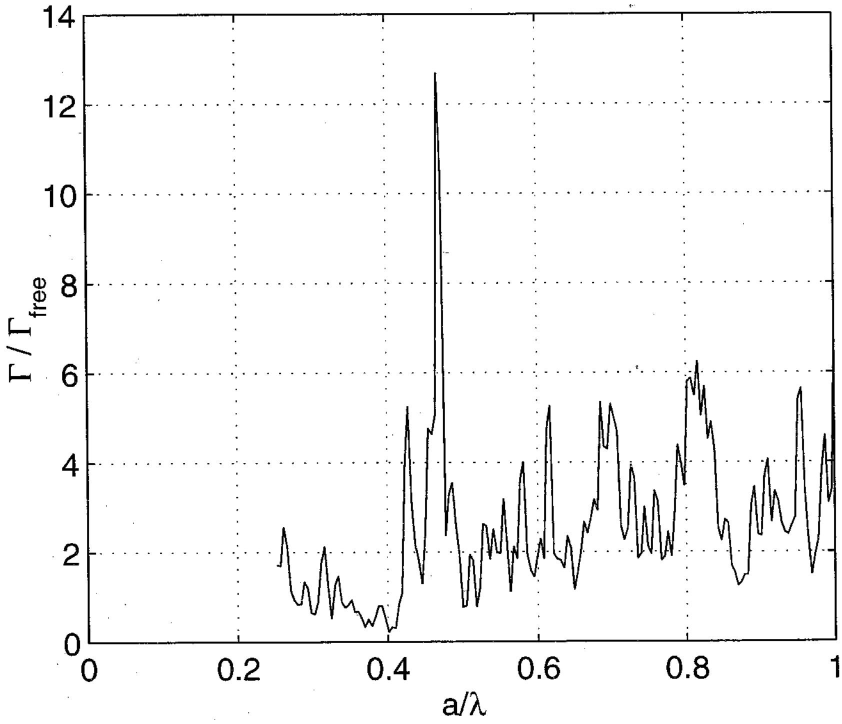

Figure 6.16: Slab-localized density of states for the reduced-symmetry square lattice for secondary hole radii r′ = 0.30 and r/a = 0.45.

photonic crystal would have no in-plane bandgap for TE modes due to the effectively reduced index contrast. The reduced-symmetry square lattice has been shown to have expanded gaps [114]. The calculated spontaneous emission rate enhancements for the reduced-symmetry square lattice with r/a = 0.45 and secondary hole radius r′ = 0.30, is shown in Fig. 6.16. This shows an example of a structure with no apparent bandgap but which exhibits points with relatively large enhancements.

6.5 Summary

The results in this chapter have shown that the spontaneous emission rate in the two-dimensional photonic bandgap slab structure can be suppressed by greater than an order of magnitude even without optimizing the device design. This occurs in spite of the fact that this structure does not exhibit a complete bandgap and is due to the coupling of the modes with the dipole source position in space. We have shown that a two-dimensional triangular lattice photonic bandgap structure in a thin slab can strongly suppress or enhance the spontaneous emission rate by about one order of magnitude even though this structure lacks a complete three-dimensional band gap. The large enhancement rates at the band edges predicted in single dipole calculations are strongly dependent on the choice of dipole position so that spatial averaging is necessary to estimate the general emission properties of the photonic structure as a whole. The bandgap structure can also be used to enhance the vertical extraction efficiency. Emission into the conduction bands can be enhanced while still maintaining relatively large extraction efficiency. In the presence of non-radiative processes, this could result in a structure with enhanced internal and external quantum efficiencies.

Chapter 7 Measurement of modified spontaneous emission

7.1 Introduction

Photonic crystals have long been suggested as a system that should exhibit strongly modified spontaneous emission; however, measurements in the optical regime have mostly been limited to low-index contrast structures that do not have a complete bandgap. Although the two-dimensional photonic crystal slab also does not have a complete bandgap, calculations (see chapter 6 and reference [91]) have shown that very strong inhibition, greater than one order of magnitude may be possible because the high index contrast and strong vertical confinement due to total internal reflection extends the bandgap over a significant portion of 4π steradians. Enhanced spontaneous emission may also be possible from the distributed states of the photonic crystal without the need for a microcavity to enhance the local density of states. This could provide a means to engineer large area devices with strongly enhanced spontaneous emission. Previously, although microcavity devices have demonstrated enhancement of the emission rate, these have been in relatively small devices (e.g., pillar-like VCSEL structure with diameters < 1 μm). Therefore, a practical device with useful output power would require a large, dense array of devices. Boroditsky et al. [99] have measured and estimated the extraction efficiency from photonic crystal slabs consisting of a triangular lattice of holes, showing enhanced extraction efficiency due to the microstructuring; however, no attempt was made to measure any enhancement of the emission rate. Angle-resolved measurements of emission into the conduction photonic bands have provided a means to experimentally map a portion of the band structure. Baba et al. [110] have also examined the spontaneous emission from a two-dimensional array of microcolumns (forming essentially, the inverse structure from the

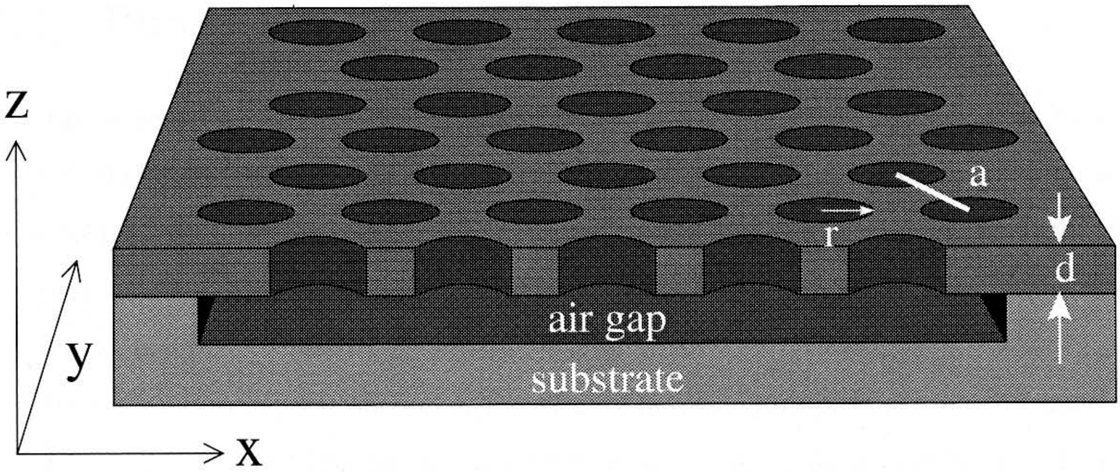

Figure 7.1: Schematic of triangular lattice photonic crystal slab structure for modified spontaneous emission measurements.

triangular array of air holes) in a hexagonal lattice. In [110], an attempt was made to measure the spontaneous lifetime modification due to the photonic structure. However, it was found to be completely dominated by the surface recombination and any modification of the spontaneous emission rate was not detectable.

7.2 Device design and fabrication

The photonic crystal slab structure is shown schematically in Fig. 7.1 and is similar to that examined through numerical simulations in chapter 6 and shown in Fig. 6.1. The slab structure consisted of 6 nominally unstrained $In_{0.53}Ga_{0.47}As$ quantum wells in a d = 150 nm thick InGaAsP slab identical to the epitaxial structure shown previously in Table 4.1. The fabrication followed essentially the same process as described in Fig. 4.2. A series of devices were fabricated in close proximity on the same wafer with lattice sizes from a = 960 nm to 300 nm with a nominal r/a = 0.35. Fabrication random and systematic errors are the same as described in section 5.4 and shown in Fig. 5.10.

7.3 Phase sensitive spectroscopy

The phase sensitive spectroscopy technique was first proposed by Henry and Nassau in 1970 [115]. Advances in modern electronics and lock-in amplifier technology has reduced the complexity of this type of measurement and eliminated the need for the complex electronics consisting of RF amplifiers, a balanced mixer, and a variable delay line, originally used by Henry and Nassau. A block diagram of the setup used for these measurements is shown in Fig. 7.2. The laser pumping source consisted of a Coherent Mira 900 Ti-Sapphire laser (S2) pumped by an argon ion laser (S1) and mode-locked at approximately 76 MHz. A reference signal was obtained by sampling a small portion of the beam (BS1) detected by a high-speed photodetector (D1). The pump pulse train was then passed through an acousto-optic modulator (AOM). The acousto-optic modulator RF driver signal was passed through an RF switch connected to a pulse generator synchronized with a frequency divider triggered by the 76 MHz reference signal. This provided a means to rapidly switch the pulse train on and off. Unfortunately, the AOM had insufficient bandwidth to switch individual Ti-Sapphire pulses, however packets of 20-30 pulses was possible. A 30-pulse packet corresponds to a total packet time of approximately 400 nsec. By switching packets with a low duty cycle, the heating of the membrane device (thermal response time on the order of microseconds) can be limited while maintaining the high peak pulse power and the 76 MHz fundamental modulation frequency.

According to Henry and Nassau [115], if the signal-to-noise of the measured signal is (S/N), then the accuracy of the phase delay $\phi = \omega\tau$ measurement is approximately $(\mathrm{S/N})^{-1}$. Therefore, the error in the lifetime τ will be $\Delta\tau \approx (S/N)^{-1}\omega^{-1}$. For the Stanford Research SR844 lock-in amplifier used as the phase sensitive detector, the signal-to-noise can be roughly estimated. For typical amplifier settings and an integration time constant of 3 sec, the equivalent noise bandwidth is $5/(64T) = 0.026$ Hz [116]. For typical experimental conditions, the signal-to-noise ratio with an equivalent noise bandwidth as described above was approximately between 30 and 100 at a modulation frequency of 76.5 MHz and the measurement accuracy is

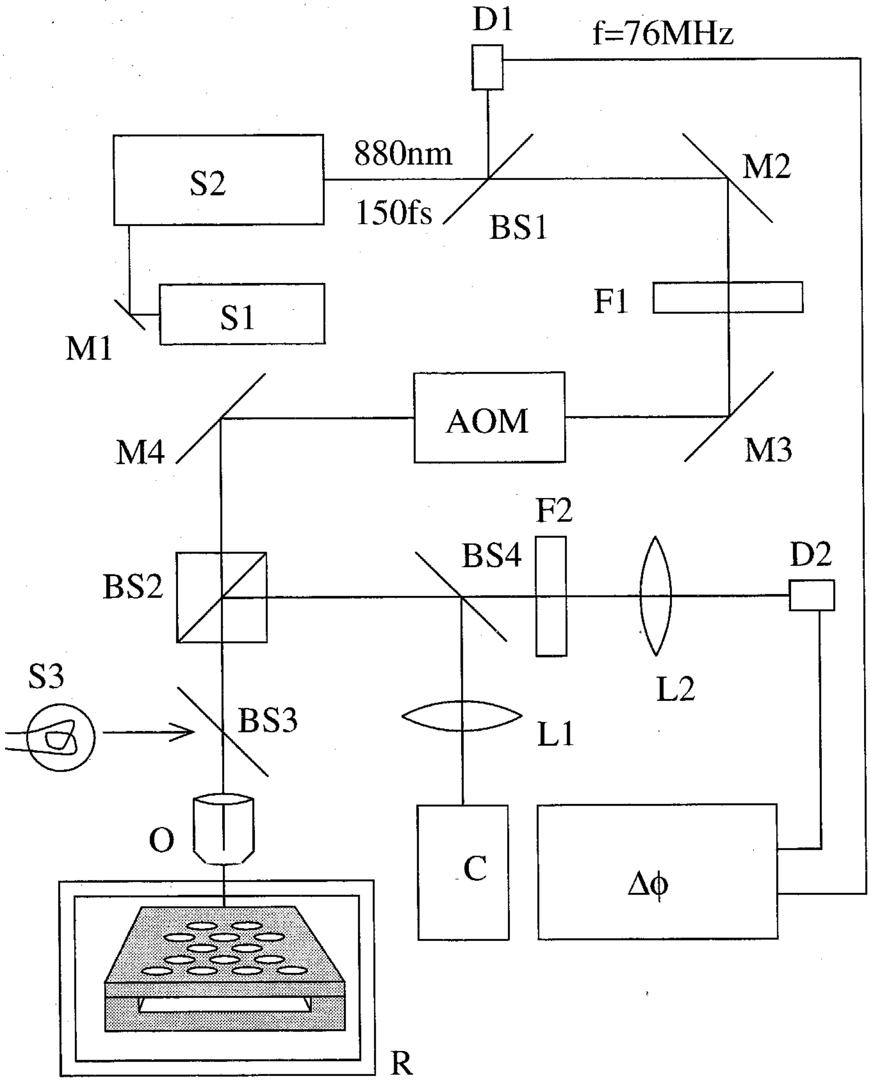

Figure 7.2: Phase sensitive spectroscopy measurement setup. S1=Argon ion laser, S2=Ti-sapphire modelocked laser, S3=xenon lamp, M1-4=mirrors, BS1-4=beamsplitters, F1=variable neutral density filter, F2=Wavelength selective filter, L1-2=lenses, O=Infrared apochromatic objective, C=imaging camera, D1-2=high speed detectors, $\Delta\phi$=phase detection electronics, R=Joule-Thomson refrigeration chamber.

$\Delta\tau = 21-70$ psec. One of the advantages of such techniques is the ability to measure processes on the order of 50 psec with a detector system with a bandwidth $\ll 1/(50$ psec$) = 20$ GHz.

7.3.1 Non-exponential decay processes

The phase sensitive spectroscopy technique, as originally described by Henry and Nassau [115], fundamentally assumes an exponential decay process so that lifetimes can be calculated from the phase delay information. However, in optically pumped intrinsic semiconductors, this is not an accurate assumption; however, experimental data in section 7.5 will be interpreted under the exponential decay assumption. This is necessary because the complex interaction between the different processes (surface, binomial, and Auger recombination) and the difficulty in accurately determining the carrier density in the active layer precludes correcting the exponential decay assumption for these other effects. However, it will be shown that these effects are not significant in some cases. In addition, the qualitative results are not altered and this assumption can be used as a lower limit for the relative change in spontaneous emission rate. In other words, the estimated emission rate change from using the exponential approximation and ignoring the possible contribution of Auger recombination will be smaller than or equal to the actual rate change.

In general, the decay of carriers in semiconductor is not an exponential process and can be described by the rate equation [117]

$$\frac{dn}{dt} = -An - Bn^2 - Cn^3 \tag{7.1}$$

where A is the point and surface recombination coefficient, B represents the binomial recombination process and C is related to the various Auger recombination processes. Consider a generalized decay process in which the time derivative of the carrier density is proportional to some power of the carrier density (k-1). For this general case, the free decay rate equation can be solved as

$$\begin{aligned}\frac{dn}{dt} &= -Cn^{k+1} &(7.2)\\ \frac{d}{dt}(\log n) &= -C\exp(k\log n) &(7.3)\\ n(t) &= \sqrt[-k]{kCt + n_0^{-k}} &(7.4)\end{aligned}$$

where n_0 is the carrier density at time t = 0. In the InGaAsP material system, Auger recombination is typically a significant loss factor. However, this only becomes significant for relatively large carrier densities [118] compared with estimated carrier densities generated in these experiments and given typical material decay coefficients. Additionally, these experiments involve the impulse response decay since the mode-locked laser generates 150 fsec pulses. Auger recombination will dominate at higher carrier densities however, the tail of the decay process will be dominated by the lower order processes. For high carrier densities, the fast initial decay due to Auger recombination may not be apparent due to the finite response time of the detector. In these experiments, a detector/amplifier system with a response time of approximately 200 - 300 psec was used. This will be discussed in greater detail in the following sections.

Binomial decay

Consider a binomial decay process such that k = 1 and the decay constant is the binomial recombination constant C ≡ B. In this case, the time decay is

$$n(t) = \begin{cases} \frac{n_0}{n_0 Bt+1} & \text{for } t >= 0 \\ 0 & \text{for } t < 0 \end{cases} \tag{7.5}$$

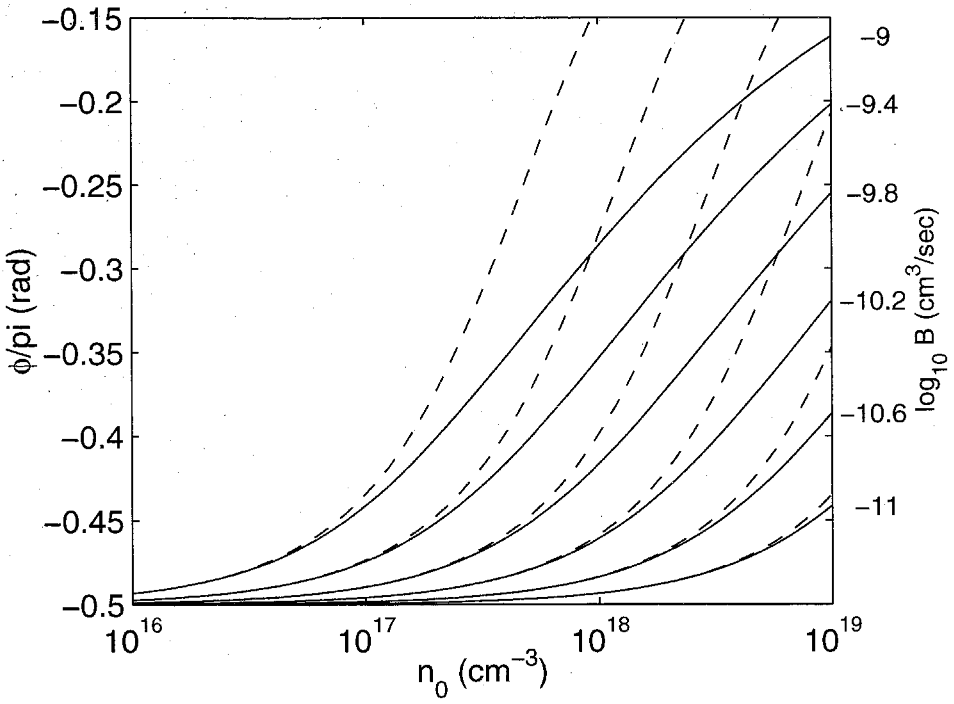

Figure 7.3: Phase delay for the binomial decay process versus peak carrier density and binomial decay constant (B) at a frequency of 76.36 MHz. The solid lines are for different B-coefficients as indicated to the right. The dotted lines the exponential decay phase delay curves for $1/\tau = Bn_0$.

By some simple transformations, the Fourier transform of $n(t)$ can be expressed in terms of the exponential integral [119] as

$$\begin{aligned} \mathcal{F}[n(t)] &= \int_0^\infty \frac{n_0 \exp(-i\omega t)dt}{n_0 Bt + 1} && (7.6) \\ &= \frac{1}{B} e^{\frac{i\omega}{Bn_0}} E_1\left(\frac{i\omega}{Bn_0}\right) && (7.7) \end{aligned}$$

where the exponential integral is defined as $E_1(z) = \int_z^\infty dte^{-t}/t$. The phase response of this decay process in the frequency domain is a function of both the initial carrier density n_0 and the decay constant B. This is shown in Fig. 7.3 for a modulation frequency of 76.36 MHz (a typical value for these experiments) where the binomial decay constant B has been varied by one order of magnitude around a typical value of 1×10^{-10} cm^3/s for this material system [120]. The phase delay from a modelled exponential decay process where the decay constant is approximated as $1/\tau = Bn_0$

is shown for comparison. In the region of low initial carrier density, the deviation from the simple exponential decay phase delay and the binomial decay phase delay is minimal. At higher carrier densities, the longer tail of the binomial decay compared to the exponential decay results in a larger phase delay. The means that if the decay process is binomial, then the measured phase will be larger than the expected value from an exponential decay model. However, the sensitivity limit of a real detection system will mitigate this somewhat. When the decay tail drops below the minimum detectable power of the measurement system, defined by the dark current of the detector and the leakage currents in the electronics, the resulting phase shift is reduced compared to the infinite sensitivity model. In the measured results in the following sections, the exponential decay model will be used since the binomial decay is not an analytically invertible function. It is important to note that even though the binomial and the exponential decay functions result in different measured phase shifts, they are both monotonically increasing with the carrier density and therefore, larger phase shift in either case corresponds with a slower decay process.

Auger recombination

The actual rate equation for the decay process (Eq. (7.1)) includes both the binomial recombination as well as the Auger process. It was previously argued that the Auger rate can be ignored. Fig. 7.4 shows a theoretical calculation of the effect on the phase delay of including the Auger recombination term versus the peak carrier density for binomial decay constants from 1×10^{-11} to 1×10^{-9} cm^3/sec and assuming an Auger recombination constant of $C = 7.5 \times 10^{-29}$ cm^6/sec [118, 120]. For a larger binomial decay constant ($B = 1 \times 10^{-9}$ cm^3/sec, highest curve), there is essentially no significant phase shift by including the Auger process. For lower decay constants, the Auger process can introduce a significant reduction in the measured phase delay at high carrier densities. However, as in the previous section, this has the effect of reducing the measured phase delay range for the same change in the binomial recombination coefficient. This means that larger phase delays still imply slower binomial recombination and that the measured phase delays will give a smaller change

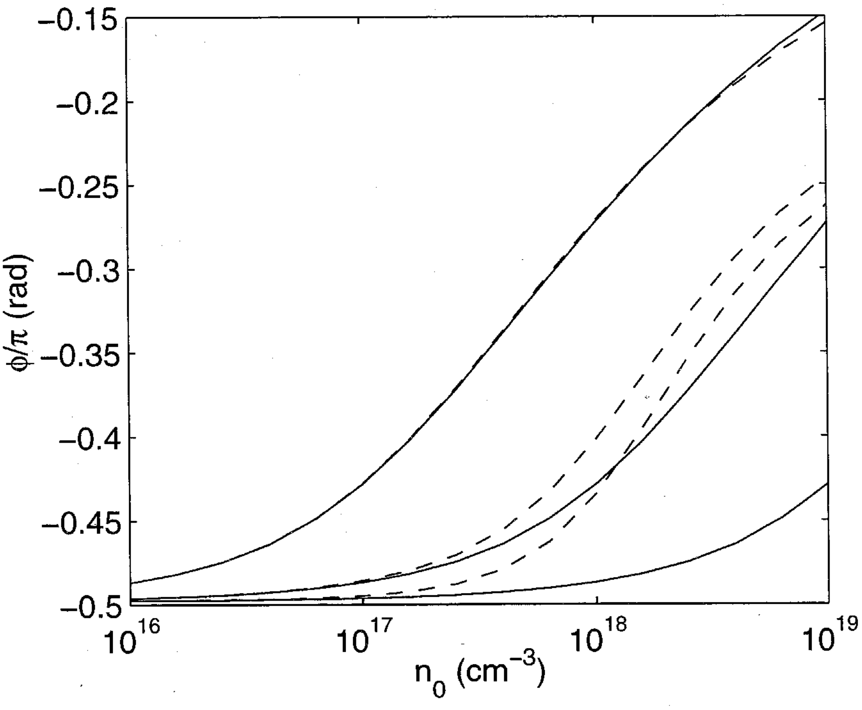

Figure 7.4: Phase delays including Auger recombination. The curves for respectively smaller phase delays, correspond to B = 1×10^{-11}, 1×10^{-10} and 1×10^{-9} cm^3/sec. The solid lines are the binomial decay only curves and the dotted lines include Auger recombination.

in the decay rate by ignoring the Auger recombination contribution than the actual change.

The decrease in phase shift due to the Auger recombination shown in Fig. 7.4 is reduced (a reduced decrease ≡ increased phase delay) due to the finite response time of the detector system used. For a detector response time of approximately 250 psec, the fast initial decay characteristic of the (n^3) Auger process is smeared by the detector. This results in an increase in the effective measured phase delay so that the measured phase including the Auger process will more closely match the Auger-free phase delays. The effect of the binomial decay process (compared to the exponential approximation) results in faster decay (B larger) giving a larger than expected phase delay. The effect of adding Auger recombination results in the slower decay (B smaller) to give a smaller than expected phase delay. The net result is the compression of the phase delay range for a given change in the binomial decay constant which results in a underestimation of the modification to the spontaneous emission rate.

7.3.2 Double lock-in measurement

Measurements of inhibited spontaneous emission suffer from the inherent difficulty that a reduced spontaneous emission rate also leads to low radiative efficiency. The radiative efficiency η_{rad} can be written as

$$\eta_{rad} = \frac{\Gamma_{rad}}{\Gamma_{rad} + \Gamma_{nr}} \tag{7.8}$$

where Γ_{rad} is the radiative emission rate and Γ_{nr} is the total transition rate due to all non-radiative processes. Clearly, assuming a constant non-radiative transition rate, any inhibition of the spontaneous emission rate leads to a corresponding reduction of the radiative lifetime. The photonic crystal slab structures inherently have a relatively low radiative efficiency because of the large non-radiative surface recombination rate. If the spontaneous emission rate is reduced due to inhibited spontaneous emission, a high-sensitivity measurement technique is necessary.

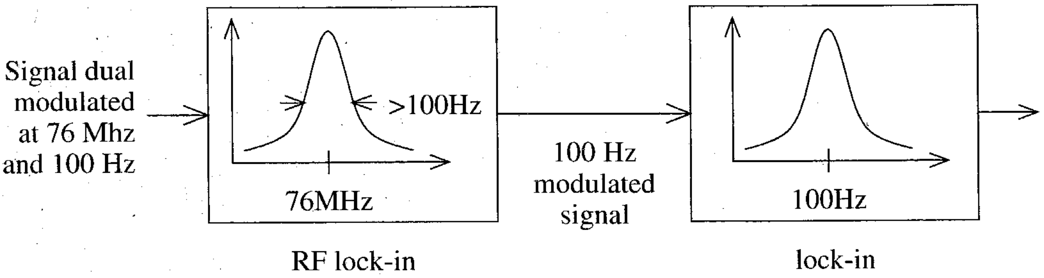

Figure 7.5: Schematic of high-sensitivity dual-modulated measurement technique.

Radio frequency electrical signals can suffer significant radiation and coupling if not properly shielded. Even with good shielding, extremely sensitive measurements may be limited by the RF pick-up in the detector system. In this case, a lock-in measurement at the modulation frequency (76 MHz) may detect the RF radiation rather than the desired signal. One solution for this is to use a dual-modulated technique. In this case, in the apparatus shown in Fig. 7.2, the acousto-optic modulator is replaced by a optical chopper, which modulates the pump beam at a relatively low frequency (100 Hz). The dual-modulated technique is shown schematically is Fig. 7.5. The modulated signal is detected by an RF lock-in amplifier to filter only the high-frequency modulated signal (76 MHz) with a bandwidth larger than the low-frequency modulation. The low-frequency modulation can then be detected using a second lock-in amplifier to ensure that the high-frequency radiation is eliminated from the measurement since it will not contain the low-frequency modulation component.

7.4 Power emission from a photonic crystal slab

The detected spontaneously emitted power from the photonic crystal slabs at different lattice sizes is shown in Fig. 7.6 at different time-averaged pumping powers using the dual-modulated measurement technique described in section 7.3.2. The devices used in this measurement differ slightly from those discussed previously and shown schematically in Fig. 7.1. In this case, a sapphire layer was attached to the front surface of the membrane structure to provide a thermal conduction path for heat removal.

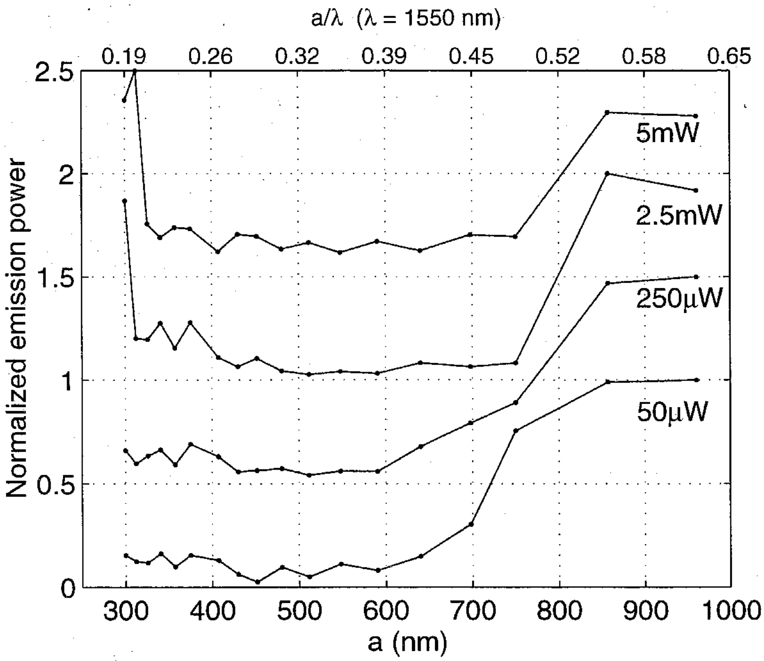

Figure 7.6: Normalized spontaneous emission power versus lattice spacing. Sequential plots for increasing pump power are shifted by 0.5 units for clarity. An estimated normalized frequency (assuming $\lambda = 1550$ nm) is indicated above the plot which is only approximately correct for the lowest pumping level. The band edges can be seen to shift to larger lattice spacing, which corresponds with a shift of the emission wavelength with increasing membrane temperature.

At low pumping power of 50 μW, the emission power for structures with large lattice sizes ($>$ 700 nm) is relatively high corresponding to emission into the "conduction" photonic bands. For smaller lattice sizes, the emission power reduced by approximately one order of magnitude for all devices with lattice sizes less than 700 nm (in normalized frequency units a / $\lambda \approx 0.45$ at $\lambda = 1550$ nm). This corresponds with the predicted behaviour shown previously in Fig. 6.8 for a structure with fixed slab thickness. At higher pumping powers the transition edge from high to low emission power, which is attributed to the conduction band edge, shifts slightly to higher lattice sizes. Since at higher pumping power, the emission wavelength of the membrane shifts to longer wavelengths due to heating of the structure, this corresponds to essentially constant normalized frequency (a/λ).

For larger pumping powers (2.5 and 5 mW), a rise in the emission power is seen for small lattice sizes. However, in this regime of the band structure below the band gap, significant emission is not expected because the photonic bands lie completely below the light line (see Fig. 6.4) and should not couple in the vertical direction. This is due to the presence of the sapphire layer above the structure. Although the refractive index of sapphire is relative low, maintaining the vertical total internal reflection confinement, it results in an asymmetric waveguide ($n_{sapphire}$ versus air below the slab). This asymmetry is the likely source of the vertical coupling seen in the small lattice size devices at high pumping powers. This emission power increase was not observed without the sapphire layer. However, these pumping powers > 2.5 mW were not achievable in that case due to catastrophic thermal failure of the membranes without the thermal conduction path provided by the sapphire.

7.5 Measurement of spontaneous lifetime

7.5.1 Unpatterned material lifetimes

Using the phase sensitive spectroscopy method, the effective transition rates for unpatterned material versus the pumping power is shown in Fig. 7.7, assuming an exponential decay process. The material was nominally intrinsic such that the recombination process would be expected to obey a binomial decay process

$$\frac{dn}{dt} \propto -Bnp = -Bn^2 \tag{7.9}$$

where n and p are the electron and hole free carrier densities which are assumed to be equal. By making an exponential decay assumption, the decay constant from Eq. (7.9) can be approximated as $1/\tau \approx Bn$. Measurement of the decay constant versus carrier density (which is assumed to be proportional to the pumping power) can be used to determine the binomial decay constant B [117]. For low pumping powers (< -10 dBm), a linear relationship between the inverse lifetime and the pumping power. By approximating the absorption in the structure and using the pump beam size to estimate the excited carrier density, this fit gives a binomial recombination coefficient of approximately $B = 1.5 - 1.7 \times 10^{-10}$ cm^3/sec. This agrees roughly with,

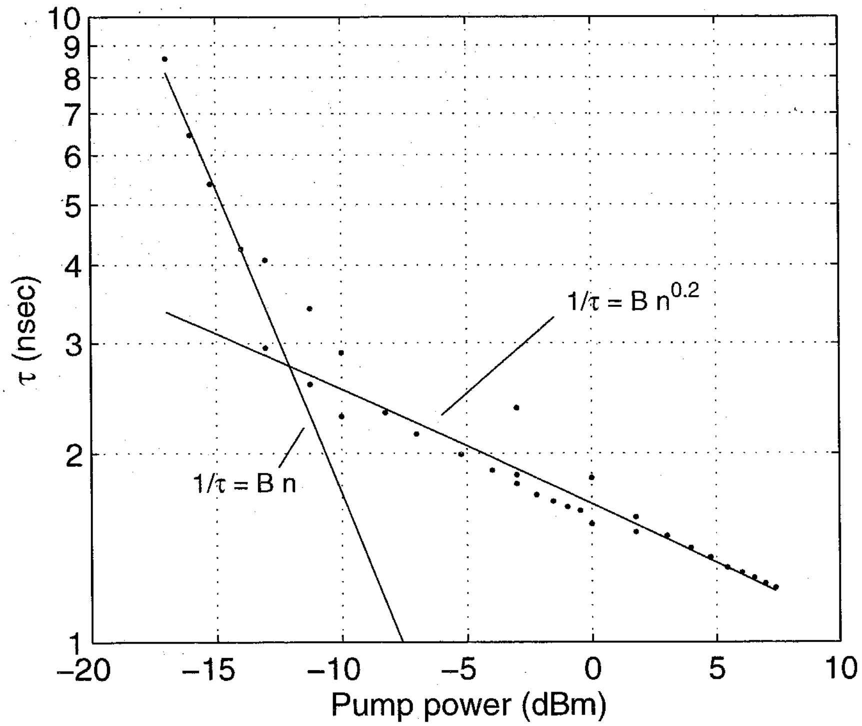

Figure 7.7: Unpatterned material transition rate measured from phase sensitive spectroscopy.

for example, Coldren et al. B = 1×10^{-10} cm^3/sec [118] measured for the same material system using a different measurement technique. For higher pumping levels, the decay lifetime variation with pump power varies similar to the $1/5^{th}$ root of the pumping power. This dependence is shown only as a visual aid to emphasize the change in slope. From the results of section 7.3.1, this dependence on pumping power (and therefore carrier density) does not asymptotically approach a constant slope.

7.5.2 Photonic crystal slab lifetime

A series of photonic crystal slab structures with varying lattice spacing were fabricated in close proximity on the same wafer all with nominal hole radii of r/a = 0.35. Using the phase sensitive spectroscopy technique, the phase delays of the luminescence from these structures were measured as a function of the device lattice size and the incident pump power. The emission wavelength shift with pumping power was measured by comparison with an unpatterned membrane structure and the effective pumping was determined by scaling the incident power by the material fill fraction for the patterned structures. This is only an approximation of the difference in absorbed power. Since the photonic structure modifies the light extraction efficiency, clearly by time-inversion symmetry, the efficiency of pump light entering the structure (related to the pumping efficiency) may also be altered. However, this difference due to the changing pumping efficiency will be ignored. This resulted in a shift to lower normalized frequency a/λ for each device as a function of pumping power. The complete data for all devices and lattice sizes are shown in Fig. 7.8 where the approximate range of normalized frequencies for each lattice spacing is indicated. The sample substrate was temperature stabilized using a Joule-Thomson microrefrigeration chamber to within ±0.1°C. The phase delay measurements presented in this section were taken with a substrate temperature of 17.0°C.

Note that a shift of the normalized frequency to lower values corresponds with higher pumping power and therefore longer emission wavelength. A three-dimensional plot of phase delay versus normalized frequency and pump power is shown in Fig. 7.9 for the same data for comparison. The largest lattice sizes (960 and 857 nm) show a decrease in the phase delay and therefore the decay coefficient with increasing pumping power. Although this may be evidence of the binomial decrease of the spontaneous lifetime due to increased carrier density, this is complicated by the fact that as the normalized frequency shifts, the emission samples a different portion of the bandstructure. Therefore this change may be linked to modification of the spontaneous emission rate. The next two smaller lattice sizes (750 and 698 nm) show only small variation in the phase delay with pumping power. Because of the complex interplay between modified spontaneous emission, the density of states spectrum and the binomial recombination process, it is difficult to make definitive conclusions from these two devices.

For the lowest pumping powers for the first three devices, the phase delays are approximately -3.2°, -2.5°, and -1.9° for the 960, 857, and 750 nm lattice sizes, respectively. At low carrier densities, it is expected that surface recombination may dominate due to the large surface-to-volume ratio of these structures. For a modula-

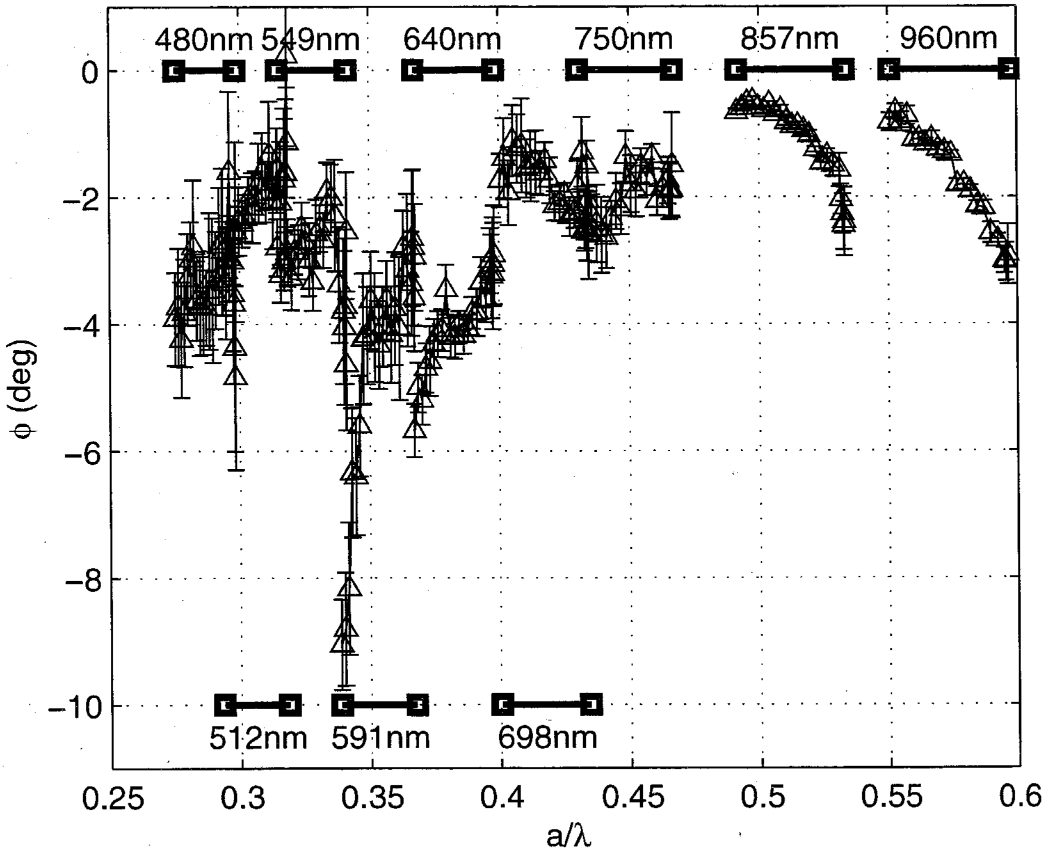

Figure 7.8: Measured phase delay versus a/λ for all pumping power and devices with different lattice spacings. The lattice spacings for each device is indicated above and below the data. The error bars represent the phase error measured as the standard deviation of the measured phase over > 100 time constants of the detection system.

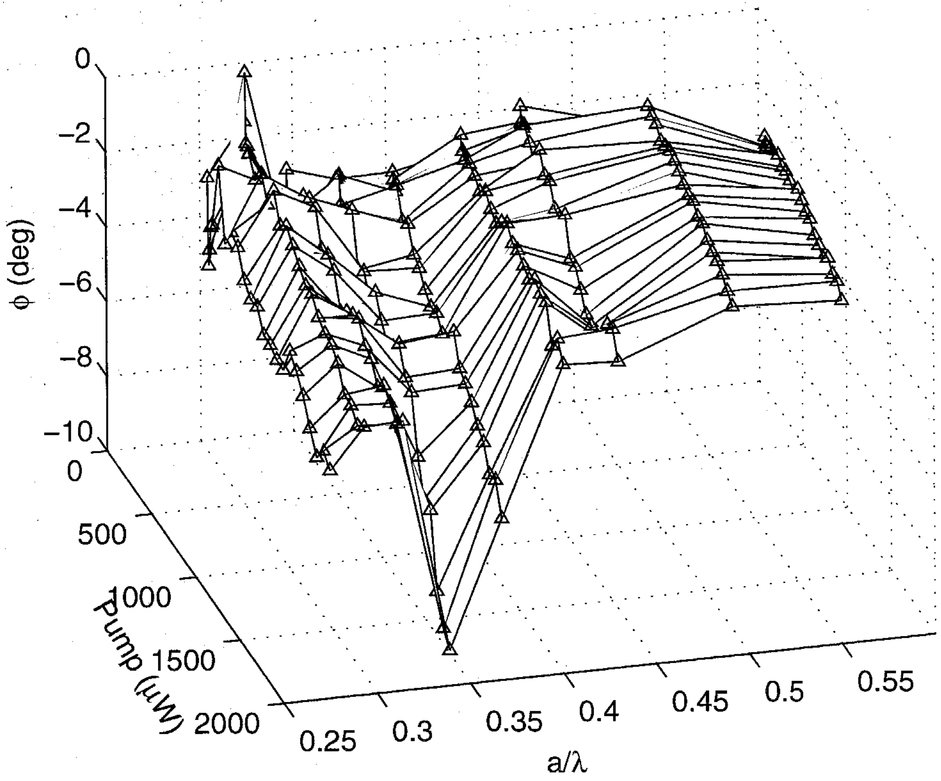

Figure 7.9: Measured phase delay of signal versus pumping power and lattice size. The peak wavelength of emission used has been corrected for the shift due to the heating of the membrane.

tion frequency of 76.4 MHz and assuming exponential decay (which would be correct for surface recombination), this corresponds to decay times of approximately 110 psec, 90 psec, and 70 psec, respectively. This shortening of the lifetime with shrinking lattice size is consistent with the expected behaviour of surface recombination [110, 121]. However, there is no way to conclusively determine that the decay process is surface recombination dominated from this data even though, in the limit of small carrier density, this will be the case.

The variation in the phase delay versus pumping power for the next smaller devices with lattice spacings of 640 and 591 nm show particularly interesting behaviour. First, note that the phase delays for these devices exhibit noticeably larger phase delays for all pumping powers. Also, both devices, and particularly the 591 nm device, show a dramatic increase in the phase delay as the pumping power increases. In section 7.5.3

it will be shown that this is due to the saturation of the surface states so that a shift from the fast surface recombination to a slower spontaneous decay is seen. Therefore the highest pumping power points (and correspondingly the largest phase delays) are points where the phase delay represents the spontaneous decay process with the surface recombination saturated, assuming that the Auger recombination can still be ignored. The final three devices with lattice sizes of 549, 512, and 480 nm shown in Fig. 7.8 and Fig. 7.9 show only small variation in the measured phase delay versus the pumping power. From Fig. 7.8, it is clear that there appears to be a frequency range exhibiting larger phase delays, which correspond to a slower decay process, for frequencies between approximately $a/\lambda = 0.34$ and 0.40 and may extend down to 0.32 although data near this frequency show relatively large error bars due to extremely low signal levels. This is in approximate correspondence with the theoretical predictions for the bandgap location. However, the shift in the relative slab thickness (d/a) for different lattice sizes (a) as discussed in chapter 6 and shown in Fig. 6.7 make a direct comparison with numerically determined band structure difficult. However, this increased phase delay band has been confirmed through measurements on different devices with nominally the same range of parameters. These also show the dramatically increased phase delay for devices within a band corresponding approximately with the predicted bandgap location.

Assuming that an exponential decay model can be used, the effective lifetimes versus pumping power and normalized frequency are shown in Fig. 7.10. Although the exact numerical values for the decay constant may not be accurate due to the differences between the exponential decay model and the binomial decay process, the band gap reduction in the spontaneous lifetime is clearly visible at high pumping powers where the surface recombination is saturated. This represents a greater than one order of magnitude increase in the lifetime between the fastest out-of-gap decay ($\tau \approx 30$ psec at $a/\lambda = 0.55$ nm) and the slowest point measured in the bandgap ($\tau \approx 330$ psec at $a/\lambda = 0.34$). From the discussion in section 7.3.1 for a given carrier density and therefore pumping power, the change in the phase delay versus the binomial recombination coefficient is reduced compared to the phase delay change if the process

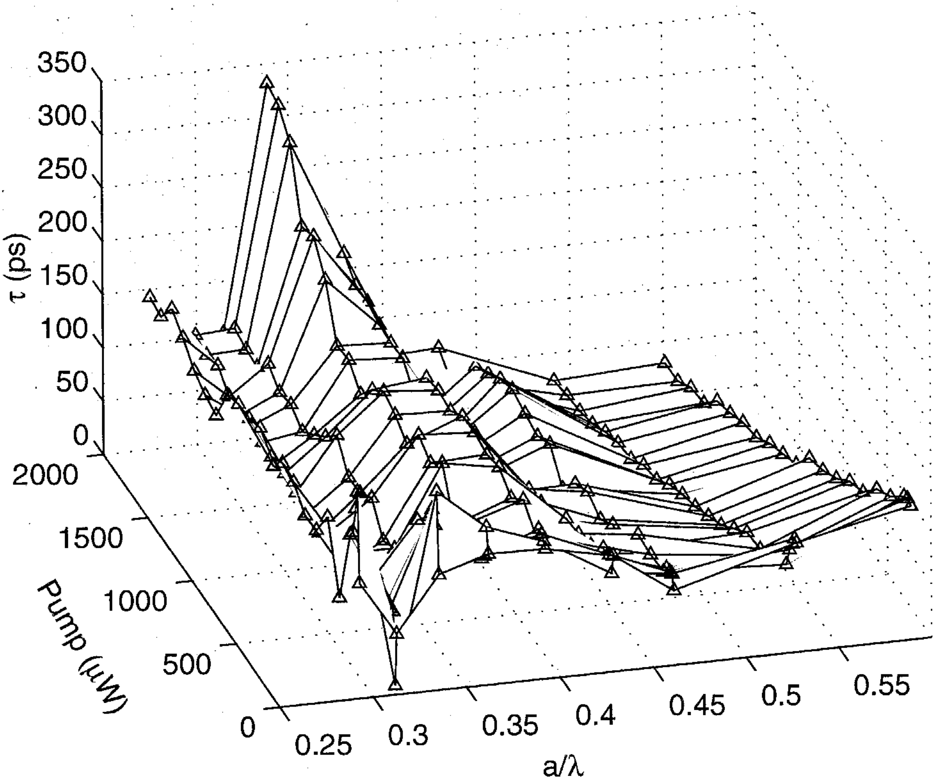

Figure 7.10: Effective decay constant assuming an exponential decay process versus pump power and normalized frequency. The same correction to the emission wavelength as in Fig. 7.9 is used. A long lifetime peak develops for high pumping powers. This is not visible at low pumping powers due to a fast surface recombination process which is saturated at higher carrier densities.

was truly exponential as shown in Fig. 7.3. Therefore spontaneous emission inhibition calculated by the exponential approximation is a lower limit and the actual lifetime ratio may be larger. Additionally, Fig. 7.10 also shows that particularly for the increased lifetime points, the lifetime versus pumping power has not shown any sort of saturation effect and the lifetime may continue to decrease with increased pumping power. This indicates that due to the slower radiation process, the carrier density required to completely saturate the surface recombination process is raised. However, due to catastrophic thermal failure of the membranes, it was not possible to perform measurements at higher pumping powers.

Assuming that the higher pumping powers are above the saturation carrier density for the surface recombination process, these phase delays and corresponding lifetimes can be taken as representative of the actual spontaneous decay process. The exponentially approximated lifetimes versus normalized frequency for pump powers from 1.8 to 2.0 mW are shown in Fig. 7.11. This clearly shows the reduced spontaneous emission rate points that may indicate the photonic bandgap spectral position from $a/\lambda = 0.32$ to $a/\lambda = 0.4$. Since Fig. 7.8 and Fig. 7.10 show that the short lifetime points at approximately $a/\lambda = 0.5$ and 0.55 are decreasing in lifetime versus pumping power and that the long lifetime points near $a/\lambda = 0.35$ are increasing in lifetime versus pumping power, the actual inhibition of the spontaneous emission rate may actually by significantly larger than the 10× difference shown here.

7.5.3 Surface recombination saturation

Many of the conclusions in the previous section depend on the saturation of the surface recombination process. The InGaAsP material system was chosen for its relatively small surface recombination velocity, which derives from its inherently low surface state density [122]. This same low surface state density results in a relatively low carrier density required to saturate these states. The saturation of the surface states with optical pumping in this material system for dry etched microstructures has been observed for example, by Maile et al. [121] and by Hübner et al. [123]. Wet etched structures and a comparison with dry etched surface state saturation has also been shown by Jacobs et al. [124, 125] by photoluminescence measurements. These results have been confirmed by cathodoluminescence by Evoy et al. [126]. The effect of surface state passivation by silicon on the surface state saturation has been examined by Fujikura et al. [127]. All these studies have shown that for a variety of different etching technologies (which result in different material surface damage), although the surface recombination velocity and surface state saturation carrier density are variable, the required optical pumping power density to saturate this decay process is not very high and seems to vary by less than an order of magnitude (although a precise comparison of all these different works is difficult because of the variety of techniques used).

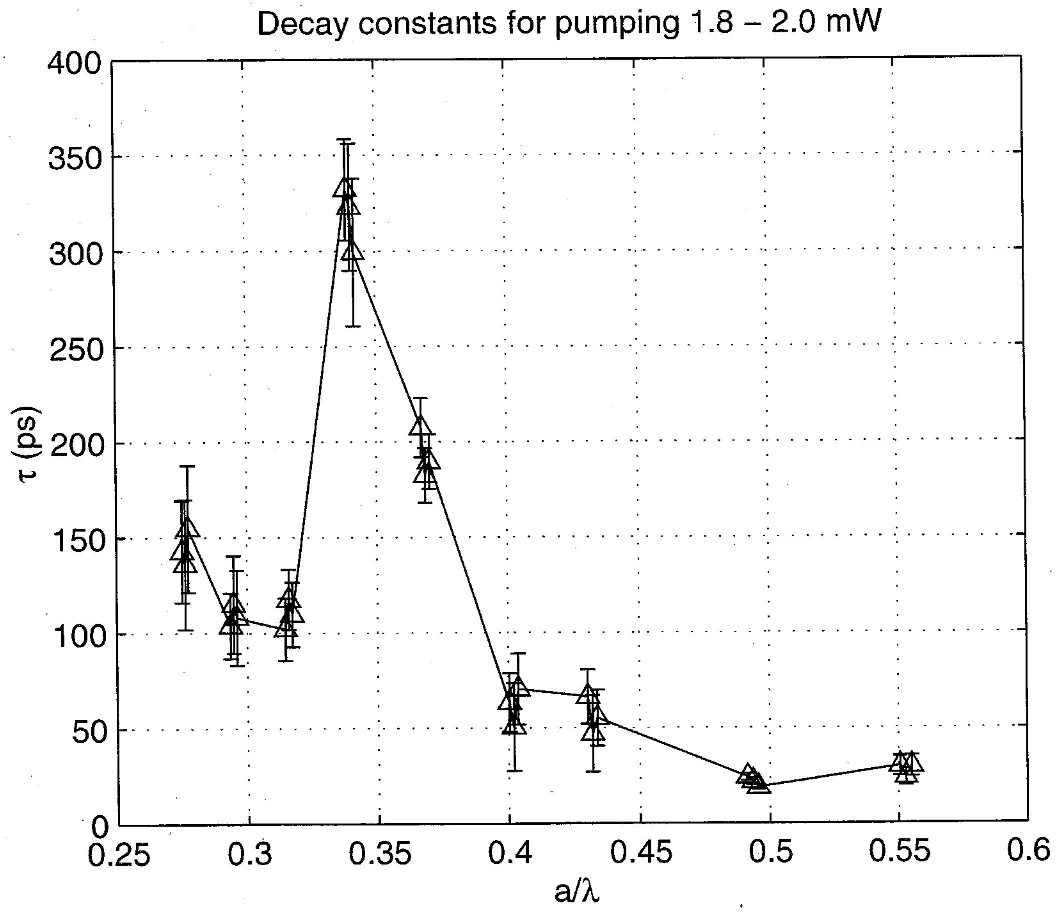

Figure 7.11: Photonic crystal slab lifetimes for devices from a = 960 nm to a = 480 nm at high pump powers (1.8 mW to 2.0 mW) showing bandgap inhibited spontaneous lifetimes. Higher carrier densities at these pump powers saturate the surface recombination so that a slow radiative rate can be measured. Maximum lifetime of approximately 350 psec may actually be longer due to incomplete surface state saturation.

A parameter proportional to the radiative efficiency can be used to measure the required pumping power to reach saturation. The ratio of the measured power to the pumping power is proportional to the radiative efficiency (the proportionality constant is the detection and collection efficiency). The radiative efficiency dependence on the pumping power is shown in Fig. 7.12 for the device with a lattice spacing of 857 nm and in Fig. 7.13 for a lattice spacing of 960 nm. The emission wavelength shifts with pumping power due to the thermal heating of the membrane resulting in a shift in normalized frequency a/λ. This means that the saturation power measured from these efficiency curves may not be accurate. However, for these devices, which are far away from the bandgap frequency range, the effect of the bandstructure should be reduced. In the limit of large lattice sizes, there should essentially be no modification of the radiation (either decay lifetime or radiation pattern). These efficiency curves also demonstrate that for these short lifetime points from Fig. 7.10 for pumping powers greater than 1 mW (0 dBm), the surface recombination process is clearly beyond the saturation point. This means that the contribution to the phase delay measurements for these devices from surface recombination can be neglected.

From efficiency curves such as those shown in Fig. 7.12 and Fig. 7.13, the saturation pumping power was measured for several points on either side and away from the bandgap. These are plotted versus the inverse lattice spacing (1/a) in Fig. 7.14. It has been shown (see for example [110]) that the surface recombination rate scales as one over the characteristic distance from any point in the structure to the nearest surface. In this structure, clearly the characteristic distance scales as the lattice size. This shows that for the relatively fast radiative decay processes above and below the bandgap, measurements at pumping powers up to 2 mW should be near or beyond the saturation point where surface recombination need not be considered. However, for the points with a reduced radiative recombination rate, the saturation power will be correspondingly increased such that even at the maximum pumping power, the smaller lattice spacing devices may still have significant surface recombination. This result corresponds well with the lifetime behaviour as a function of pumping power discussed in the previous section.

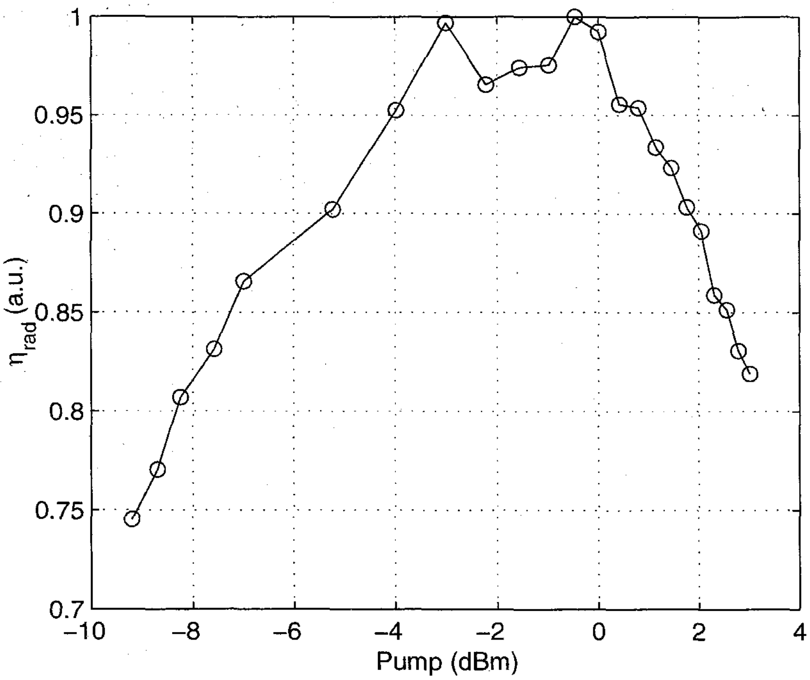

Figure 7.12: Power dependent radiation efficiency from a photonic crystal slab device with a = 857 nm. Saturation of the surface states is seen as a peak at ∼ −1.5 dBm pump power. The decrease in efficiency above this is due to detector responsivity and reduced internal quantum efficiency and also occurs in unpatterned samples.

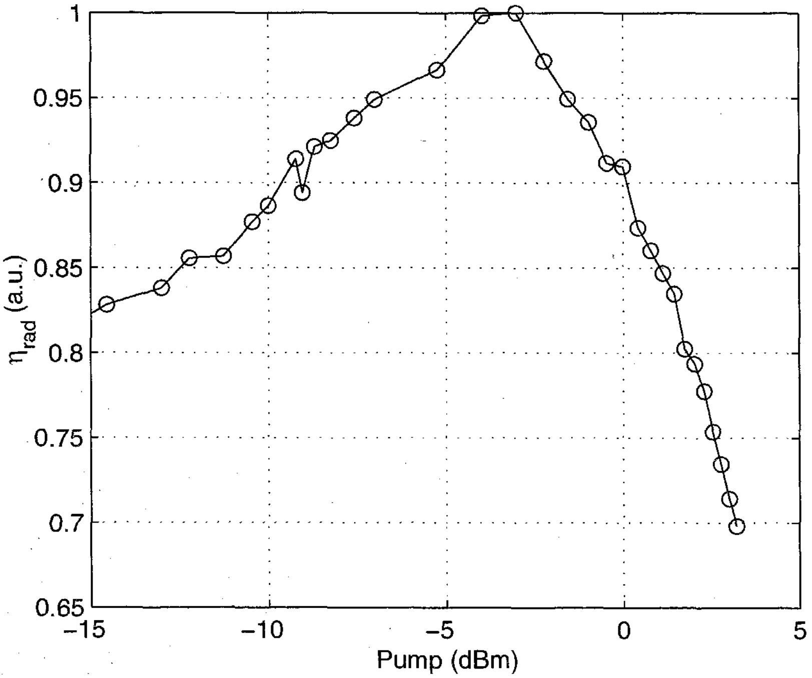

Figure 7.13: Power dependent radiation efficiency from a photonic crystal slab device with a = 960 nm saturating at ∼ −4 dBm.

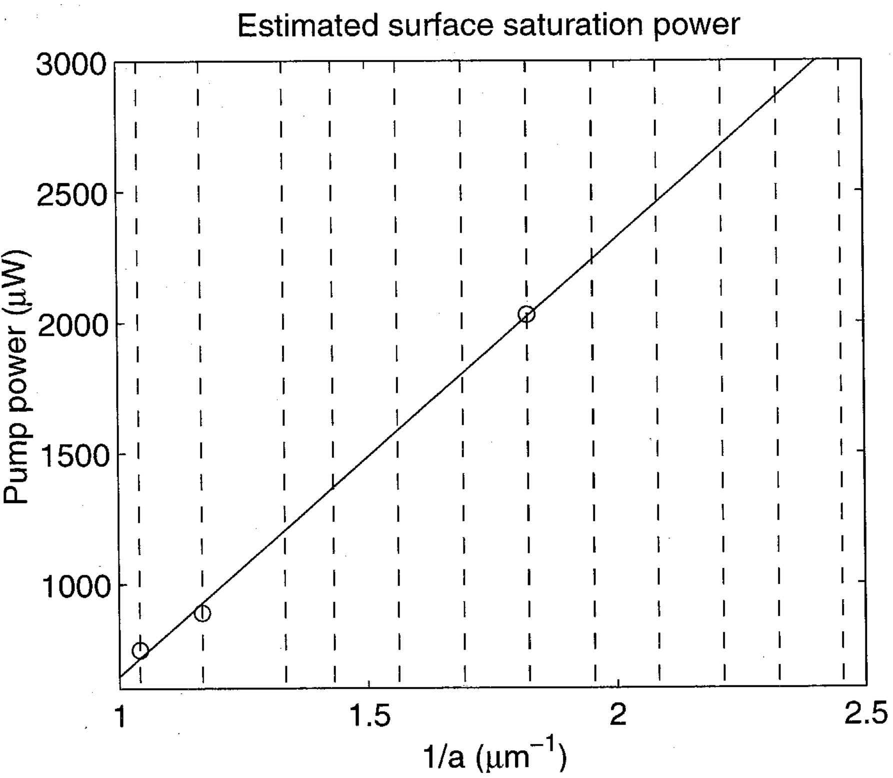

Figure 7.14: Projected saturation powers. Saturation powers for a = 960, 857 and 549 nm are taken as the peak of the efficiency curve. Plotting versus 1/a gives an estimate of the power necessary for surface state saturation for the difference lattice sizes. The sizes for measured devices are indicated by the dotted vertical lines.

7.6 Summary

A dramatic inhibition of the spontaneous rate within the photonic bandgap as compared with the out-of-gap emission rate has been experimentally demonstrated. These measurements have indicated that the out-of-gap emission rate may be significantly accelerated as compared to the unpatterned material emission rate. Although the non-exponential behaviour of the decay process limits the accuracy with which the exact numerical decay lifetimes can be considered, it has been shown that this has the effect of resulting in an under estimation of the relative change. The actual decay lifetime variation between the bandgap frequencies and the out-of-gap frequencies is expected to be larger. Additionally, the photonic structure is expected to alter the pumping efficiency in the same way as the extraction efficiency can be altered. This results in an inability to accurately determine the carrier density in the active layer and therefore also the inability to isolate the contributions of the various non-radiative and radiative decay processes. The spontaneous lifetime within the photonic bandgap has been shown to be greater than one order of magnitude slower than the conduction band emission. The prediction shown theoretically in chapter 6, that a structure lacking a complete photonic bandgap could have a dramatic effect on the spontaneous emission, has been demonstrated.

Chapter 8 Conclusions

8.1 Summary of results

8.1.1 Hexagonal disk and defect microcavities

The goal of high density photonic integrated circuits requires the development of compact and efficient light sources and other optical elements. Photonic crystals have frequently been suggested as a template from which a variety of such devices may be drawn.

Planar hexagonal disk microcavities based on a two-dimensional photonic bandgap structure in the InP material system have been examined. Lasing at room temperature was demonstrated under optical pumping in which the lasing mode was selectable through adjustment of the pumping geometry to change the relative pump-mode overlap of the different cavity modes. The spontaneous emission peaks due to the cavity modes were observed only in the cases where the photonic bandgap was tuned to overlap with the semiconductor quantum well emission band demonstrated bandgap-based optical confinement. A relatively high lasing threshold was observed due to the poor overlap between the pump and the lasing mode and the relatively high membrane temperature due to poor thermal conduction for heat removal with this cavity design. Heat dissipation could be improved by including a supporting post similar to that found in microdisk lasers or by mounting the membrane onto a low index substrate to conserve the index contrast confinement but provide a heat conduction path.

Defects within a photonic bandgap crystal have frequently been suggested as possibilities for creating extremely small optical microcavities. Spontaneous emission spectra from isolated single photonic crystal defects have been presented and are among the first such measurements. Narrow linewidth emission from a cavity with a modal volume [27] similar to $2.5\,(\lambda/2n)^3 \approx 0.03\mu\text{m}^3$. When the pumping region is well localized to the patterned photonic crystal domain, the spontaneous emission shows a narrow cavity mode peak with little or no background emission corresponding to the broader intrinsic material response spectrum. The mode frequency is tunable lithographically across the material emission bandwidth. The defect mode degeneracy can be split by adjusting the cavity geometry, leaving a truly single mode microcavity. The cavity Q can also be adjusted by moving the defect mode to lower normalized frequencies. Pulsed lasing under optical pumping at low temperature (143 K) has been demonstrated.

8.1.2 Spontaneous lifetime

The results in this chapter have shown the mildly surprising result that the spontaneous emission rate in the two-dimensional photonic bandgap slab structure can be suppressed by greater than an order of magnitude even without optimizing the device design. This occurs in spite of the fact that this structure does not exhibit a complete bandgap and is due to the coupling of the modes with the dipole source position in space. We have shown that a two-dimensional triangular lattice photonic bandgap structure in a thin slab can strongly suppress or enhance the spontaneous emission rate by about one order of magnitude even though this structure lacks a complete three-dimensional band gap. The large enhancement rates at the band edges predicted in single dipole calculations are strongly dependent on the choice of dipole position so that spatial averaging is necessary to estimate the general emission properties of the photonic structure as a whole. The bandgap structure can also be used to enhance the vertical extraction efficiency. Emission into the conduction bands can be enhanced while still maintaining relatively large extraction efficiency. In the presence of non-radiative processes, this could result in a structure with enhanced internal and external quantum efficiencies.

Experimental measurements using phase sensitive spectroscopy have provided among the first evidence of strong inhibition of the spontaneous emission rate in a semiconductor photonic crystal slab structure. The ratio of emission rates in the bandgap to the out-of-gap rate is shown to be greater than one order of magnitude assuming an exponential decay process. This has been shown to be a lower bound to the emission rate ratio due to the binomial nature of the decay process and to the contribution from Auger recombination. The lifetime measurements have also shown the practically important result that the surface recombination rate can be relatively easily saturated due to the low surface state density in this material systems. The power extracted in the slab-normal direction also demonstrates the expected high output for conduction band frequencies predicted by numerical simulations that result from a combination of enhanced extraction efficiency and modified spontaneous emission rate, which results in a change of the radiative efficiency.

8.2 Future directions

This and similar works in the field of photonic bandgap crystal structures have only begun to touch upon the wide-ranging possibilities that have been suggested for this class of engineered materials. Much of this has been from the "bandgap" point of view where the photonic crystal to inhibit or block (reflect or diffract) radiation. This is essentially the point of view taken in chapters 4 and 5 to create microcavity devices using the photonic bandgap crystal as a means to confine the electromagnetic radiation. This is the same point of view used to consider photonic crystal waveguides such as those recently demonstrated by Lin et al. [128] and Baba et al. [129]. Although microcavities and photonic crystal defect cavities have been demonstrated as laser sources and some of the spontaneous emission properties have been examined, this can be considered to be only the first step in understanding the use of photonic crystals for microcavity devices. The work in this thesis has demonstrated the feasibility of designing and fabricating microcavity lasers based on photonic crystals, but by no means have these designs been optimized for any particular use nor has it been determined if this is the best choice of geometry or material system.

Clearly, the lasing performance of these devices must be improved. In the larger microcavities, the complex mode structure and mode interaction briefly discussed in chapters 3 and 4 needs to be examined more carefully. Efficient pumping of the microcavities is also a complex problem given the small size of the defect cavities and the critical need for low index of refraction regions above and below the optically thin membrane. Furthermore, any application using these types of microcavities will require the coupling of light into and out of the cavity to or from a waveguide or other free space optics. The efficiency of this process is an issue which has yet to be considered in depth and is not a trivial problem due to the complex emission pattern.

The inhibition of spontaneous emission discussed in chapters 6 and 7 also uses the photonic crystal bandgap properties, in this case to inhibit internally generated radiation. However, the band enhancement of the emission is different in that the existence of a bandgap is not necessary. The symmetry and geometry of the material on a submicron scale can be designed to modify the local electromagnetic environment and thereby change the macroscopic radiation properties. Similar non-bandgap type behaviours have been used for example, to demonstrated lasing or enhanced gain at zero group velocity points in the bandstructure [130, 131] and for designable refraction due to band curvature, the so-called superprism effect [132]. The lifetime measurements of emission from photonic crystal slabs is among the first experimental evidence to date of greater than an order of magnitude inhibition of the spontaneous recombination rate over the entire material emission spectrum using a photonic crystal in the near-infrared. However, due to the complexity of the different radiative and non-radiative processes involved, it is difficult to separate the various effects. Further work is necessary in order to conclusively settle this issue. Although the air suspended membrane structure used, in theory provides a very strong spontaneous lifetime change, it may be necessary to modify the structure to avoid the thermal heating problems limiting the measurements in chapter 7. However, the large differences in lifetime between bandgap and out-of-gap frequencies have shown that without significant efforts to optimize the structure, significantly modified spontaneous emission is possible in geometries that lack a complete bandgap but are also much simpler in terms of fabrication.

The modification of the spontaneous emission rate due to the changes to the local electromagnetic field resulting from the photonic crystal structure demonstrates that electromagnetic properties of a material can be engineered through nano and microstructure. This is a very fundamental property and extends beyond spontaneous emission to all electromagnetic interactions including such properties as resonant transition related behaviour and optical nonlinearities. This work has only begun to scratch the surface of the rich and diverse possibilities offerred by the possibility of engineered optical properties.

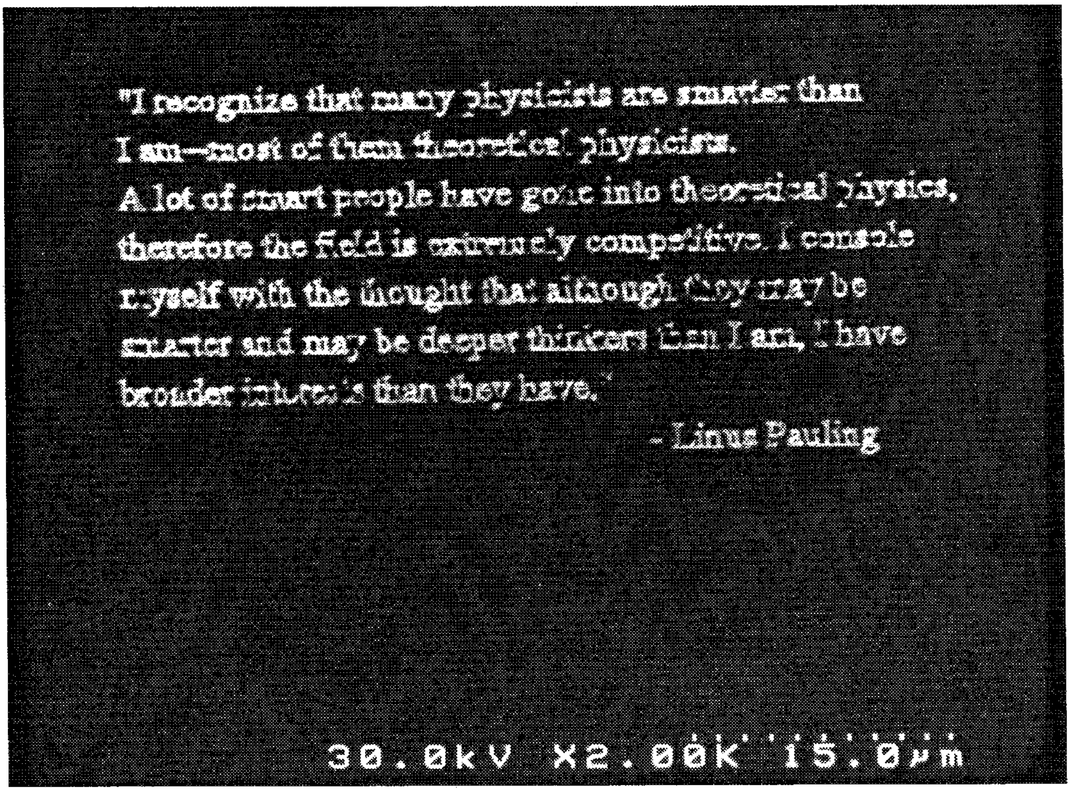

Figure 8.1: Electron beam lithographically defined pattern etched into silicon by XeF_2 chemically assisted ion beam etching (CAIBE)

Bibliography

[1] A. Yariv and P. Yeh, *Optical Waves in Crystals*, John Wiley & Sons Inc., New York, 1984.

[2] H. Kolgenik and C.V. Shank, "Coupled wave theory of distributed feedback lasers," *J. App. Phys.*, vol. 43, pp. 2328, 1972.

[3] M. Nakamura, H.W. Yen, A. Yariv, E. Garmire, S. Somekh, and H.L. Garvin, "Laser oscillations in epitaxial GaAs waveguides with separate optical carrier confinement," *App. Phys. Lett.*, vol. 23, pp. 224, 1973.

[4] G.A. Evans and J.M. Hammer, Eds., *Surface emitting semiconductor lasers and arrays*, Quantum Electronics - Principles and Applications. Academic Press, New York, 1993.

[5] M.A. Duguay, Y. Kokubun, T.L. Koch, and L. Pfeiffer, "Antiresonant reflecting optical wave-guides in SiO_2-Si multilayer structures," *App. Phys. Lett.*, vol. 49, no. 1, pp. 13–15, 1986.

[6] P. Yeh and A. Yariv, "Bragg reflection waveguides," *Opt. Comm.*, vol. 19, no. 3, pp. 427–430, December 1976.

[7] E. Yablonovitch, "Inhibited spontaneous emission in solid-state physics and electronics," *Phys. Rev. Lett.*, vol. 58, no. 20, pp. 2059–2062, 1987.

[8] S. John, "Strong localization of photons in certain disordered dielectric superlattices," *Phys. Rev. Lett.*, vol. 58, no. 23, pp. 2486–2489, 1987.

[9] E. Yablonovitch, "Photonic band-gap structures," *J. Opt. Soc. Am. B*, vol. 10, no. 2, pp. 283–295, 1993.

[10] E. Yablonovitch, T.J. Gmitter, R.D. Meade, A.M. Rappe, K.D. Brommer, and J.D. Joannopoulos, "Donor and acceptor modes in photonic band-structure," *Phys. Rev. Lett.*, vol. 67, no. 24, pp. 3380–3383, 1991.

[11] T. Baba, "Photonic crystals and microdisk cavities based on GaInAsP-InP system," *IEEE J. Select. Top. Quant. Elect.*, vol. 3, no. 3, pp. 808–830, 1997.

[12] T.F. Krauss and R.M. De la Rue, "Photonic crystals in the optical regime - past, present and future," *Prog. in Quant. Elec.*, vol. 23, no. 2, pp. 51–96, 1999.

[13] P.S.J. Russell, S. Tredwell, and P.J. Roberts, "Full photonic bandgaps and spontaneous emission control in 1D multilayer dielectric structures," *Opt. Comm.*, vol. 160, no. 1-3, pp. 66–71, 1999.

[14] E.M. Purcell, "Spontaneous emission probabilities at radio frequencies," *Phys. Rev.*, vol. 69, pp. 681, 1946.

[15] D. Kleppner, "Inhibited spontaneous emission," *Phys. Rev. Lett.*, vol. 47, pp. 233, 1981.

[16] A.F.J. Levi, S.L. McCall, S.J. Pearton, and R.A. Logan, "Room temperature operation of submicrometer radius disc laser," *Elect. Lett.*, vol. 29, no. 18, pp. 1666–1668, 1993.

[17] S.L. McCall, A.F.J. Levi, R.E. Slusher, S.J. Pearton, and R.A. Logan, "Whispering-gallery mode microdisk lasers," *App. Phys. Lett.*, vol. 60, no. 3, pp. 289–291, 1992.

[18] N.C. Frateschi and A.F.J. Levi, "Resonant modes and laser spectrum of microdisk lasers," *App. Phys. Lett.*, vol. 66, no. 22, pp. 2932–2934, 1995.

[19] N.C. Frateschi and A.F.J. Levi, "The spectrum of microdisk lasers," *J. App. Phys.*, vol. 80, no. 2, pp. 644–653, 1996.

[20] Y. Xu, J.S. Vuckovic, R.K. Lee, O.J. Painter, A. Scherer, and A. Yariv, "Finite-difference time-domain calculation of spontaneous emission lifetime in a microcavity," *J. Opt. Soc. Am. B*, vol. 16, no. 3, pp. 465–474, 1999.

[21] Y. Xu, R.K. Lee, and A. Yariv, "Finite-difference time-domain analysis of spontaneous emission in a microdisk cavity - art. no. 033808," *Phys. Rev. A*, vol. 61, no. 3, pp. 3808–+, 2000.

[22] B. Gayral, J.M. Gerard, B. Sermage, B. Legrand, V. Thierry-Mieg, and E. Costard, "Experimental evidence of spontaneous emission enhancement for quantum boxes in pillar microcavities," *Superlattices and microstructures*, vol. 25, no. 1-2, pp. 401–404, 1999.

[23] J.M. Gerard, B. Sermage, B. Gayral, B. Legrand, E. Costard, and V. Thierry-Mieg, "Enhanced spontaneous emission by quantum boxes in a monolithic optical microcavity," *Phys. Rev. Lett.*, vol. 81, no. 5, pp. 1110–1113, 1998.

[24] J.M. Gerard and B. Gayral, "Strong purcell effect for InAs quantum boxes in three-dimensional solid-state microcavities," *IEEE J. Lightwave Tech.*, vol. 17, no. 11, pp. 2089–2095, 1999.

[25] D.G. Deppe, L.A. Graham, and D.L. Huffaker, "Enhanced spontaneous emission using quantum dots and an apertured microcavity," *IEEE J. Quant. Elect.*, vol. 35, no. 10, pp. 1502–1508, 1999.

[26] L.A. Graham, D.L. Huffaker, and D.G. Deppe, "Spontaneous lifetime control in a native-oxide- apertured microcavity," *App. Phys. Lett.*, vol. 74, no. 17, pp. 2408–2410, 1999.

[27] O. Painter, J. Vuckovic, and A. Scherer, "Defect modes of a two-dimensional photonic crystal in an optically thin dielectric slab," *J. Opt. Soc. Am. B*, vol. 16, no. 2, pp. 275–285, 1999.

[28] R. Coccioli, M. Boroditsky, K.W. Kim, Y. Rahmat-Samii, and E. Yablonovitch, "Smallest possible electromagnetic mode volume in a dielectric cavity," *IEE Proc.-Optoelectronics*, vol. 145, no. 6, pp. 391–397, 1998.

[29] P.R. Villeneuve, S. Fan, S.G. Johnson, and J.D. Joannopoulos, "Three-dimensional photon confinement in photonic crystals of low-dimensional periodicity," *IEE Proc.-Optoelectronics*, vol. 145, no. 6, pp. 384–390, 1998.

[30] E. Yablonovitch and T.J. Gmitter, "Photonic band-structure - the face-centered-cubic case," *Phys. Rev. Lett.*, vol. 63, no. 18, pp. 1950–1953, 1989.

[31] J. Martorell and N.M. Lawandy, "Observation of inhibited spontaneous emission in a periodic dielectric structure," *Phys. Rev. Lett.*, vol. 65, no. 15, pp. 1877–1800, 1990.

[32] E.P. Petrov, V.N. Bogomolov, I.I. Kalosha, and S.V. Gaponenko, "Spontaneous emission of organic molecules embedded in a photonic crystal," *Phys. Rev. Lett.*, vol. 81, no. 1, pp. 77–80, 1998.

[33] E.P. Petrov, V.N. Bogomolov, I.I. Kalosha, and S.V. Gaponenko, "Modification of the spontaneous emission of dye molecules in photonic crystals," *Acta Physica Polonica A*, vol. 94, no. 5-6, pp. 761–771, 1998.

[34] S.V. Gaponenko, V.N. Bogomolov, E.P. Petrov, A.M. Kapitonov, D.A. Yarotsky, I.I. Kalosha, A.A. Eychmueller, A.L. Rogach, J. McGilp, U. Woggon, and F. Gindele, "Spontaneous emission of dye molecules, semiconductor nanocrystals, and rare-earth ions in opal-based photonic crystals," *IEEE J. Lightwave Tech.*, vol. 17, no. 11, pp. 2128–2137, 1999.

[35] S.G. Romanov, T. Maka, C.M.S. Torres, M. Muller, and R. Zentel, "Emission properties of dye-polymer-opal photonic crystals," *IEEE J. Lightwave Tech.*, vol. 17, no. 11, pp. 2121–2127, 1999.

[36] S.G. Romanov, R.M. De la Rue, H.M. Yates, and M.E. Pemble, "Impact of gap layer deposition upon photonic bandgap behaviour of opal," *J. Phys.-Cond. Matt*, vol. 12, no. 3, pp. 339–348, 2000.

[37] *Harnessing Light: Optical Sciences and Engineering for the 21st Century.* National Academy Press, 1998.

[38] K. Sakoda, "Transmittance and bragg reflectivity of 2-dimensional photonic lattices," *Phys. Rev. B*, vol. 52, no. 12, pp. 8992–9002, 1995.

[39] K. Sakoda, "Optical transmittance of a two-dimensional triangular photonic lattice," *Phys. Rev. B*, vol. 51, no. 7, pp. 4672, 1995.

[40] M. Plihal and A.A. Maradudin, "Photonic band structure of two-dimensional systems: The triangular lattice," *Phys. Rev. B*, vol. 44, no. 16, pp. 85565–8571, 1991.

[41] J.D. Jackson, *Classical Electrodynamics*, Wiley, New York, 1975.

[42] C. Kittel, *Introduction to Solid State Physics*, John Wiley & Sons Inc., New York, 7th edition, 1996.

[43] N.W. Ashcroft and N.D. Mermin, *Solid State Physics*, Saunders College, Philadelphia, PA, 1976.

[44] J.D. Joannopoulos, R.D. Meade, and J.N. Winn, *Photonic Crystals, Molding the Flow of Light*, Princeton University Press, Princeton, NJ, 1995.

[45] K.M. Ho, C.T. Chan, and C.M. Soukoulis, "Existence of a photonic gap in periodic dielectric structures," *Phys. Rev. Lett.*, vol. 65, no. 25, pp. 3152–3155, 1990.

[46] X.P. Feng and Y. Arakawa, "Off-plane angle dependence of photonic band gap in a two-dimensional photonic crystal," *IEEE J. Quant. Elect.*, vol. 32, no. 3, pp. 535–542, 1996.

[47] T. Søndergaard, J. Broeng, A. Bjarklev, K. Dridi, and S.E. Barkou, "Suppression of spontaneous emission for a two- dimensional honeycomb photonic bandgap structure estimated using a new effective-index model," *IEEE J. Quant. Elect.*, vol. 34, no. 12, pp. 2308–2313, 1998.

[48] H. Benisty, D. Labilloy, C. Weisbuch, C.J.M. Smith, T.F. Krauss, D. Cassagne, A. Beraud, and C. Jouanin, "Radiation losses of waveguide-based two-dimensional photonic crystals: Positive role of the substrate," *App. Phys. Lett.*, vol. 76, no. 5, pp. 532–534, 2000.

[49] K.S. Yee, "Numerical solution of initial boundary value problems involving Maxwell's equations in isotropic media," *IEEE Trans. Antennas and Prop.*, vol. AP-14, pp. 302–307, 1966.

[50] C.M. Furse and O.P. Gandhi, "Why the DFT is faster than the FFT for FDTD time-to-frequency domain conversions," *IEEE Microwave Guid. Wave Lett.*, vol. 5, no. 10, pp. 326–328, 1995.

[51] G. Mur, "Absorbing boundary conditions for the finite-difference approximation of the time-domain electromagnetic-field equations," *IEEE Trans. Electromagn. Compat.*, vol. EMC-23, pp. 377–382, 1981.

[52] J.P. Berenger, "A perfectly matched layer for the absorption of electromagnetic-waves," *J. Comp. Phys.*, vol. 114, no. 2, pp. 185–200, 1994.

[53] S.D. Gedney, "An anisotropic perfectly matched layer-absorbing medium for the truncation of FDTD lattices," *IEEE Trans. Antennas and Prop.*, vol. 44, no. 12, pp. 1630–1639, 1996.

[54] J.P. Berenger, "Three-dimensional perfectly matched layer for the absorption of electromagnetic waves," *J, Comp. Phys.*, vol. 127, no. 2, pp. 363–379, 1996.

[55] E.A. Hinds, *Cavity Quantum Electrodynamics*, chapter : Perturbative cavity quantum electrodynamics, Academic, New York, 1994.

[56] C.H. Henry and R.F. Kazarinov, "Quantum noise in photonics," *Rev. Mod. Phys.*, vol. 68, no. 3, pp. 801–853, 1996.

[57] R.J. Glauber and M. Lewenstein, "Quantum optics of dielectric media," *Phys. Rev. A*, vol. 43, no. 1, pp. 467–491, 1991.

[58] S.M. Barnett, B. Huttner, and R. Loudon, "Spontaneous emission in absorbing dielectric media," *Phys. Rev. Lett.*, vol. 68, no. 25, pp. 3698–3701, 1992.

[59] G.L.J.A Rikken and Y.A.R.R Kessener, "Local-field effects and electric and magnetic dipole transitions in dielectrics," *Phys. Rev. Lett.*, vol. 74, no. 6, pp. 880–883, 1995.

[60] E. Snoeks, A. Lagendijk, and A. Polman, "Measuring and modifying the spontaneous emission rate of erbium near an interface," *Phys. Rev. Lett.*, vol. 74, no. 13, pp. 2459–2462, 1995.

[61] P.W. Milonni, "Field quantization and radiative processes in dispersive dielectric media," *J. Mod. Opt.*, vol. 42, no. 10, pp. 1991–2004, 1995.

[62] Y. Yamamoto and S. Machida, "Microcavity semiconductor laser with enhanced spontaneous emission," *Phys. Rev. A*, vol. 44, pp. 657–668, 1991.

[63] D. Labilloy, H. Benisty, C. Weisbuch, T.F. Krauss, C.J.M. Smith, R. Houdre, and U. Oesterle, "High-finesse disk microcavity based on a circular bragg reflector," *App. Phys. Lett.*, vol. 73, no. 10, pp. 1314–1316, 1998.

[64] C.J.M. Smith, H. Benisty, D. Labilloy, U. Oesterle, R. Houdre, T.F. Krauss, R.M. De la Rue, and C. Weisbuch, "Near-infrared microcavities confined by two- dimensional photonic bandgap crystals," *Elect. Lett.*, vol. 35, no. 3, pp. 228–230, 1999.

[65] R.K. Lee, O.J. Painter, B. D'Urso, A. Scherer, and A. Yariv, "Measurement of spontaneous emission from a two- dimensional photonic band gap defined

microcavity at near-infrared wavelengths," *App. Phys. Lett.*, vol. 74, no. 11, pp. 1522–1524, March 1999.

[66] R.K. Lee, O.J. Painter, B. Kitzke, A. Scherer, and A. Yariv, "Photonic bandgap disk laser," *Elect. Lett.*, vol. 35, no. 7, pp. 569–570, 1999.

[67] O. Painter, R.K. Lee, A. Scherer, A. Yariv, J.D. O'Brien, P.D. Dapkus, and I. Kim, "Two-dimensional photonic band-gap defect mode laser," *Science*, vol. 284, no. 5421, pp. 1819–1821, 1999.

[68] O.J. Painter, A. Husain, A. Scherer, J.D. O'Brien, I. Kim, and P.D. Dapkus, "Room temperature photonic crystal defect lasers at near-infrared wavelengths in ingaasp," *IEEE J. Lightwave Tech.*, vol. 17, no. 11, pp. 2082–2088, 1999.

[69] M. Sargent III, M.O. Scully, and W.E. Lamb Jr., *Laser Physics*, Addison-Wesley, 1974.

[70] B. Sapoval and C. Hermann, *Physics of Semiconductors*, Springer-Verlag, New York, 1995.

[71] L.D. Landau and E.M. Lifshitz, *Quantum Mechanics*, vol. 2 of *A shorter course of theoretical physics*, Pergamon Press, New York, 1974.

[72] D.F. Walls and G.J. Milburn, *Quantum Optics*, Springer-Verlag, New York, 1995.

[73] L. Mandel and E. Wolf, *Optical coherence and quantum optics*, Cambridge University Press, New York, 1995.

[74] S.W. Corzine, R.S. Geels, J.W. Scott, R.H. Yan, and L.A. Coldren, "Design of fabry-perot surface-emitting lasers with a periodic gain structure," *IEEE J. Quant. Elect.*, vol. 25, no. 6, pp. 1513–1524, 1989.

[75] A. Yariv, *Quantum Electronics*, John Wiley & Sons Inc., New York, 1989.

[76] E.F. Schubert, N.E.J. Hunt, M. Micovic, R.J. Malik, D.L. Sivco, A.Y. Cho, and G.J. Zydzik, "Highly efficient light-emitting diodes with microcavities," *Science*, vol. 265, no. 5174, pp. 943–945, 1994.

[77] S.H. Fan, P.R. Villeneuve, J.D. Joannopoulos, and E.F. Schubert, "High extraction efficiency of spontaneous emission from slabs of photonic crystals," *Phys. Rev. Lett.*, vol. 78, no. 17, pp. 3294–3297, 1997.

[78] J. O'Brien, O. Painter, R.K. Lee, C.C. Cheng, A. Yariv, and A. Scherer, "Lasers incorporating 2D photonic bandgap mirrors," *Elect. Lett.*, vol. 32, no. 24, pp. 2243–2244, November 1996.

[79] A. Rosenberg, R.J. Tonucci, and E.A. Bolden, "Photonic band-structure effects in the visible and near ultraviolet observed in solid-state dielectric arrays," *App. Phys. Lett.*, vol. 69, no. 18, pp. 2638–2640, 1996.

[80] P.L. Gourley, J.R. Wendt, G.A. Vawter, T.M. Brennan, and B.E. Hammons, "Optical-properties of 2-dimensional photonic lattices fabricated as honeycomb nanostructures in compound semiconductors," *App. Phys. Lett.*, vol. 64, no. 6, pp. 687–689, 1994.

[81] B. D'Urso, O. Painter, J. O'Brien, T. Tombrello, A. Yariv, and A. Scherer, "Modal reflectivity in finite-depth two-dimensional photonic-crystal microcavities," *J. Opt. Soc. Am. B*, vol. 15, no. 3, pp. 1155–1159, March 1998.

[82] D. Labilloy, H. Benisty, C. Weisbuch, T.F. Kraus, R.M. De La Rue, V. Bardinal, R. Houdré, U. Oesterle, D. Cassagne, and C. Jouanin, "Quantitative measurement of transmission, reflection and diffraction of two-dimensional photonic band gap structures at near-infrared wavelengths," *Phys. Rev. Lett.*, vol. 79, no. 21, pp. 4147–4150, 1997.

[83] M. Berggren, A. Dodabalapur, R.E. Slusher, Z. Bao, A. Timko, and O. Nalamasu, "Organic lasers based on lithographically defined photonic-bandgap resonators," *Elect. Lett.*, vol. 34, no. 1, pp. 90–91, 1998.

[84] M. Boroditsky, T.F. Krauss, R. Coccioli, R. Vrijen, R. Bhat, and E. Yablonovitch, “Light extraction from optically pumped light- emitting diode by thin-slab photonic crystals,” *App. Phys. Lett.*, vol. 75, no. 8, pp. 1036–1038, 1999.

[85] A. Scherer, O. Painter, B. D’Urso, R. Lee, and A. Yariv, “InGaAsP photonic band gap crystal membrane microresonators,” *J. Vac. Sci. Tech. B*, vol. 16, no. 6, pp. 3906–3910, 1998.

[86] M. Boroditsky, I. Gontijo, M. Jackson, R. Vrijen, E. Yablonovitch, T. Krauss, C.C. Cheng, A. Scherer, R. Bhat, and M. Krames, “Surface recombination measurements on III-V candidate materials for nanostructure light-emitting diodes,” *J. App. Phys.*, vol. 87, no. 7, pp. 3497–3504, 2000.

[87] P. St. J. Russell, D. M. Atkin, and T. A. Birks, *Bound Modes Of Two-Dimensional Photonic Crystal Waveguides*, pp. 203–218, Kluwer Academic Publishers, The Netherlands, 1996.

[88] G.R. Fowles, *Introduction to modern optics*, Dover, New York, 1989.

[89] C.C. Cheng, V. Arbet-Engels, E. Yablonovitch, and A. Scherer, “Lithographic band gap tuning in photonic band gap crystals,” *J. Vac. Sci. Tech. B*, vol. 14, no. 6, pp. 4110–4114, 1996.

[90] Landolt-Bornstein, *Numerical Data and Function relationships in Science and technology*, vol. 17a-b, Springer-Verlag, Berlin, 1982.

[91] R.K. Lee, Y. Xu, and A. Yariv, “Modified spontaneous emission from a two-dimensional photonic band gap crystal slab,” *Manuscript B009742 accepted for publication, J. OSA B*, April 2000.

[92] S.L. McCall, P.M. Platzman, R. Dalichaouch, D. Smith, and S. Schultz, “Microwave propagation in 2-dimensional dielectric lattices,” *Phys. Rev. Lett.*, vol. 67, no. 15, pp. 2017–2020, 1991.

[93] S.Y. Lin, V.M. Hietala, S.K. Lyo, and A. Zaslavsky, "Photonic band gap quantum well and quantum box structures: A high-Q resonant cavity," *App. Phys. Lett.*, vol. 68, no. 23, pp. 3233–3235, 1996.

[94] N. Kawai, M. Wada, and K. Sakoda, "Numerical analysis of localized defect modes in a photonic crystal: Two-dimensional triangular lattice with square rods," *Jap. J. App. Phys.*, vol. 37, no. 8, pp. 4644–4647, 1998, part 1.

[95] T. Ueta, K. Ohtaka, N. Kawai, and K. Sakoda, "Limits on quality factors of localized defect modes in photonic crystals due to dielectric loss," *J. App. Phys.*, vol. 84, no. 11, pp. 6299–6304, 1998.

[96] J. Vuckovic, O. Painter, Y. Xu, A. Yariv, and A. Scherer, "Finite-difference time-domain calculation of the spontaneous emission coupling factor in optical microcavities," *IEEE J. Quant. Elect.*, vol. 35, no. 8, pp. 1168–1175, 1999.

[97] R.K. Lee, O. Painter, B. Kitzke, A. Scherer, and A. Yariv, "Emission properties of a defect cavity in a two-dimensional photonic bandgap crystal slab," *J. Opt. Soc. Am. B*, vol. 17, no. 4, pp. 629–633, 2000.

[98] V. Kuzmiak and A.A. Maradudin, "Localized defect modes in a two-dimensional triangular photonic crystal," *Phys. Rev. B*, vol. 57, no. 24, pp. 15242–15250, 1998.

[99] M. Boroditsky, R. Vrijen, T.F. Krauss, R. Coccioli, R. Bhat, and E. Yablonovitch, "Spontaneous emission extraction and Purcell enhancement from thin-film 2-D photonic crystals," *IEEE J. Lightwave Tech.*, vol. 17, no. 11, pp. 2096–2112, 1999.

[100] R. Williams, *Modern GaAs processing methods*, Artech House, Norwood, MA, 1990.

[101] S.J. Wind, P.D. Gerber, and H. Rothuizen, "Accuracy and efficiency in electron beam proximity effect correction," *J. Vac. Sci. Tech. B*, vol. 16, no. 6, pp. 3262–3268, 1998.

[102] U. Hofmann, R. Crandall, and L. Johnson, "Fundamental performance of state-of-the-art proximity effect correction methods," *J. Vac. Sci. Tech. B*, vol. 17, no. 6, pp. 2940–2944, 1999.

[103] R. Crandall, U. Hofmann, and R.L. Lozes, "Contrast limitations in electron-beam lithography," *J. Vac. Sci. Tech. B*, vol. 17, no. 6, pp. 2945–2947, 1999.

[104] A. Olkhovets and H.G. Craighead, "Low voltage electron beam lithography in PMMA," *J. Vac. Sci. Tech. B*, vol. 17, no. 4, pp. 1366–1370, 1999.

[105] I. Schnitzer, E. Yablonovitch, C. Caneau, T.J. Gmitter, and A. Scherer, "30-percent external quantum efficiency from surface textured, thin-film light-emitting-diodes," *App. Phys. Lett.*, vol. 63, no. 16, pp. 2174–2176, 1993.

[106] E.F. Schubert, Y.H. Wang, A.Y. Cho, L.W. Tu, and G.J. Zidzik, "Resonant cavity light-emitting diode," *App. Phys. Lett.*, vol. 60, no. 8, pp. 921–923, 1992.

[107] S. John and K. Busch, "Photonic bandgap formation and tunability in certain self-organizing systems," *IEEE J. Lightwave Tech.*, vol. 17, no. 11, pp. 1931–1943, 1999.

[108] Y. Xu, R.K. Lee, and A. Yariv, "Quantum analysis and the classical analysis of spontaneous emission in a microcavity - art. no. 033807," *Phys. Rev. A*, vol. 61, no. 3, pp. 3807–+, 2000.

[109] J.K. Hwang, H.Y. Ryu, and Y.H. Lee, "Spontaneous emission rate of an electric dipole in a general microcavity," *Phys. Rev. B*, vol. 60, no. 7, pp. 4688–4695, 1999.

[110] T. Baba, K. Inoshita, H. Tanaka, J. Yonekura, M. Ariga, A. Matsutani, T. Miyamoto, F. Koyama, and K. Iga, "Strong enhancement of light extraction efficiency in GaInAsP 2-D-arranged microcolumns," *IEEE J. Lightwave Tech.*, vol. 17, no. 11, pp. 2113–2120, 1999.

[111] S.M. Barnett and R. Loudon, "Sum rule for modified spontaneous emission rates," *Phys. Rev. Lett.*, vol. 77, no. 12, pp. 2444–2446, 1996.

[112] S.M. Barnett and R. Loudon, "Sum rule for environmentally modified spontaneous emission rates," *Quant. and Semiclass. Opt.*, vol. 10, no. 4, pp. 591–599, 1998.

[113] C.M. Anderson and K.P. Giapis, "Larger two-dimensional photonic band gaps," *Phys. Rev. Lett.*, vol. 77, no. 14, pp. 2949–2952, 1996.

[114] C.M. Anderson and K.P. Giapis, "Symmetry reduction in group 4mm photonic crystals," *Phys. Rev. B*, vol. 56, no. 12, pp. 7313–7320, 1997.

[115] C.H. Henry and K. Nassau, "Lifetimes of bound excitons in CdS," *J. Lumin.*, vol. 1,2, pp. 299–306, 1970.

[116] Stanford Research Systems, Sunnyvale, CA, *Model SR844 RF Lock-In Amplifier*, 2.3 edition, April 1997.

[117] G.P. Agrawal and N.K. Dutta, *Long-wavelength semiconductor lasers*, Van Nostrand Reinhold, New York, 1986.

[118] L.A. Coldren and S.W. Corzine, *Diode lasers and photonic integrated circuits*, John Wiley & Sons Inc., New York, 1995.

[119] *Handbook of Mathematical Functions with Formulas, Graphs and Mathematical Tables.* US Department of Commerce, 1964.

[120] E. Wintner and E.P. Ippen, "Nonlinear carrier dynamics in $\mathrm{Ga}_x\mathrm{In}_{1-x}\mathrm{As}_y\mathrm{P}_{1-y}$ compounds," *App. Phys. Lett.*, vol. 44, no. 10, pp. 999–1001, 1984.

[121] B.E. Maile, A. Forchel, R. Germann, and D. Grutzmacher, "Impact of sidewall recombination on the quantum efficiency of dry etched InGaAs/InP semiconductor wires," *App. Phys. Lett.*, vol. 54, no. 16, pp. 1552–1554, 1989.

[122] D.D. Nolte, "Surface recombination, free-carrier saturation, and dangling bonds in InP and GaAs," *Solid-State Elec.*, vol. 33, no. 2, pp. 295–298, 1990.

[123] B. Hubner, R. Zengerle, and A. Forchel, "Direct optical analysis of the carrier diffusion in semiconductor wire structures," *Mat. Sci. and Eng. B*, vol. 35, no. 1-3, pp. 273–277, 1995.

[124] B. Jacobs, M. Emmerling, A. Forchel, I. Gyuro, P. Speier, and E. Zielinski, "Optical investigations of the sidewall recombination in wet etched InGaAs/InP-wires," *Jap. J. App. Phys.*, vol. 32, no. 2A, pp. L173–L176, 1993.

[125] B. Jacobs, H. Zull, A. Forchel, I. Gyuro, P. Speier, and E. Zielinski, "Comparison of the sidewall recombination in dry and wet etched InGaAs/InP wires," *Microelec. Eng.*, vol. 21, no. 1-4, pp. 401–404, 1993.

[126] S. Evoy, G.F. Redinbo, and H.G. Craighead, "Cathodoluminescence and photoluminescence analysis of $\mathrm{In}_x\mathrm{Ga}_{1-x}\mathrm{As}$/GaAs quantum well structures," *App. Phys. Lett.*, vol. 68, no. 9, pp. 1259–1261, 1996.

[127] H. Fujikura, M. Kubo, and H. Hasegawa, "Excitation power dependent photoluminescence behavior in etched quantum. wires having silicon interlayer-based edge passivation and its interpretation," *Jap. J. App. Phys.*, vol. 36, no. 3B, pp. 1937–1943, 1997.

[128] S.Y. Lin, E. Chow, V. Hietala, P.R. Villeneuve, and J.D. Joannopoulos, "Experimental demonstration of guiding and bending of electromagnetic waves in a photonic crystal," *Science*, vol. 282, no. 5387, pp. 274–276, 1998.

[129] T. Baba, N. Fukaya, and J. Yonekura, "Observation of light propagation in photonic crystal optical waveguides with bends," *Elect. Lett.*, vol. 35, no. 8, pp. 654–655, 1999.

[130] S. Nojima, "Enhancement of optical gain in two-dimensional photonic crystals with active lattice points," *Jap. J. App. Phys.*, vol. 37, no. 5B, pp. L565–L567, 1998.

[131] M. Meier, A. Mekis, A. Dodabalapur, A. Timko, R.E. Slusher, J.D. Joannopoulos, and O. Nalamasu, "Laser action from two-dimensional distributed feedback in photonic crystals," *App. Phys. Lett.*, vol. 74, no. 1, pp. 7–9, 1999.

[132] H. Kosaka, T. Kawashima, A. Tomita, M. Notomi, T. Tamamura, T. Sato, and S. Kawakami, "Superprism phenomena in photonic crystals," *Phys. Rev. B*, vol. 58, no. 16, pp. R10096–R10099, 1998.